

Energy Research and Development Division  
**FINAL PROJECT REPORT**

# **Solar-Reflective “Cool” Walls: Benefits, Technologies, and Implementation**

Appendix N: Development of Fluorescent Cool  
Pigments (Task 5.2 Report)

**California Energy Commission**  
**Gavin Newsom, Governor**

April 2019 | CEC-500-2019-040-APN





# Appendix N: Development of fluorescent cool pigments (Task 5.2 report)

---

Paul Berdahl<sup>1</sup>, Sharon Chen<sup>1</sup>, and Ronnen Levinson<sup>1</sup>

<sup>1</sup> Heat Island Group, Lawrence Berkeley National Laboratory

31 May 2018

## Abstract

The re-emission at longer wavelengths of light absorbed at shorter wavelengths, or fluorescence, can lower the temperature in the sun of dark surfaces. We identified and developed two classes of pigments that fluoresce in or close to the invisible near-infrared spectrum: one based on ruby (aluminum oxide doped with chromium), which we have used to formulate pink and red coatings; and another based on the Egyptian and Han blue family (calcium copper tetra-silicate, and variants replacing calcium with barium or strontium), which we have used to prepare blue, green, and blue-black coatings. Measurements made with a calorimetric apparatus developed in this study indicate that fluorescence can reject up to 15% of the sunlight incident on these coatings. Some of the fluorescent blue pigments also exhibit a quantum yield (number of emitted photons divided by the number of exciting photons that are absorbed) much higher than that previously reported. This may facilitate their use in luminescent solar concentrators for photovoltaic generation of electricity.

## 1 Overview

Various pigments are used to formulate desired non-white colors that stay cooler in the sun than alternatives. These cool pigments provide a high near-infrared (NIR) reflectance in the solar infrared range of 700 to 2500 nm, and also a color specified by a reflectance spectrum in the 400 to 700 nm visible range. Still cooler materials can be formulated by also utilizing the phenomenon of fluorescence (photoluminescence).

While potential fluorescent cool pigments have been screened during a prior DOE funded project with PPG Industries (Zalich and Kornish 2016), only a few pigments have demonstrated the potential for efficient fluorescence and also appear to have adequate (low) cost and durability. The first such pigment was ruby, which is composed of aluminum oxide doped with chromium. It can be used to produce red and pink colored materials. The second important

class of materials includes the ancient pigment Egyptian blue. Egyptian blue has the chemical composition of  $\text{CaCuSi}_4\text{O}_{10}$ —that is, calcium copper tetra-silicate. The most important other members of this class, the Egyptian blue family, have the same formula but with barium (Ba) or strontium (Sr) replacing calcium. The barium variant is also known from ancient times as Han (or Chinese) blue. The strontium variant has no common name. The best performance to date with the Egyptian blue family has been achieved with the calcium and strontium compounds. These blue pigments can also be blended with yellow pigment to achieve a green color, or with an orange pigment to obtain a blue-shade black. The blending process does not diminish the near-infrared fluorescence.

Laboratory-fabricated coatings have shown that coatings with fluorescent pigments can provide a contribution, or boost, to the Effective Solar Reflectance (ESR) of up to 0.17 above the ordinary Solar Reflectance (SR). The target for future commercial coatings is a fluorescence benefit (ESR minus SR) of 0.10 to 0.15. The energy flux of full sunlight is roughly  $1,000 \text{ W m}^{-2}$ , so we can expect that future colored fluorescence materials can reduce peak heat absorption rates by 100 to  $150 \text{ W m}^{-2}$ .

## 2 Measurement of effective solar reflectance

If a surface re-emits at longer wavelengths light absorbed at shorter wavelengths, or fluoresces, it will exhibit an effective solar reflectance that is the fraction of incident solar power rejected by the combination of reflection and fluorescence. Like solar reflectance, effective solar reflectance ranges from 0 to 1 (or 0 to 100 percent).

Levinson et al. (2017) detail the development and application of a calorimetric technique for the measurement of effective solar reflectance (Task Report Appendix A).

## 3 Ruby pigments

Even though natural rubies are quite expensive, manufactured rubies are not. The wholesale cost of cut and polished ruby gems for jewelry is about US\$0.30 per carat (200 mg). A layer of manufactured rubies has a pleasing dark red color with a fluorescence benefit of 0.30! Also, ruby pigment is not difficult to manufacture; manufacturers can use the same solid-state reaction techniques they currently employ for other mixed metal oxide pigments such as Fe-Cr-O cool black. Unfortunately, prototype coatings colored with ruby pigment are not as dark as desired and have a fluorescence benefit of only 0.15. Future research may yield further improvements. In the meantime, ruby pigments can provide a dark pink color with high ESR, near 0.80. For comparison, smooth white commercial materials have SR in the range of 0.70 to 0.85—about the same as the ruby pigment. Berdahl et al. (2016) provides more details and shows photos of these materials (Task Report Appendix B).

## 4 Egyptian and Han blue family of pigments

These alkaline earth copper silicates usually are synthesized by solid-state reaction techniques. Briefly, oxides or carbonates of the component metals are intimately mixed and heated in air for a few hours to a temperature near 900 °C. After the synthesis, copper oxide (CuO), a black compound, is usually present as an impurity. If too much CuO is present, the resulting pigment is gray rather than blue. Egyptian blue is available commercially, from Kremer Pigmente. Thus, this company can control the CuO concentration to some extent. However, we have found that for fluorescent pigment applications, even more stringent limitations on CuO contamination are needed. We found that washing (leaching) the commercial pigment with hydrochloric acid (HCl) reduces but does not eliminate the CuO. In Berdahl et al. (2018), included here as a pre-print (Task Report Appendix B), we showed that the near-infrared fluorescence is enhanced by up to a factor of 2 with the HCl soak. The paper also contains color images of some of the samples.

The fluorescence benefits of the prototype materials range from about 0.08 up to 0.17. The best material is based on washed Egyptian blue, with pigment amount of 68 g m<sup>-2</sup>. The visual reflectance (at 550 nm) is only 0.15, a medium dark blue, while the ESR is 0.57. The relatively small amount of pigment needed per unit area indicates that it is a reasonably strong pigment. The density is 3.09 g cm<sup>-2</sup>. Allowing a PVC (pigment volume concentration) of up to 50%, minimum coating thickness is only about 44 μm.

The quantum yield of the fluorescence is the number of emitted photons divided by the number of exciting photons that are absorbed. With only exotic exceptions, the quantum yield must be less than 1.0, and for many fluorescence processes is much less than unity. Our most important result is that the quantum yield of the Ca and Ba variants is quite high and even approaches unity, as shown in Figure 1.

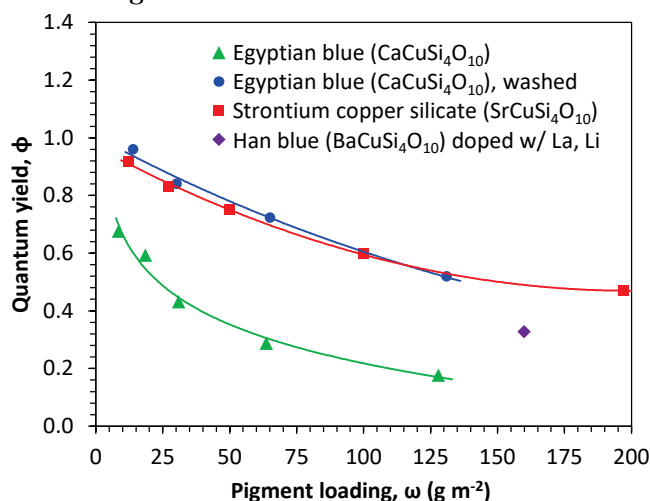


Figure 1. The quantum yield of blue alkaline earth copper silicate pigmented coatings as a function of pigment loading (areal density).

## 5 An unexpected result: Luminescent solar concentrator (LSC) applications

LSC technology is a strategy for concentrating solar radiation for photovoltaic generation of electricity. A large transparent plate containing a phosphor (or an organic dye) absorbs sunlight, resulting in emission of fluorescence, much of which is trapped within the plates by total internal reflection. The trapped energy emerges from the edges of the plate in concentrated form and is then converted to electricity by a photovoltaic cell. The 900 nm fluorescence from Egyptian blue family phosphors is well matched to conventional silicon photovoltaic cells.

It was only recently, in this project, that accurate quantum yield numbers became available. Prior literature indicates that the yield for Egyptian blue is only about 10% and is even lower for the other compounds. Now we know that if the CuO contamination issue is addressed, the quantum yield is high and can even approach unity. For additional detail, see Berdahl et al. (2018) (Task Report Appendix C).

### References

Berdahl P, Boocock SK, Chan GC-Y, Chen SS, Levinson RM, Zalich MA. 2018. High quantum yield of the Egyptian blue family of infrared phosphors ( $\text{MCuSi}_4\text{O}_{10}$ , M = Ca, Sr, Ba). *J. Applied Physics* 123, 193103 (11 pp). <https://doi.org/10.1063/1.5019808>

Berdahl P, Chen SS, Destailats H, Kirchstetter TW, Levinson RM, Zalich MA. 2016. Fluorescent cooling of objects exposed to sunlight - The ruby example. *Solar Energy Materials & Solar Cells* 157, 312-317. <http://doi.org/10.1016/j.solmat.2016.05.058>

Levinson R, Chen S, Ferrari C, Berdahl P, Slack J. 2017. Methods and instrumentation to measure the effective solar reflectance of fluorescent cool surfaces. *Energy & Buildings* 152, 752-765. <http://dx.doi.org/10.1016/j.enbuild.2016.11.007>

Zalich M, Kornish B. 2016. Fluorescent pigments for high-performance cool roofing and facades, DOE project report, Contract No. DE-EE0006347. <http://osti.gov>

**Task Report Appendix A:  
Preprint of ESR measurement article (Levinson et al.  
2017)**

# **Methods and instrumentation to measure the effective solar reflectance of fluorescent cool surfaces**

Ronnen Levinson<sup>1\*</sup>, Sharon Chen<sup>1</sup>, Chiara Ferrari<sup>3</sup>, Paul Berdahl<sup>1</sup>, and Jonathan Slack<sup>1</sup>

<sup>1</sup> Heat Island Group, Lawrence Berkeley National Laboratory

<sup>2</sup> University of Modena and Reggio Emilia, Modena, Italy

\* Corresponding author, RML27@cornell.edu

## **Abstract**

Fluorescent cool dark surfaces stay cool in the sun by reflecting near-infrared (NIR) irradiance and by actively emitting in the NIR spectrum some of the energy absorbed from visible sunlight. The fraction of incident solar energy rejected by reflection and fluorescence is the “effective solar reflectance”, or ESR, of the surface.

It is challenging to measure ESR with a solar spectrometer or a solar reflectometer, the radiometric instruments most commonly used to measure the solar reflectance (SR) of specimens in the laboratory. We have tested a variety of calorimetric techniques for using temperature in the sun to interpolate the effective solar absorptance ( $1 - \text{ESR}$ ) of a fluorescent test specimen from the known solar absorptances of non-fluorescent reference specimens. Our experiments show that averaging out noise in the temperature signal induced by variations in convection is key.

We developed a computer-controlled rotary apparatus that compares the temperatures in the sun of up to six specimens. Trials on six different fluorescent specimens indicate that it can measure ESR with a repeatability of about 0.02. To maximize the ratio of signal to noise in temperature determination, and to facilitate calculation of the fluorescence benefit ( $\text{ESR} - \text{SR}$ ), measurements should be performed with specimens facing the sun.

# 1 Introduction

High solar reflectance can help keep a roof or wall cool in the sun. The coolest building envelope surfaces are bright white, reflecting about 90% of incident sunlight (spectrum 300 – 2,500 nm) when new and unsoiled (CRRC, 2016). In recent decades, cool surface designers have broadened their product color palettes by offering “cool colored” surfaces that pair low reflectance in the visible spectrum (400 – 700 nm) with high reflectance in the near-infrared (NIR) spectrum (700 – 2,500 nm). A high-performance dark cool colored surface available today, such as a natural red clay tile, may reflect about 20% of visible light, and about 60% of NIR light, to attain a solar reflectance (SR) near 0.40 [1].

The temperature in the sun of a non-white surface can be further reduced without affecting color if the surface rapidly re-emits some of the absorbed ultraviolet (UV; 300 – 400 nm) or visible sunlight as invisible NIR radiation. These “fluorescent” cool surfaces can reject sunlight by both reflection (light leaves at the wavelength of incidence) and fluorescence (light leaves at a longer wavelength). Recent collaboration among Lawrence Berkeley National Laboratory (LBNL; Berkeley, CA, USA), PPG Industries, Inc. (Allison Park, PA, USA), and the Shepherd Color Company (West Chester, OH, USA) has yielded fluorescent cool pigments, such as ruby ( $\text{Al}_2\text{O}_3\text{:Cr}$ ), that could be used to make cool dark architectural coatings [2] [3].

The fraction of incident sunlight rejected by the combination of reflection and fluorescence is called “effective solar reflectance,” or ESR. If a surface is opaque, its effective solar absorptance (ESA)  $\alpha_e$  is one minus its effective solar reflectance  $\rho_e$ . Of course, if a surface does not fluoresce, its effective solar reflectance equals its pure solar reflectance (SR)  $\rho$ , and its effective solar absorptance equals its pure solar absorptance (SA)  $\alpha$ .

This study examines various laboratory and field methods for measurement of ESR. We are particularly interested in techniques suited to characterize small coated specimens, on the order of 100 cm<sup>2</sup>, that can be made from limited quantities of prototype cool fluorescent pigments.

We can classify ESR measurement techniques as radiometric (based on measuring radiation) or calorimetric (based on measuring temperature). We note that the idea of relating the solar reflectance of an opaque surface to its temperature in the sun is not new. For example, Berdahl and Bretz [4] showed a close correlation between temperature in the sun and laboratory spectrometer measurement of solar reflectance. Also, Yuan, Emura, & Farnham [5] used surface temperature measurements to estimate the solar reflectance of 50 cm by 50 cm samples of retroreflective building envelope materials.

## 2 Theory

### 2.1 Calorimetric calculation of ESA and ESR

Using a standard linearization of long-wave radiative exchange, the steady-state temperature  $T$  of an adiabatic surface in the sun is governed by the energy balance

$$\alpha_e I = h_c (T - T_a) + h_r (T - T_r) , \quad (1)$$

where  $I$  is global solar irradiance (incident solar power per area);  $T_a$  is air temperature;  $T_r$  is long-wave radiative exchange temperature (equal to sky temperature, if the surface sees only the sky); and  $h_c$  is the convective heat transfer coefficient. The radiative heat transfer coefficient  $h_r$  is approximated as

$$h_r \approx 4 \varepsilon \sigma T_a^3 \quad (2)$$

where  $\varepsilon$  is surface thermal emittance and  $\sigma$  is the Stefan-Boltzmann constant. Solving Eq. (1) for surface temperature yields

$$T = (\alpha_e I + h_c T_a + h_r T_r) / (h_c + h_r). \quad (3)$$

This indicates that neglecting the weak temperature dependences of  $h_c$  and  $h_r$ , surface temperature will scale linearly with ESA (or with pure SA, if the surface does not fluoresce).

Note that while the relationship between surface temperature and ESA varies with  $h_c$  and  $h_r$ , ESA itself is a short-wave radiative property independent of convection and long-wave radiation.

Consider three specimens on a common platform. If a test specimen of unknown ESA  $\alpha_{e,3}$  experiences the same solar irradiance, convective heat transfer coefficient, radiative heat transfer coefficient, air temperature, and radiative exchange temperature as nearby non-fluorescent reference specimens of known pure SAs  $\alpha_1$  and  $\alpha_2$ , the ESA of the test specimen can be related to the pure SAs of the reference specimens by temperature interpolation:

$$\alpha_{e,3} = \alpha_1 + (\alpha_2 - \alpha_1) (T_3 - T_1) / (T_2 - T_1) . \quad (4)$$

The ESA of a test specimen can also be determined by fitting a line of the form

$$T = m \alpha + b \quad (5)$$

to the temperatures and pure SAs of the non-fluorescent reference specimens, then computing

$$\alpha_{e,3} = (T_3 - b) / m . \quad (6)$$

If the test specimen is opaque, its ESR will be

$$\rho_{e,3} = 1 - \alpha_{e,3} . \quad (7)$$

## 2.2 Variations with specimen position of convective heat transfer coefficient

Error in calorimetric determination of ESA via Eq. (4) may be induced by specimen-to-specimen variations in solar irradiance, thermal emittance, or convective heat transfer coefficient. Differences in solar irradiance can be minimized by keeping specimens parallel and avoiding shadows, while thermal emittance can be made consistent through choice of material. However, the forced component of the convective heat transfer coefficient can depend strongly on the distance from leading edge of the platform to leading edge of specimen. Let local Reynold's number

$$\text{Re}_x = U x / \nu \quad (8)$$

where  $U$  is free-stream wind speed,  $x$  is distance from edge of plate (platform), and  $\nu$  is the kinematic viscosity of air. The local forced convective heat transfer coefficient

$$h_x = k \text{Nu}_x / x \quad (9)$$

where  $k$  is the thermal conductivity of air and  $\text{Nu}_x$  is the local Nusselt number. If the flow over the plate is laminar ( $\text{Re}_x < 500,000$ ),

$$\text{Nu}_x = 0.332 \text{Re}_x^{(1/2)} \text{Pr}^{(1/3)} / [1 - (\xi / x)^{(3/4)}]^{(1/3)} \quad (10)$$

where  $\text{Pr}$  is the Prandtl number of air and  $\xi$  is the unheated starting length (Ref. [6], Eq. 6.98). If the flow over the plate is turbulent ( $\text{Re}_x > 500,000$ ), then

$$\text{Nu}_x = (\text{Nu}_x)_{\xi=0} / [1 - (\xi / x)^{(9/10)}]^{(1/9)} \quad (11)$$

where

$$(\text{Nu}_x)_{\xi=0} = 0.0296 \text{Re}_x^{(4/5)} \text{Pr}^{(1/3)} \quad (12)$$

(Ref. [6], Eqs. 6.99 and 6.92).

Figure 1 shows variations with distance from leading edge of plate of laminar and turbulent local forced convective heat transfer coefficients, calculated for a free-stream wind speed of 2 m/s and zero unheated starting length. At that speed, flow is laminar ( $\text{Re}_x < 500,000$ ) for the first 400 cm. The laminar convective heat transfer coefficient drops rapidly from 28 W/m<sup>2</sup>·K at 1 cm, to 9 W/m<sup>2</sup>·K at 10 cm, and to 6 W/m<sup>2</sup>·K at 20 cm. This indicates that unless the specimens are centered on a large platform (say, 1 m by 1 m), variations in distance from platform edge may induce substantial specimen-to-specimen differences in temperature, and thus introduce error in calculation of ESA from measured temperatures.

## 2.3 Uncertainty in ESA

We can use Eq. (1) to approximate the ratio  $s$  of the uncertainty in computed ESA,  $\Delta\alpha_e$ , to uncertainty in measured surface temperature,  $\Delta T$ , as

$$s \equiv \Delta\alpha_e / \Delta T \approx d\alpha_e / dT = (h_c + h_r) / I. \quad (13)$$

The reciprocal of this sensitivity,  $(1/s)$ , can be estimated by measuring the variation with solar absorptance of the surface temperatures of non-fluorescent materials, then calculating the slope of the best linear fit to  $T$  vs.  $\alpha$ .

## 3 Test and reference specimens

This study uses six ruby-based fluorescent test specimens prepared by some of the authors in earlier work [3], and 11 non-fluorescent reference specimens.

The thermal emittance of each test and reference specimen was measured with a Devices & Services Portable Emissometer following ASTM C1371-15: Standard Test Method for Determination of Emittance of Materials Near Room Temperature Using Portable Emissometers [7].

The solar spectral reflectance of each reference specimen was measured with a PerkinElmer Lambda 900 UV-VIS-NIR spectrometer with 150 mm Labsphere integrating sphere, following ASTM E903-12: Standard Test Method for Solar Absorptance, Reflectance, and Transmittance of Materials Using Integrating Spheres [8]. Each specimen was mounted at the sphere's reflectance port in the conventional manner to measure "without window" solar spectral reflectance. In some cases, it was also measured with a quartz window between the port and the specimen to determine "with window" solar spectral reflectance. Each solar spectral reflectance was weighted with an air mass 1 global horizontal (AM1GH) solar spectral irradiance to calculate AM1GH solar reflectance [9] [10].

The pure solar reflectance of each test specimen was measured in accordance with Section 4.2, below.

### 3.1 Fluorescent test specimens

The first test specimen, "ruby crystal clear", is a clear-coated ruby crystal array on a white substrate (Figure 2b). Each crystal is a square pyramid, approximately 5 mm by 5 mm by 2.6 mm. The clear acrylic increases the thermal emittance of this specimen to 0.875 from 0.765 for uncoated crystals.

The remaining five fluorescent test specimens are ruby-pigment coatings (Figure 3). Each coating was prepared by mixing ruby pigment (alumina doped with chromium oxide) into clear acrylic, then applying the pigmented acrylic to a bright white substrate (an aluminum panel painted white). The ruby-pigment coatings are labelled 0.2%, 1%, 2%, 3%, and 4% according to the weight fraction of chromium oxide ( $\text{Cr}_2\text{O}_3$ ) present in the alumina ( $\text{Al}_2\text{O}_3$ ) pigment. Their thermal emittances range from 0.876 to 0.885 (Table 1).

## 3.2 Non-fluorescent reference specimens

We prepared 11 non-fluorescent reference specimens, each 75 mm by 75 mm (Table 2). Reference specimens A1 - A9 are aluminum panels hand painted with two layers of titanium oxide white, then overcoated with titanium oxide white and/or bone black to create a white, gray, or black surface (Figure 4). Their thermal emittances range from 0.886 to 0.926.

Reference specimen A10, “ruby crystal white”, is an aluminum panel with a ruby crystal array, overpainted white (Figure 2c); reference specimen A11, “ruby crystal gray”, is the analog of specimen A10, but overpainted gray, rather than white (Figure 2a). Their thermal emittances are 0.911 and 0.912, respectively. Ruby crystal white and ruby crystal gray each have essentially the same shape and thermal properties as ruby crystal clear.

# 4 Radiometric measurement of ESR

## 4.1 Spectrofluorometer

Absolute and complete spectral fluorescence measurements are not routine, so complete calibrated measurements are uncommon. However, measurement of spectral emission intensity (arbitrary units) is essential for optimizing fluorescent materials. One can compare emission from various samples under the same conditions to find the spectral distributions and even small differences in intensity.

LBNL adapted equipment formerly used to determine the albedo of polluted snow [11] to make a spectrofluorometer that measures fluorescence over the spectrum 500 - 1,100 nm. The apparatus includes a tungsten lamp (with xenon gas fill), a high-quality short-pass filter (optical density 4) to block wavelengths that would interfere with observation of the fluorescence emission, a 150 mm Labsphere integrating sphere, and a spectrophotometer. The incident light passes through the integrating sphere to strike the fluorescent sample, and the diffuse emission is collected by the integrating sphere. An optical fiber port on the sphere passes the fluorescence to the input fiber of a compact Ocean Optics S2000 spectrometer with a fixed diffraction grating and a silicon array detector. The fluorescence spectra of several ruby coatings are shown range at full scale in Figure 5 and with greater detail in ESM Figure A-1.

PPG purchased a PTI (Photon Technology International) QM-500 spectrofluorometer that uses an InGaAs detector (500 - 1,700 nm). The instrument determines the excitation wavelength with an input monochromator and the emission wavelength with an output monochromator, and can thus determine both excitation and emission spectra. This arrangement is more sensitive at longer wavelengths, while the LBNL fluorescence instrumentation, using a silicon array detector, is insensitive to radiation beyond about 1,100 nm.

Since measurements from each spectrofluorometer are reported in arbitrary units, neither instrument can be used as configured to assess effective spectral reflectance (ratio of emitted +

reflected power to excitation power, as a function of excitation wavelength). However, it may be possible to adapt the PTI QM-500 spectrofluorometer to measure effective spectral reflectance by calibrating its input (excitation) and output powers, and adding an integrating sphere. The same adapted spectrofluorometer could also be used to measure pure spectral reflectance by measuring output power only at the excitation wavelength.

## 4.2 Spectrophotometer

Using a UV-VIS-NIR spectrophotometer with integrating sphere to measure effective spectral reflectance is not feasible, because the instrument's calibration protocol assumes that the wavelength of detected light is the same as that of incident light. The effective reflectance spectrum will be inaccurate if instrument response at emission wavelengths differs from that at excitation wavelengths. However, this apparatus can be used to measure the pure spectral reflectance of a fluorescent surface by selectively filtering its detector(s). Pure spectral reflectance can be used to calculate pure solar reflectance, which in turn can be subtracted from ESR to assess the portion of ESR attributable to fluorescence.

For example, ruby emits in the spectrum 650 – 800 nm, with strong peaks near 694 nm (edge of visible spectrum). Covering the photomultiplier used to detect 250 – 900 nm radiation with a filter that blocks this emission (ESM Figure A-2) permits measurement of pure spectral reflectance from 250 to 650 nm. Pure spectral reflectance over the remainder of the solar spectrum (650 – 2,500 nm) can be measured without a filter, since incident radiation at these wavelengths does not excite ruby. Figure 6 shows the apparent solar spectral effective reflectance (blue curve) and the solar spectral pure reflectance (red curve) of ruby crystal clear. Using an air mass 1 global horizontal (AM1GH) solar spectral irradiance to compute broadband properties [9] [10], the apparent difference between apparent effective solar reflectance (0.452) and pure solar reflectance (0.434) is only 0.017. We will later demonstrate that the true ESR of this specimen is about 0.74, indicating that the apparent ESR assessed by spectrophotometer was about 0.28 low.

## 4.3 Reflectometer

Using the Solar Spectrum Reflectometer (Devices & Services, Dallas, TX, USA) to measure ESR presents a similar challenge, because its calibration protocol also assumes that the wavelength of detected light is the same as that of incident light. For example, using version 6 of this instrument to measure the AM1GH ("G1") solar reflectance of ruby crystal clear yields 0.508, or about 0.22 below true ESR. We also note that the incandescent lamp in this reflectometer may not generate enough UV light to excite certain fluorescent pigments.

## 4.4 Pyranometer

The ESR of a very large specimen (at least 4 m by 4 m) could be measured with a first-class pyranometer following ASTM E1918-06(2015): Standard Test Method for Measuring Solar

Reflectance of Horizontal and Low-Sloped Surfaces in the Field [12]. Specifically, E1918 could yield ESR as the ratio of the reflected and fluoresced upflux measured by a downward-facing pyranometer to the solar irradiance measured by an upward-facing pyranometer.

The ESR of a large specimen (about 1 m by 1 m) could be measured with a first-class pyranometer following non-ASTM method E1918A [13] [10]. The E1918A technique exactly covers a test surface with a stacked pair of opaque, non-fluorescent masks of known solar reflectance. The lower mask is black and the upper mask is white. A downward-facing pyranometer first measures upflux with the white mask exposed. The white mask is removed, and upflux is remeasured with the black mask exposed. The black mask is removed, and the upflux is measured a third time with the test surface exposed. The ESR of the test surface can be interpolated from the SRs of the white and black masks by comparing the upflux with test surface exposed to the upfluxes with white and black masks exposed.

Since neither E1918 nor E1918A can determine the ESR of a small test specimen (about 10 cm by 10 cm), these techniques will be more useful when fluorescent cool envelope materials are available in large quantities.

## 4.5 Pyrheliometer plus pyranometer

The ESR of a small test specimen could be measured by using a pyrheliometer to measure reflected plus fluoresced upflux, and a pyranometer to measure downflux (solar irradiance). ESR could then be calculated as the ratio of the measured upflux to the product of the measured irradiance and the view factor from the pyrheliometer to the portion of the test surface that it sees.

The challenge is that since a pyrheliometer has a narrow field of view, it would measure a very small upflux from a test surface whose reflection and fluorescence are diffuse. For example, a vertical pyrheliometer with a 38 mm diameter collimating tube and a 1° “slope” angle that is placed 100 mm above a test surface would see a target of diameter 41 mm. The view factor from the detector tube opening to the target would be 0.039. If the test surface receives an irradiance of 1000 W/m<sup>2</sup> and has an ESR of 0.50, the pyrheliometer would measure an upflux of 19.5 W/m<sup>2</sup>. Raising ESR by 0.05 would increase the measured upflux by only 2 W/m<sup>2</sup>, suggesting that the signal to noise ratio of ESR measurement could be small.

As an aside, it would be reasonable to consider the use of a pyranometer or pyrheliometer plus pyranometer to determine ESR as calorimetric, since each instrument measures radiance with a thermopile. We choose to classify them as radiometric because these methods calculate ESR from radiances, rather than temperatures.

# 5 Experiments to design calorimetric apparatus

The following series of experiments was used to design and refine techniques for calorimetric assessment of ESR in accordance with Eqs. (4) through (7). Readers uninterested in the preliminary designs may skip ahead to Section 5.6.

## 5.1 Experiment 0A: Measuring ESA of ruby crystal clear exposed on reclining chair

The temperature in the sun of ruby crystal clear was compared to those of three reference specimens: A10 (ruby crystal white), A1 (white), and A2 (gray#1). The support was the adjustable back of a reclining chair facing directly into the sun. A light beige towel was placed under the samples and over the chair's upholstered pad (ESM Figure A-3). The four specimens were laid out with 25 mm gaps along the width of the pad (560 mm), leaving about 90 mm of pad on each side of the array.

The temperature of the back of each specimen was measured with a thermistor and recorded with a data logger, as detailed in ESM Table A-1. The trial began about 13:00 local daylight time (LDT) on 2015-06-23 in Walnut Creek, CA, USA (clear sky, air temperature 31.6 °C, slight breeze). After a 15 minute warm up, an 11 minute period with fairly steady temperatures was chosen for analysis.

Two determinations of ESA for the ruby crystal sample were performed. Simple temperature interpolation with A1 (white) and A2 (gray #1) yielded an ESA of 0.262, which is close to that of A2 (0.267). However, since the convective heat transfer coefficient over the ruby crystal array might differ from that over a smooth painted metal panel, the ESA of the test specimen was also extrapolated from that of ruby crystal white, as follows. The ruby crystal sample was about 2.4 °C warmer than ruby crystal white (SA 0.231). We calculated the convective heat transfer coefficient over the ruby crystal white specimen by assuming  $I = 1050 \text{ W/m}^2$ ,  $h_r = 6 \text{ W/m}^2\cdot\text{K}$ , and  $T_r = T_a - 12 \text{ }^\circ\text{C}$ , then solving Eq. (1) to obtain  $h_c = 9 \text{ W/m}^2\cdot\text{K}$ . Using this convective heat transfer coefficient for ruby crystal clear, Eq. (1) was solved to find  $\rho_c = 0.264$ . The mean of the two determinations was 0.263, and thus the ESR is 0.737.

## 5.2 Experiment 0B: Assessing linearity of surface temperature vs. ESA with nine reference specimens exposed on reclining chair

To test the linear relationship between surface temperature and ESA required for use of Eq. (4), the temperatures of the nine painted metal reference specimens (A1 - A9) were measured at the same site and using the same support (reclining chair back plus towel) used in Experiment 0A. The nine specimens were arranged in a three by three array with about 2.5 cm spacing. The top

three samples were A1 - A3, with A4 - A6 in the middle, and A7 - A9 at bottom. The left and right margins were each about 14 cm.

On 2015-07-28 at 13:45 LDT (clear sky, air temperature 40 to 40.5 °C, calm), the specimens were placed on the support to warm up for 25 min. Their upper surface temperatures were then measured with an infrared thermometer eight times over the next 30 min, as detailed in ESM Table A-1. Median surface temperature varied nearly linearly with solar absorptance (Figure 7), supporting use of Eq. (4). The slight downward curvature in this plot is likely due to slight increases in the radiative and convective heat transfer coefficients with increasing temperature.

### **5.3 Experiment 1: Measuring ESA of ruby crystal panel exposed on three-specimen platform**

With the goal of creating a simple portable apparatus for reproducible calorimetric measurement of ESA, we built a 15 cm by 30 cm by 5 cm platform from white foam board (lightweight moisture-resistant low density polystyrene) with three specimen cavities, each 76 mm by 76 mm (Figure 8). Each cavity can support an optional quartz window (100 mm by 100 mm by 1.6 mm) above the specimen to reduce wind noise. A silicon pyranometer measures solar irradiance, while a handheld vane anemometer is used to measure wind speed. Thermistors were affixed to the back of each specimen with thermal paste and aluminum tape, as detailed in ESM Table A-1.

We made three versions of this platform, each with a uniform cavity depth of 6 mm (0.25"), 13 mm (0.5"), or 19 mm (0.75"). Trials were conducted at LBNL at various times between 10:50 and 15:40 LDT on sunny days in September 2015. In each trial, the test specimen was ruby crystal clear. One reference specimen was always A1 (white), and the second was either A2 (gray#1) or A3 (gray#2). The platform was oriented to face the sun (surface normal parallel to solar beam).

Figure 9 shows five different trials in which test specimen ESA was calculated from Eq. (4). The horizontal line shows the ESA measured in Experiment 0A (0.263). Trial 1A, using no window and the shallowest (6 mm) cavity, yielded an ESA only about 0.01 lower than that found in Experiment 0A, but with noticeable wind noise. Adding windows (Trial 1B) further lowered the estimate of ESA by about 0.06 without reducing noise. Retaining windows while increasing cavity depth to 13 mm (Trials 1C and 1E) or 19 mm (Trial 1F) eliminated window noise, but yielded ESAs about 0.02 to 0.03 lower than found in Experiment 0A.

Each quartz window is nonselective in the solar spectrum, with minimal absorption (absorptance < 0.01 from 300 to 2,500 nm) and essentially constant near normal-hemispherical solar spectral reflectance ( $0.06 \pm 0.01$ ). However, reflections at the air-window interfaces make the solar reflectance of a specimen measured through a quartz window differ from that observed without a quartz window (Levinson, Berdahl, & Akbari 2005). For example, for reference specimens A1 - A9 (Table 2),

$$\rho_{\text{with window}} = 0.82 \rho_{\text{without window}} + 0.06 \quad (14)$$

with coefficient of determination  $R^2 > 0.99$ ; differences ( $\rho_{\text{with window}} - \rho_{\text{without window}}$ ) range from about -0.06 to +0.08.

It may be possible to compensate for window reflectance by using Eq. (4) to compute the with-window ESA of the test specimen from the with-window SAs of the reference specimens, then calculating the without-window ESR of the test specimen by assuming that Eq. (14) applies to ESR. This approach would yield with-window ESAs of 0.27 to 0.32, with-window ESRs of 0.68 to 0.73, and without-window ESRs of 0.75 to 0.82 for ruby crystal clear in Trials 1B, 1C, 1E, and 1F. These ESRs are 0.01 to 0.08 higher than those found in Experiment 0A (ruby crystal clear on a reclining chair).

Windows can alter in other ways the relationship between SR (or ESR) and specimen temperature. For example, the coefficient of free convection over each specimen is a function of the difference between the temperature of the specimen and that of the air in the cavity [6]. The absence of forced convection over the specimen when a window seals the cavity makes the total (forced + free) convective coefficient  $h_c$  more dependent on specimen SA (or ESA) and temperature. This weakens the assumption underlying Eq. (4) that  $h_c$  is the same for all specimens. To minimize errors induced by variations in  $h_c$ , one would have to use reference specimens whose SAs closely bound the ESA of the test specimen.

## 5.4 Experiment 2: Measuring surface temperatures of non-fluorescent specimens on five-specimen platform

To explore the effects of wind-induced surface temperature fluctuations measured without protective windows, we measured the temperatures of non-fluorescent metal specimens on several different platforms. Six trials, 2A - 2F, were conducted at LBNL on sunny but often windy days in October 2015, between 11:40 and 16:00 LDT. Trials 2A - 2C exposed a set of five duplicate 50 mm by 50 mm green specimens (SA 0.88), while Trials 2D - 2F tested a set of five different 50 mm by 50 mm specimens (SAs 0.72, 0.73, 0.77, 0.88, 0.96).

Trial 2A arranged the five duplicate specimens in two rows at the center of a 36 cm by 38 cm by 2.5 cm foam board; Trial 2B arranged them in one row on a 20 cm by 61 cm by 2.5 cm foam board; and Trial 2C set them in a cavity array (9 cm by 9 cm, 25 mm deep). Trial 2D exposed the five different specimens as in Trial 2B; Trial 2E added a parapet-style wind break (25 mm height, 5 cm from the specimen row) to the Trial 2D setup; and Trial 2F exposed these five different specimens exposed as in Trial 2C (ESM Figure A-4).

The platform was oriented to face the sun. After a 10 minute warm up, specimen temperatures were recorded every 10 seconds for a period of 20 minutes.

Trials 2A - 2C yielded temperature range (max - min) values of about 1 to 2 °C. Trials 2D - 2F yielded surface temperatures that generally increased with solar absorptance, but with much more noise and less linearity than observed on a calm day in Experiment 0B (Figure 7).

The slopes of the lines fit to  $T$  vs.  $\alpha$  in Figure 7 range from 31.4 to 42.1 °C per unit change in solar absorptance. We can use these slopes to relate error in ESA to error in measured surface temperature. For example, in Experiment 0B or Experiment 2D, an error of 1 °C would change ESA by 0.027.

### **5.5 Experiment 3: Measuring surface temperatures of non-fluorescent specimens on rotating apparatus (early versions)**

Since specimen placement, especially distance from leading edge of platform to specimen, is expected to affect convective heat transfer coefficient, surface temperature, and finally estimation of ESA, we tried symmetrically arranging duplicate specimens on a rotating platform to make convection more uniform.

Our first approach manually rotated the square platform (33 cm by 33 cm by 2.5 cm) shown in ESM Figure A-5, which faced the sun. Trials 3A and 3B were conducted at LBNL on sunny afternoons in November 2015. Following a 10 minute warm up, each trial rotated the platform a quarter turn every 5 min for 20 minutes, with a data logger recording specimen temperatures every 10 seconds. At the end of Trial 3A, the time-averaged temperature range was 1.1 °C; at the end of Trial 3B, it was 0.4 °C (ESM Figure A-6).

Our second approach installed a circular platform of diameter 30 cm on the platter of a phonographic turntable (Figure 10). The platform was horizontal and revolved at 0.55 Hz (33 RPM). As in previous trials, the specimens were allowed a 10 minute warm up period. In Trial 3C, conducted at LBNL on a sunny, calm late morning in January 2016, the time-averaged temperature range over a 6 minute measurement period was 0.4 °C (Figure 11).

### **5.6 Experiment 4: Measuring surface temperatures of non-fluorescent specimens on first programmable rotating platter**

We built a rotating platter that holds six specimens, and positions each in turn under a fixed infrared thermometer. The first version of this programmable apparatus measured the temperature of each specimen for several seconds, recorded the final value, then quickly rotated the platter to bring the next specimen into the thermometer's narrow field of view.

The platter, a 5.1 cm thick, 45 cm diameter slab of expanded polystyrene (EPS) foam adhered to a thin aluminum plate, was rotated by a computer-controlled electric stepper motor. The angular position of the platter was continuously measured with a shaft-mounted goniometer to

provide closed-loop control of platter rotation. Up to six specimens, each 50 to 75 mm on a side, could be placed at 60° intervals on the surface of the platter, which in turn was faced into the sun (ESM Figure A-7). The operator could specify (a) the duration and speed of pre-measurement “spin-up” revolutions; (b) the number of measurement revolutions; (c) the duration of each temperature measurement; and (d) the speed with which to rotate the platter to bring the next specimen under the thermometer.

We conducted four trials, 4A – 4D, in April 2016. In each trial, the platter was spun at 30 RPM for 10 minutes to minimize any pre-trial differences in specimen temperature that might result from spatial variations in convection coefficient or solar irradiance. Next, over a series of 20 to 40 revolutions, the platter was rotated in increments of 60° to bring each specimen under the thermometer. Specimen temperature was recorded after 4 to 5 seconds of measurement. The platter was then rotated for about 2 sec to bring the next specimen into view.

Trials 4A and 4B exposed six duplicate green specimens—the same as those used in Experiments 2 and 3—on April 15 (sunny) and April 18 (intermittently cloudy, and windier), respectively. Trial 4B temperature and solar irradiance time series are shown in ESM Figure A-8. Trial 4A yielded time-averaged temperatures with a range of 0.18 °C after 40 revolutions, while Trial 4B yielded a range of 0.74 °C after 35 revolutions (ESM Figure A-9).

Trials 4C and 4D exposed reference specimens A1 (white), A2 (gray #1), A3 (gray #2), A4 (gray #3), A7 (gray #6), and A9 (black) on April 15 and April 18, respectively. Trial 4D temperature and solar irradiance time series are shown in Figure 12. While instantaneous temperatures fluctuated over the course of each trial, time-averaged surface temperatures varied linearly with solar absorptance (Figure 13).

## **5.7 Upgrading the programmable rotating platter to create final apparatus**

After Experiment 4, we improved the capabilities and performance of the programmable rotating platter by changing its drive motor, expanding its suite of local weather sensors, and upgrading its electronics and control software. These improvements made it substantially easier to operate the apparatus and to use its measurements to assess ESR.

First, we smoothed the rotation of the platter by replacing its stepper motor drive with a variable-speed DC motor drive. This reduced the tendency of the platter to vibrate when its motion is halted, and increased the accuracy with which each specimen can be positioned below the IR thermometer. Second, we added a three-cup anemometer to measure local wind speed, and a shaded thermistor to measure ambient air temperature. Third, we replaced the handheld data logger with a computer-controllable, multifunction data acquisition (DAQ) device. This increased the accuracy of sensor signal digitization and made all measurements immediately available to the apparatus control software. Fourth, we upgraded the control software (Python code executed on a Windows PC) to (a) better regulate the motion of the platter; (b) capture

specimen temperature, weather, and platter angle at the end of each specimen measurement; and (c) record to a file the time-stamped instantaneous specimen temperature and weather measurements, along with cumulative mean specimen temperatures, as they are captured.

The final apparatus is shown in Figure 14 and detailed in ESM Table A-1. A video of the platter motion is presented in the Electronic Supplementary Material.

## 6 Measurement of ESR with final apparatus

In Experiment 5 (September 2016), we used the final apparatus to measure the ESRs of ruby crystal clear and the five fluorescent ruby-pigment coatings.

### 6.1 Methodology

We conducted 30 trials at LBNL with the upgraded apparatus in late September 2016. The fluorescent specimens were grouped with non-fluorescent reference specimens to form four test sets (A – D). Set A compared the 0.2%, 1%, and 2% coatings to references A1 (white), A2 (gray#1), and A3 (gray#2), while Set B compared the fluorescent 2%, 3%, and 4% coatings to the same three references. Note that the 2% coating was present in both Set A and Set B.

Set C compared ruby crystal clear to references A10 (ruby crystal white) and A11 (ruby crystal gray). Set D was Set C plus the 2% coating and references A1 (white) and A2 (gray#1) (Figure 15). Set E, comprised of references A1 (white), A2 (gray#1), A3 (gray#2), A4 (gray#3), A7 (gray#6), and A9 (black) was measured to verify that the reference temperatures varied linearly with solar absorptance.

Sets A, B, and C were tested facing the sun in Trials 5A – 5C, 5D – 5F, and 5G – 5I, respectively, then tested horizontally with solar elevation angles of 45 to 52° in Trials 5J – 5L, 5M – 5O, and 5P – 5R. Set D was tested horizontally in extended Trial 5S, a series of 10 subtrials (5S/i through 5S/x) in which the solar elevation angle ranged from 18° to 49°. Set E temperatures were measured facing the sun in Trial 5T, then horizontally in Trial 5U.

Each trial included a 10 min spin up at about 8 RPM, except in extended Trial 5S, where spin-up time was reduced to 1 min when the gap between consecutive subtrials was less than 10 min. With the exception of Trial 5U, which was briefer, each trial (or subtrial) included about 25 to 50 measurement revolutions (Table 3). In the measurement phase, the apparatus held each specimen under the IR thermometer for 5 seconds before spinning the platter at about 6 RPM to bring the next specimen into view.

The ESA and ESR of each specimen was calculated following Eqs. (5) through (7). Its fluorescence benefit (ESR – SR) was calculated by subtracting its AM1GH solar reflectance from its sun-facing ESR.

## 6.2 Results

Figure 16 illustrates the output of the apparatus with the time series of solar irradiance, wind speed, air temperature, and instantaneous and cumulative mean specimen temperatures measured in Trial 5C.

Figure 17 shows how the ESA of each fluorescent test specimen in Trials 5D – 5F was determined by locating its final mean temperature on a line fit through the final mean temperatures and pure SAs of the non-fluorescent references. Similar plots for all trials involving fluorescent specimens (5A – 5R) are presented in ESM Figure A-10.

Specimen ESRs are reported by trial in Table 3 and summarized in Table 4. Mean ESR measured horizontally was 0.047 higher than mean ESR measured facing the sun for ruby crystal clear, and 0.021 to 0.031 higher for the coatings. For a given specimen and orientation, ESR sample standard deviation ranged from 0.002 to 0.023.

The variations with solar beam incidence angle of the ESRs of the 2% coating and of ruby crystal clear are shown in Figure 18.

The linear variation with pure SA of the final mean temperatures of non-fluorescent reference specimens is shown in ESM Figure A-11.

## 7 Discussion

### 7.1 Radiometric measurement techniques

Two of the radiometric ESR measurement techniques (pyranometer methods E1918, requiring a sample at least 4 m by 4 m; and E1918A, requiring a sample about 1 m by 1 m) are promising for rating commercial products once available at large scale, but not for measuring the ESR of small prototype specimens (about 10 cm by 10 cm). The combination of a pyrhelimeter and pyranometer may work to characterize small specimens if the ratio of signal to noise can be improved.

It may be possible to calibrate the input and output of a spectrofluorometer to provide absolute measurement of the effective spectral reflectance of a small specimen. Such an instrument would not have to cover the entire solar spectrum so long as it includes all excitation and emission wavelengths. Pure reflectance at non-excitation wavelengths could be assessed with a traditional spectrophotometer.

### 7.2 Calorimetric measurement techniques

From the calorimetric measurement design experiments we have made the following observations.

1. The temperatures of stationary reference specimens varied nearly linearly with SA on a calm, sunny day, validating the calculation of ESA by temperature interpolation of known SA values (Experiment 0B).
2. ESA can be measured in calm, sunny conditions (Experiment 0A).
3. Wind can induce variations of about 2 °C in duplicate specimen surface temperature if the specimens are stationary and unshielded (Experiment 2).
4. Shielding specimens with a window removes convection noise, but yields ESA different from that measured with unshielded specimens on a calm, sunny day (Experiment 1). Further heat transfer analysis would be required to correct for the radiative and convective influences of the windows.
5. Rotating the specimen platform and averaging the time series of specimen temperature measurements mitigates convection noise (Experiments 3 through 5).

Experiments 3 through 5 identified two useful rotary techniques: (a) continuous measurement of the temperature of each specimen with a contact thermometer, such as a thermistor, thermally connected to its back; and (b) intermittent measurement of the temperature of each specimen with a single IR thermometer that sees the face of each specimen in turn. Each has practical advantages and disadvantages.

Continuous measurements can be recorded with a small, standalone logger, so long as the logger can revolve with the platter. No computer control is required, since the platter can spin at a constant speed. Weather measurements can be collected with a second logger. The primary disadvantages to this method are that (a) the temperature sensors must be cross calibrated, ideally before each trial; (b) the temperature sensors must be joined to specimens with thermal paste to minimize thermal resistance; (c) this thermal resistance may grow if the sensor is dislodged; and (d) a standalone logger that can record and process thermistor and pyranometer signals tends to be expensive (about US\$1K). The first three issues can be managed. For example, one could use thermal epoxy, rather than thermal paste, to permanently bond an accurate but inexpensive thermistor (example: US Sensor KS103G2, 0.1 °C interchangeability, US\$5) to the back of each specimen, then cross-calibrate the sensors by measuring specimen temperatures when rotated in a dark room. As for the last issue, we note that the labor savings associated with this simple design may offset the investment in data logging equipment.

Intermittent measurements can be performed with a single, non-contact IR thermometer, removing the needs to cross calibrate multiple temperature sensors and thermally bond them to the specimens. This makes it easy to change specimens. Computer control of platter motion and data collection makes the system programmable and versatile, allowing systematic investigation of geometric and dynamic factors that may influence results. Analysis features built into the control software also reduce the need to post-process temperature measurements. On the other hand, even when the broadband thermal emittances of specimens

are matched, the use of an IR thermometer can complicate assessment of surface temperature if there are specimen-to-specimen variations in spectral emittance within the portion of the thermal IR detected by the sensor [14].

The intermittent-measurement apparatus is more complicated than that needed for continuous measurement. Substantial effort was required to design and build the electronics and software needed to intermittently rotate the platter, synchronize temperature measurements to platter motion, and communicate with the DAQ hardware. We note in particular that early attempts to use an inexpensive hobbyist microcontroller with integrated analog and digital I/O uncovered serious limitations in these microcontrollers, including limited range and resolution of analog input; lack of basic functionality, such as a battery powered clock to maintain system time; and incomplete, unsupported application program interfaces for both the microcontroller and its accessories, such as external analog-to-digital conversion integrated circuits. Most vexing of all, we discovered that some dedicated-function integrated circuits failed randomly. We resolved these problems by switching to a more expensive, but more robust, scientific-grade DAQ device.

### **7.3 ESR measurement repeatability and technique**

The Experiment 5 trials indicate that the final apparatus measures the ESR of a given specimen, in a given orientation, with a repeatability (sample standard deviation) of about 0.02.

In our earliest experiments with a clear-coated ruby array with sun normal to the sample, we found  $ESR = 0.737$ . At the conclusion of the present work we have  $ESR = 0.764$ . The difference, 0.027, is within the combined uncertainties of the two measurements and is indicative of the current state of the art. On the other hand, under favorable circumstances, the standard deviations (repeatability) obtained with the current apparatus is as small as 0.002, so there is room for further improvement.

The ESR of the ruby crystal clear was about 0.05 higher measured horizontally (solar incidence angle around  $50^\circ$ ) than when measured facing the sun. This may result from variations with beam incidence angle in specular reflectance from the clear-coated crystals. (The white- and gray-coated crystals appear matte.) A normally incident photon must be reflected twice before leaving the pyramid surface of the ruby crystal array, reducing net reflectance. For example, if the sloping top surface reflectance of a ruby crystal is 0.07, the net surface reflectance for a normally incident photon is only  $0.07 \times 0.07 = 0.0049$ . For incidence angles well away from normal the surface reflectance should be comparable to 0.07.

The ESR of the coatings was about 0.02 higher measured horizontally (solar incidence angle around  $50^\circ$ ) than when measured facing the sun. The reason for this variation is unclear, but is not surprising since reflectance often increases with incidence angle (Appendix A of Ref. [9]).

We recommend measuring ESR with specimens facing the sun, for three reasons. First, since pure solar reflectance is typically measured at near-normal incidence, measuring ESR at normal

(or near normal) incidence makes it easier to compute the fluorescence benefit (ESR – pure SR). Second, facing the sun provides a consistent incidence angle. Third, facing the sun maximizes the incident solar flux, increasing the ratio of signal (temperature rise induced by solar heat gain) to noise (temperature fluctuations induced by variations in convection).

If measuring ESR with specimens facing the sun, it may be desirable to compute the SRs of each spectrally selective surface with a sun-facing solar spectral irradiance, rather than with AM1GH. However, the difference in spectral power distribution between the sun-facing irradiance and the AM1GH irradiance, and the associated error in pure SR, may be small so long as the sun is not very low in the sky. For example, the near-infrared fraction of the ASTM Standard G173 air mass 1.5 global tilt solar spectral irradiance on a 37° surface rotated toward the sun (G173GT; solar altitude angle 41.8°, solar beam incidence angle 4.8°) is 0.518, which is only 0.031 (6.4%) greater than the 0.487 near-infrared fraction of AM1GH [9]. If the NIR reflectance of a highly selective surface exceeds its UV/visible reflectance by 0.40, its G173GT solar reflectance will be only 0.012 higher than its AM1GH solar reflectance.

## 7.4 Other applications

Our calorimetric technique could also be applied to other special surfaces, including directionally selective reflectors (DSRs) used as cool envelope materials. The solar reflectance of a DSR, such as a retroreflector, or a roofing product that looks white from the sky and dark from ground level, is inconvenient to measure with a conventionally configured spectrophotometer that provides only near-normal irradiance. It could be measured at any solar incidence angle using our calorimetric technique, though measurement at incident angles approaching 90° may substantially reduce the ratio of signal to noise.

## 8 Summary

Test methods are needed to evaluate the abilities of surfaces colored with fluorescent cool pigments to reject incident sunlight by the combination of reflection and fluorescence. Our review of radiometric techniques for the measurement of effective solar reflectance suggests that two pyranometer methods (E1918A, E1918) could be applied to large or very large specimens, and that a suitably calibrated spectrofluorometer fitted with an integrating sphere could measure the effective spectral reflectance of a small specimen.

We have tested a variety of calorimetric techniques for using temperature in the sun to interpolate the effective solar absorptance of a test specimen from the known solar absorptances of non-fluorescent reference specimens. Our experiments showed that averaging out noise in the temperature signal induced by variations in convection is key.

We have developed a computer-controlled rotary apparatus that compares the temperatures in the sun of up to six specimens. Trials on six different fluorescent specimens indicate that it can measure ESR with a repeatability of about 0.02. To maximize the ratio of signal to noise in

temperature determination, and to facilitate calculation of the fluorescence benefit, measurements should be performed with specimens facing the sun.

This apparatus could also be used to assess the solar reflectance of directionally selective reflectors that are difficult to characterize with conventional laboratory instruments.

## Acknowledgements

This work was supported by the Assistant Secretary for Energy Efficiency and Renewable Energy, Office of Building Technology, State, and Community Programs, of the U.S. Department of Energy under Contract No. DE-AC02-05CH11231; and by the California Energy Commission (CEC) through its Electric Program Investment Charge (EPIC). We also wish to thank Howdy Goudy of Lawrence Berkeley National Laboratory for assistance with electronics; Katerina Tsou of Michigan State University for her contributions to measurements; and Victor Cassella of Kipp & Zonen for loan of an SP Lite2 pyranometer.

## References

- [1] R. Levinson, P. Berdahl, H. Akbari, W. Miller, I. Joedicke, J. Reilly, Y. Suzuki and M. Vondran, "Methods of creating solar-reflective nonwhite surfaces and their application to residential roofing materials," *Solar Energy Materials & Solar Cells*, vol. 91, pp. 304-314, 2007.
- [2] M. Zalich and B. Kornish, "Fluorescent pigments for high-performance cool roofing and facades," 2016.
- [3] P. Berdahl, S. Chen, H. Destailats, T. Kirchstetter, R. Levinson and M. Zalich, "Fluorescent cooling of objects exposed to sunlight - the ruby example," *Solar Energy Materials & Solar Cells*, vol. 15, p. 312-317, 2016.
- [4] P. Berdahl and S. Bretz, "Preliminary survey of the solar reflectance of cool roofing materials," *Energy & Buildings*, vol. 25, pp. 149-158 (Figures 11, 12), 1997.
- [5] J. Yuan, K. Emura and C. Farnham, "A method to measure retro-reflectance and durability of retro-reflective materials for building outer walls," *Journal of Building Physics*, vol. 38, no. 6, p. 500-516, 2015.
- [6] F. White, *Heat and Mass Transfer*, Addison-Wesley, 1988.
- [7] ASTM, ASTM C1371-15: Standard Test Method for Determination of Emittance of Materials Near Room Temperature Using Portable Emissometers, ASTM International, 2015.

- [8] ASTM, ASTM E903-12: Standard Test Method for Solar Absorptance, Reflectance, and Transmittance of Materials Using Integrating Spheres, ASTM International, 2012.
- [9] R. Levinson, H. Akbari and P. Berdahl, "Measuring solar reflectance—Part I: defining a metric that accurately predicts solar heat gain," *Solar Energy*, vol. 84, pp. 1717-1744.
- [10] R. Levinson, H. Akbari and P. Berdahl, "Measuring solar reflectance—Part II: review of practical methods. Solar Energy," *Solar Energy*, vol. 84, pp. 1745-1759, 2010.
- [11] O. Hadley and T. Kirchstetter, "Black-carbon reduction of snow albedo," *Nature Climate Change*, vol. 2, no. 6, pp. 437-440, 2012.
- [12] ASTM, ASTM E1918-06(2015): Standard Test Method for Measuring Solar Reflectance of Horizontal and Low-Sloped Surfaces in the Field, ASTM International, 2015.
- [13] H. Akbari, R. Levinson and S. Stern, "Procedure for measuring the solar reflectance of flat or curved roofing assemblies," *Solar Energy*, vol. 82, pp. 648-655, 2008.
- [14] Micro-Epsilon, "Basics of Non Contact Temperature Measurement," 2016. [Online]. Available: <http://www.micro-epsilon.com/download/products/dat--infrared-basics--en-us.pdf>. [Accessed 3 October 2016].
- [15] ASTM, ASTM C1549-09(2014): Standard Test Method for Determination of Solar Reflectance Near Ambient Temperature Using a Portable Solar Reflectometer, ASTM International, 2014.
- [16] CRRC, "Rated Products Directory," Cool Roofing Rating Council, Oakland, CA, USA, 2016. [Online]. Available: <http://coolroofs.org>.
- [17] R. Levinson, P. Berdahl and H. Akbari, "Solar spectral optical properties of pigments, part I: Model for deriving scattering and absorption coefficients from transmittance and reflectance measurements," *Solar Energy Materials & Solar Cells*, vol. 89, pp. 319-349, 2005.

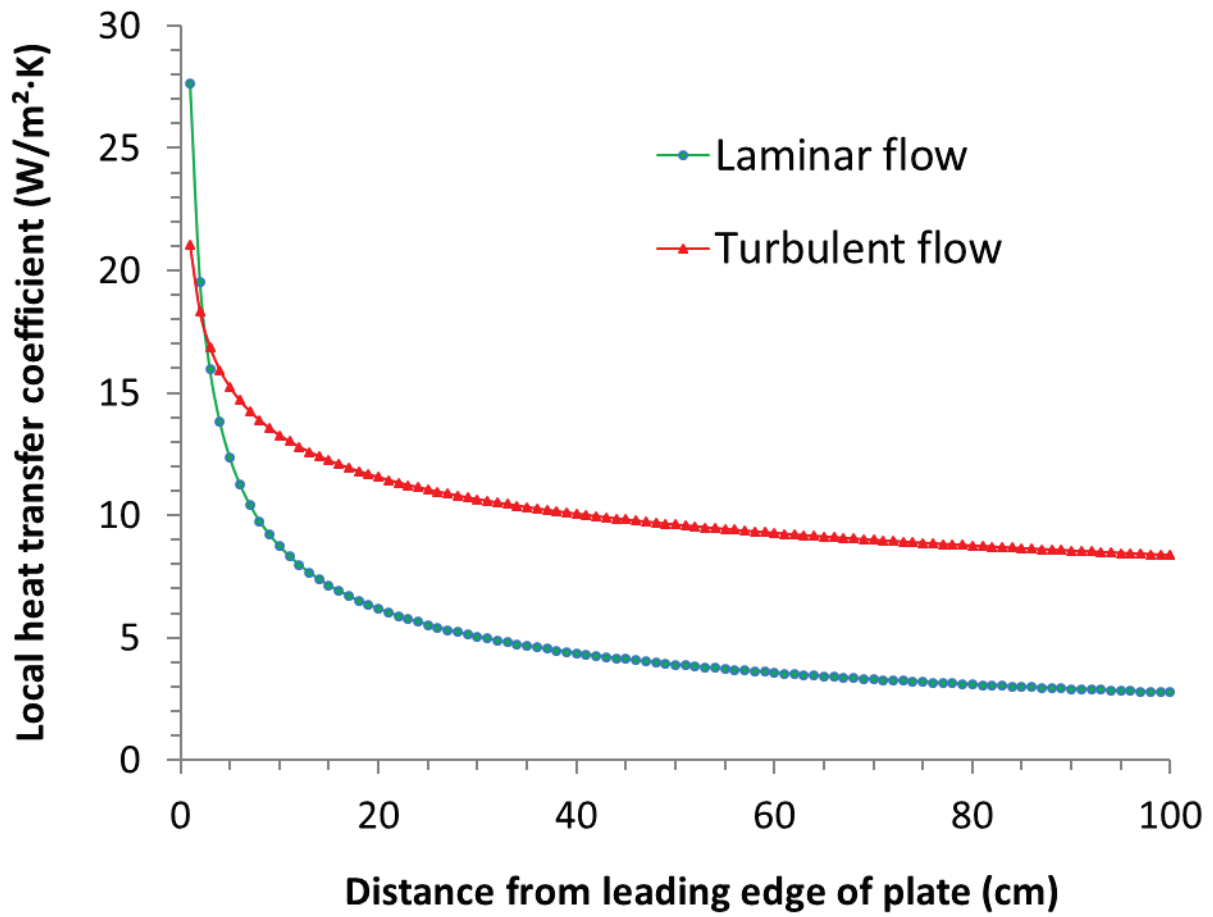
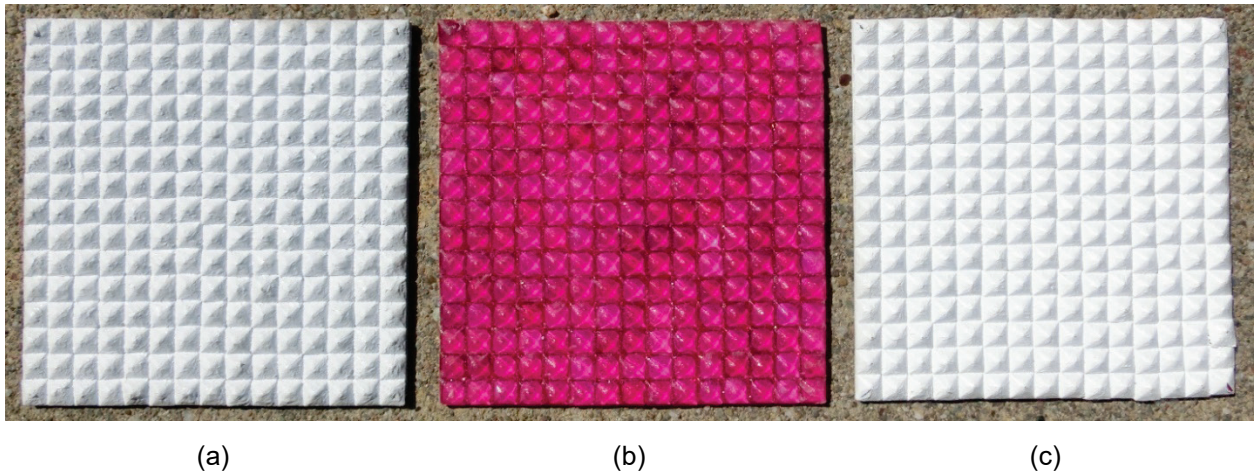


Figure 1. Variations with distance from leading edge of plate of laminar and turbulent local forced convective heat transfer coefficients, calculated for a free-stream wind speed of 2 m/s. At that speed, flow is laminar (local Reynold's number < 500,000) for the first 400 cm.



**Figure 2.** Images of 75 mm by 75 mm ruby crystal specimens overcoated with (a) gray acrylic paint (“ruby crystal gray”), (b) clear acrylic paint (“ruby crystal clear”), or (c) white acrylic paint (“ruby crystal white”). The gems are set in a thick layer of bright white artist paint on an aluminum substrate.



**Figure 3.** Images of 75 mm by 75 mm ruby-pigment coatings with 0.2%, 1%, 2%, 3%, or 4% weight fractions of chromium oxide present in the alumina pigment.

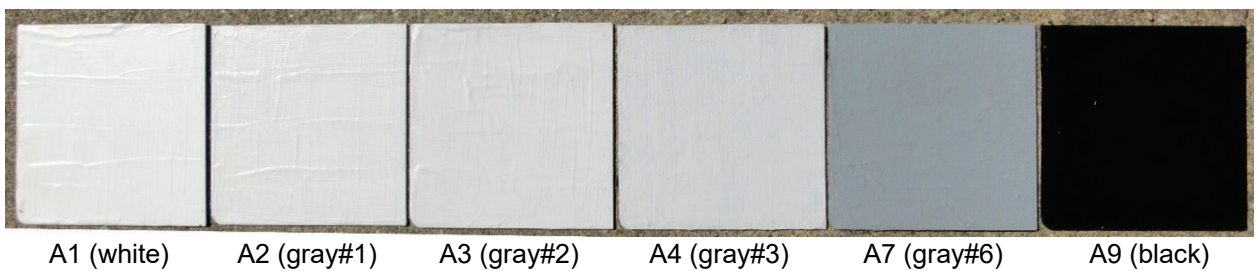


**Figure 4.** Images of six of the painted metal panels (A1 – A9) used as non-fluorescent reference specimens: A1 (white), A2 (gray#1), A3 (gray#2), A4 (gray#3), A7 (gray#6), and A9 (black). Each panel is 75 mm by 75 mm.

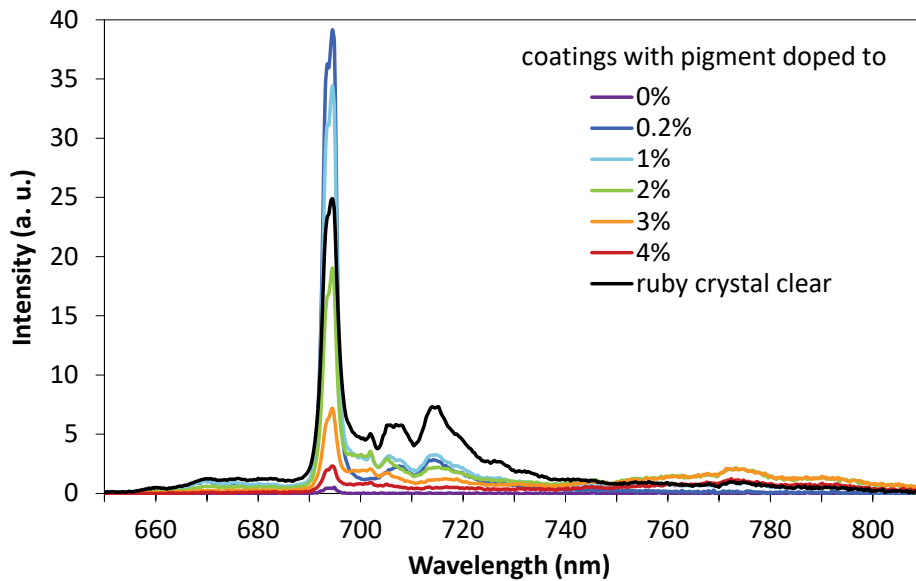


Figure 5. Fluorescence spectra obtained with the LBNL spectrofluorometer of highly-pigmented ruby coatings with  $\sim 500 \text{ g m}^{-2}$  of 0 to 4 wt%  $\text{Cr}_2\text{O}_3$ -doped  $\text{Al}_2\text{O}_3$ , and of the ruby crystal clear.

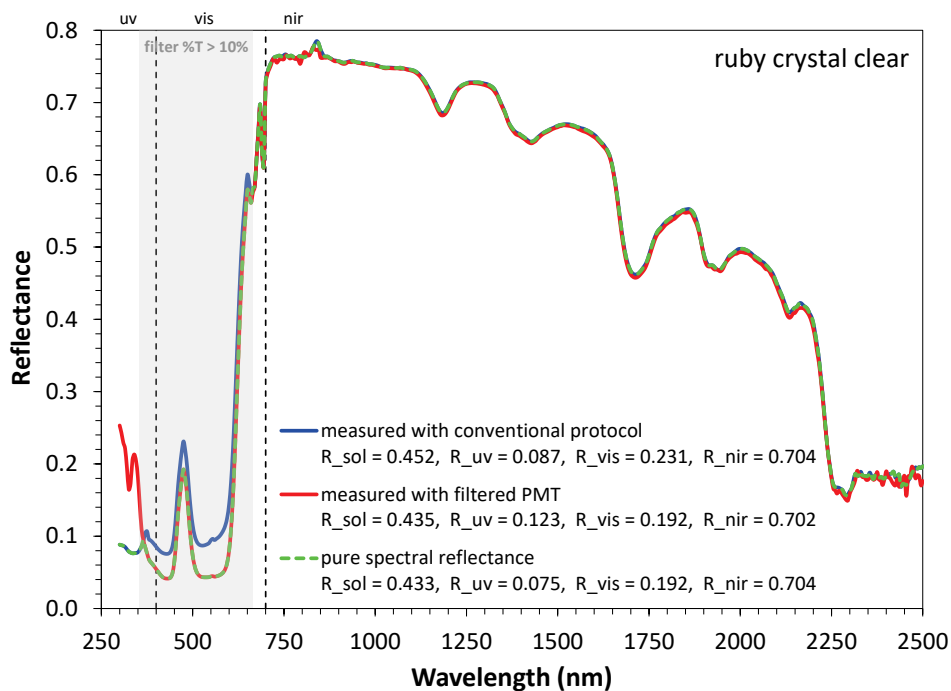


Figure 6. Solar spectral “effective” reflectance (blue curve, measured without correction) and solar spectral reflectance (red curve, measured by filtering emission) of ruby crystal clear. Pure spectral reflectance (dashed green curve) uses filtered data where filter transmittance exceeds 10%, and non-filtered data at other wavelengths. Each spectrum was obtained with a UV-vis-NIR spectrophotometer with integrating sphere. The effective reflectance spectrum will be inaccurate if instrument response at emission wavelengths differs from that at excitation wavelengths.

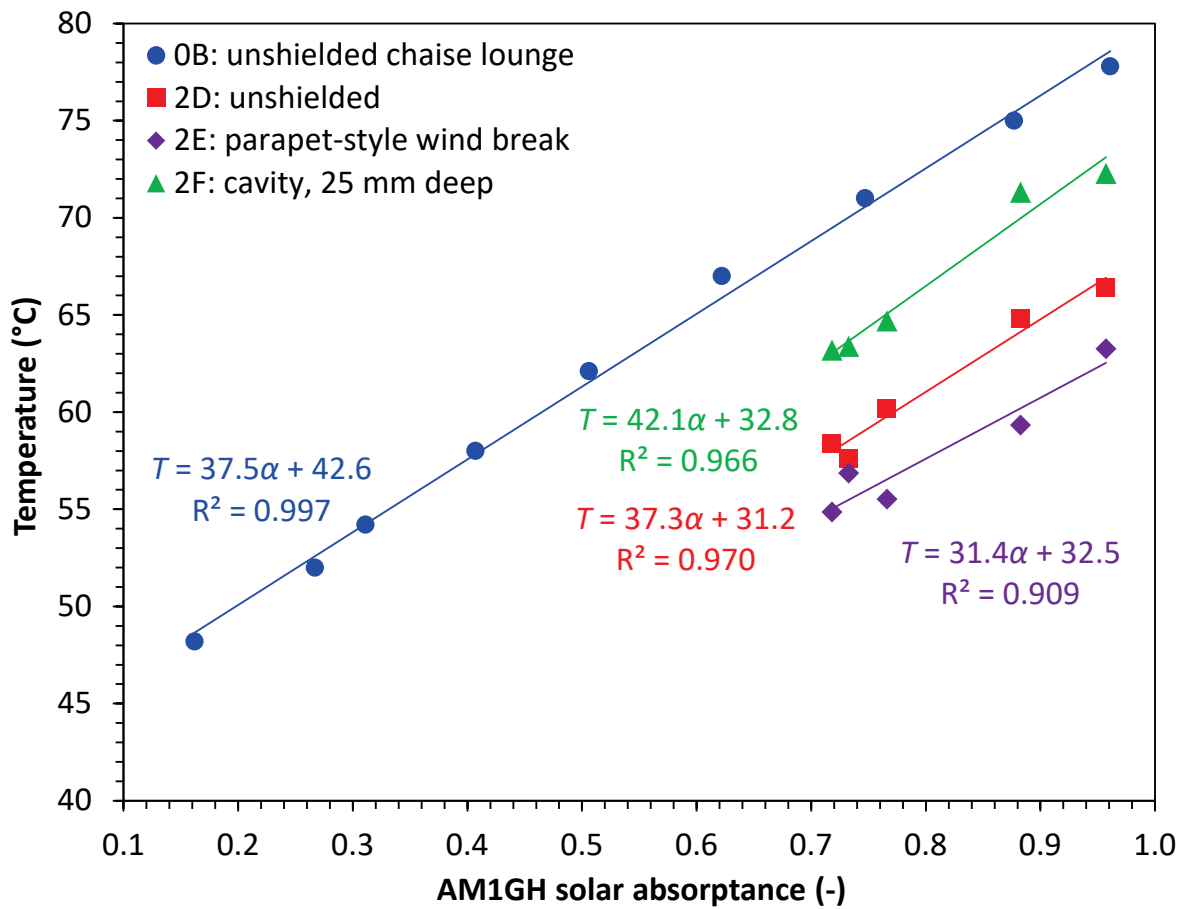
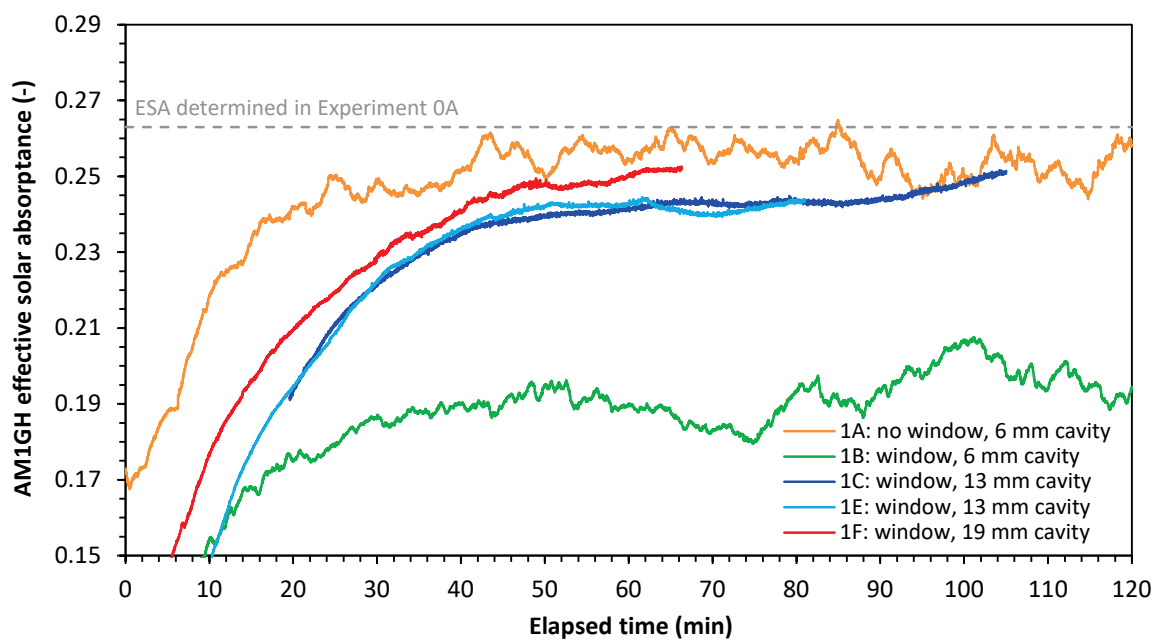


Figure 7. In experiment 0B, the median surface temperatures of nine non-fluorescent painted metal panels (reference specimens A1 – A9) varied nearly linearly with solar absorptance on a sunny, calm afternoon in July 2015. Also shown are variation of time-averaged surface temperature with solar absorptance of non-fluorescent specimens tested in Experiment 2, Trials 2D – 2F, conducted on sunny days in October 2015.



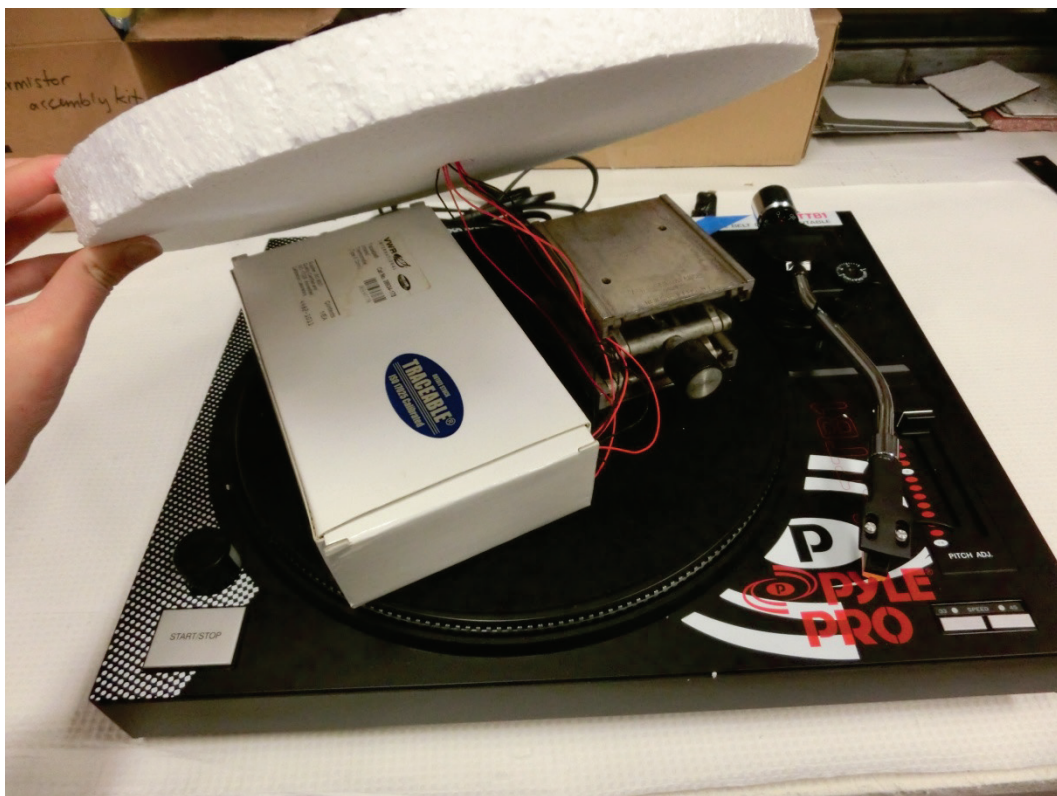
Figure 8. Three-cavity insulated apparatus used to measure the ESA of ruby crystal clear (center cavity). Image also shows the pyranometer and anemometer used to measure solar irradiance and wind speed.



**Figure 9. Effective solar absorptance of ruby crystal clear interpolated from solar absorptances of white (A1) and either gray#1 (A2) or gray#2 (A3) reference specimens, using temperatures measured with several versions of the Experiment 1 apparatus.**



(a)



(b)

**Figure 10. Images of a continuously rotating platform on a phonographic turntable, including (a) a top view showing four duplicate specimens, and (b) a look under the hood. The four specimens are spaced 5 cm from each other, and 3.8 cm from the platform edge.**

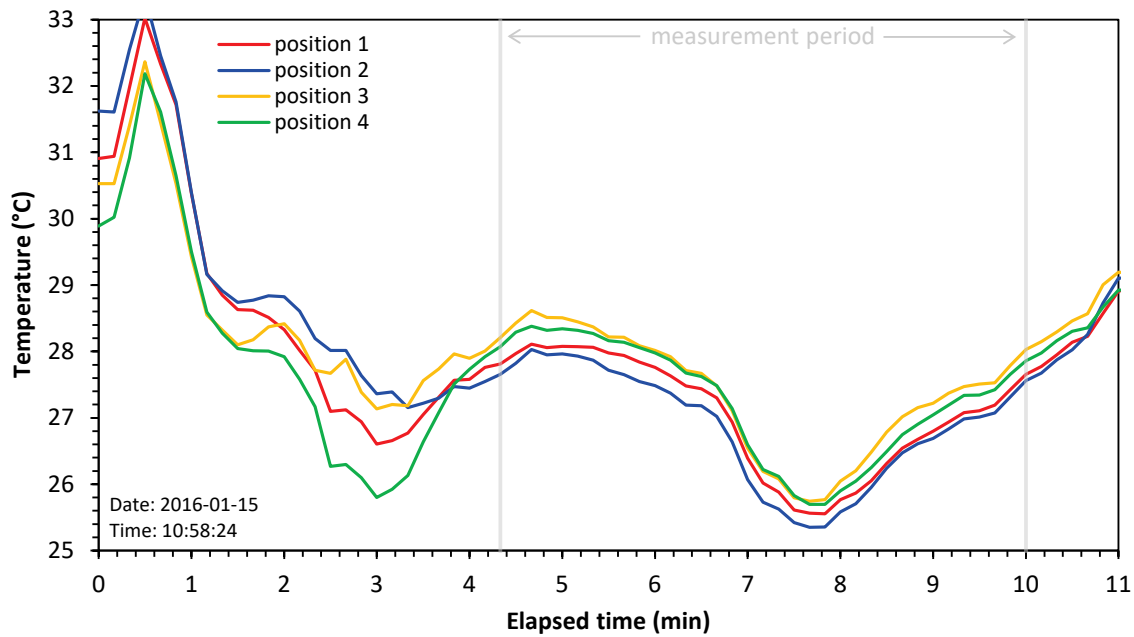


Figure 11. Surface temperatures of duplicate non-fluorescent specimens measured on a platform revolving at 33 RPM, measured in Trial 3C of Experiment 3. Outside air temperature was about 18 °C.

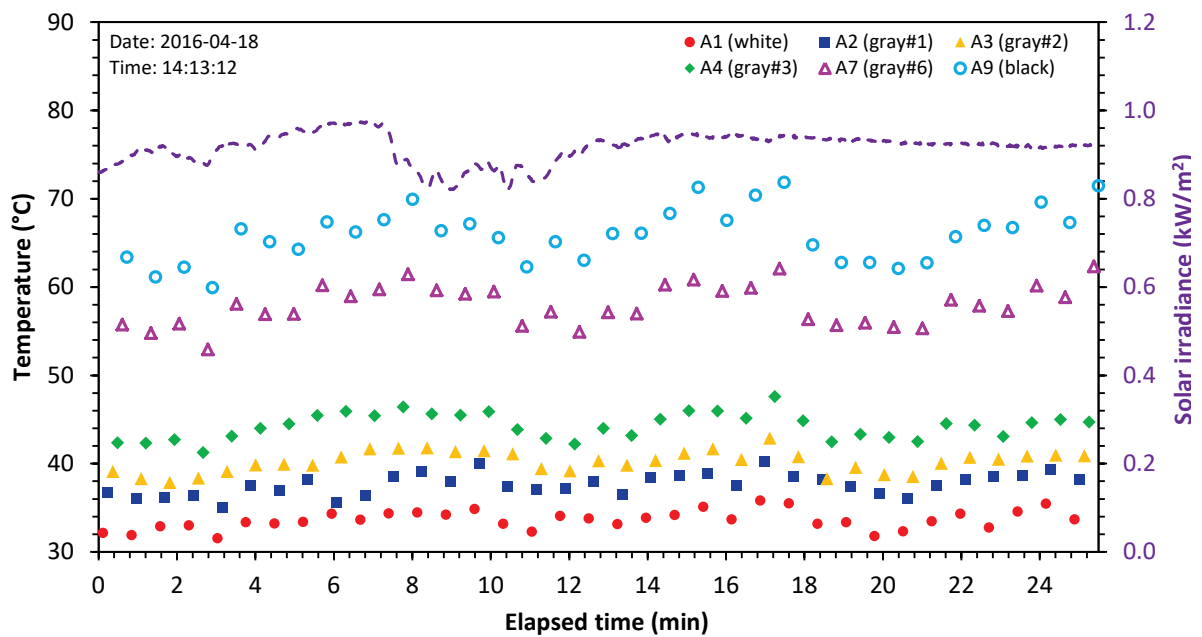
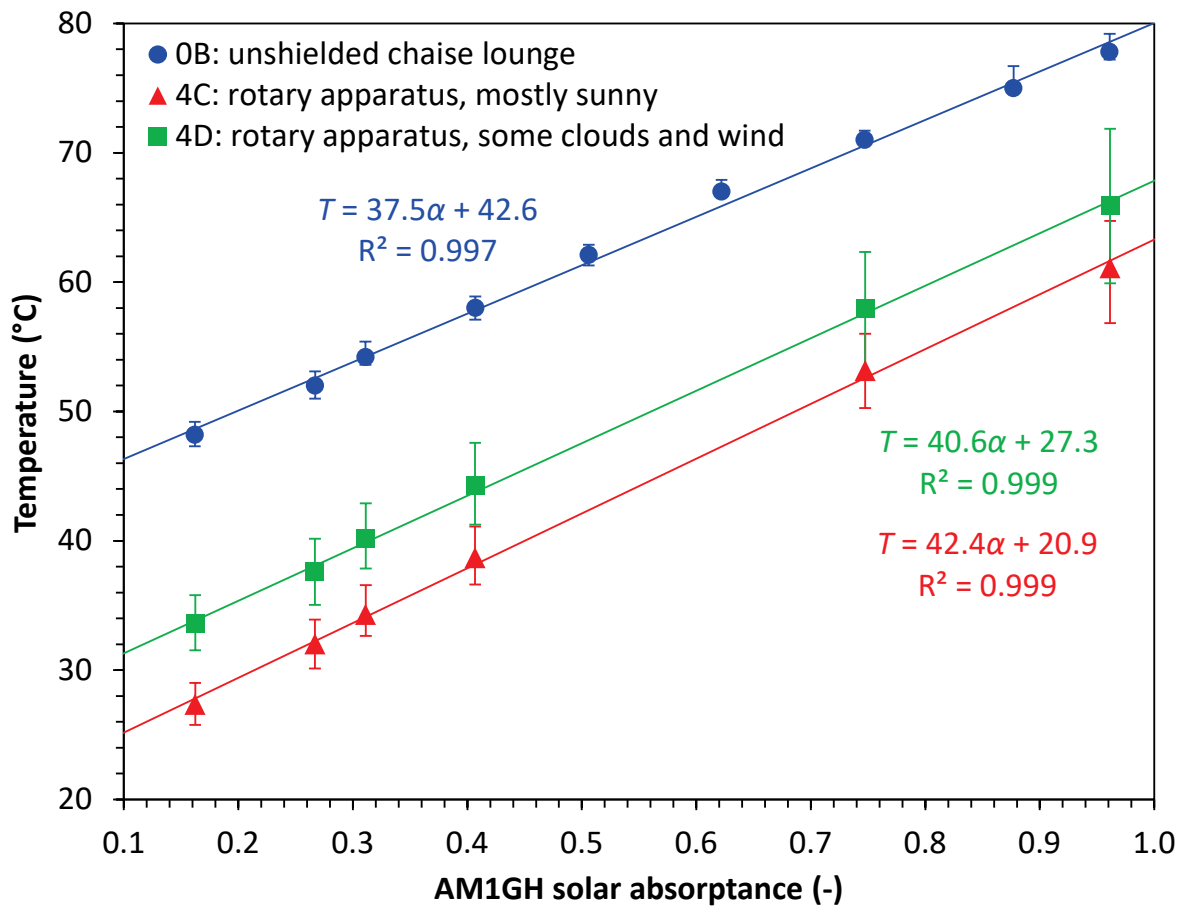


Figure 12. Instantaneous surface temperatures of six non-fluorescent reference specimens measured with the initial programmable rotary apparatus in Trial 4D. Also shown is global horizontal solar irradiance.



**Figure 13. Variation with solar absorptance of the time-averaged temperatures of six gray-scale reference specimens (L to R: A1, A2, A3, A4, A7, and A9) measured with the initial programmable rotary apparatus in Trials 4C and 4D (April 2016). Also shown for comparison are the temperatures of all nine gray-scale reference specimens (L to R: A1 – A9) in Trial 0B (June 2015). Error bars bound low and high values.**



**Figure 14. Photo of final apparatus, including rotating platter, IR thermometer (upper right), anemometer (lower left), pyranometer (on same board as anemometer), and control electronics (underneath tripod). The air temperature sensor is hidden below the platter.**

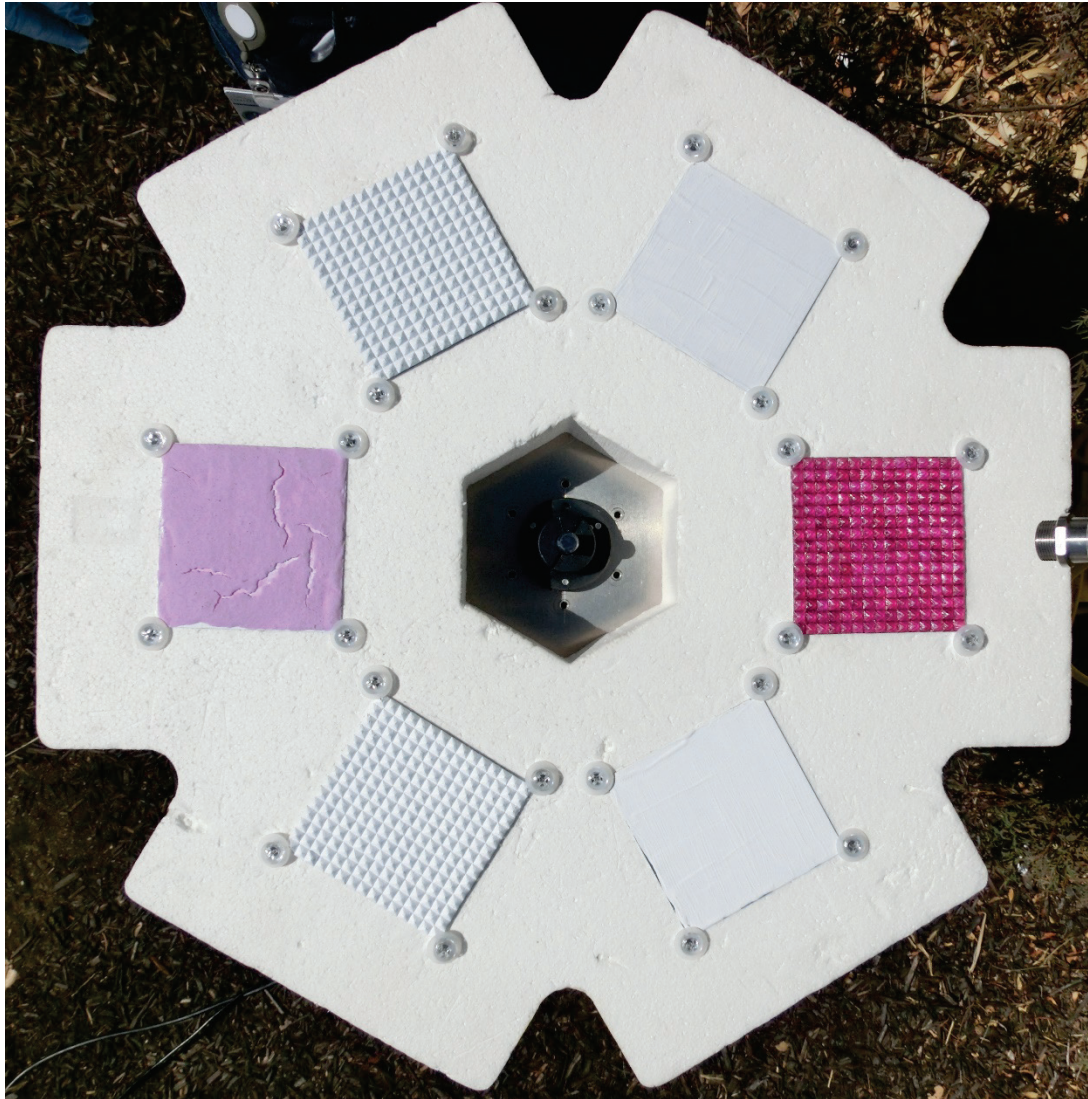
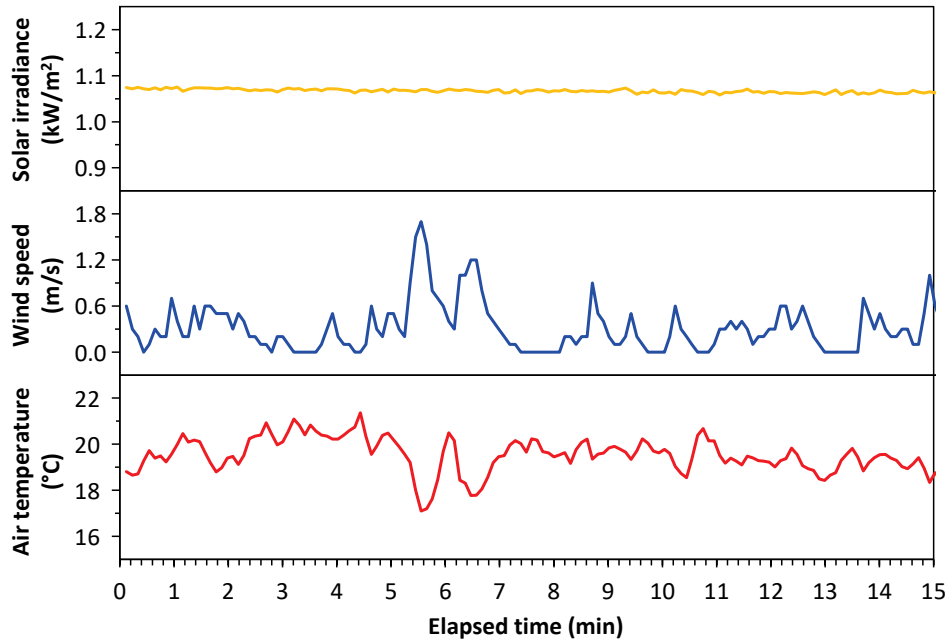
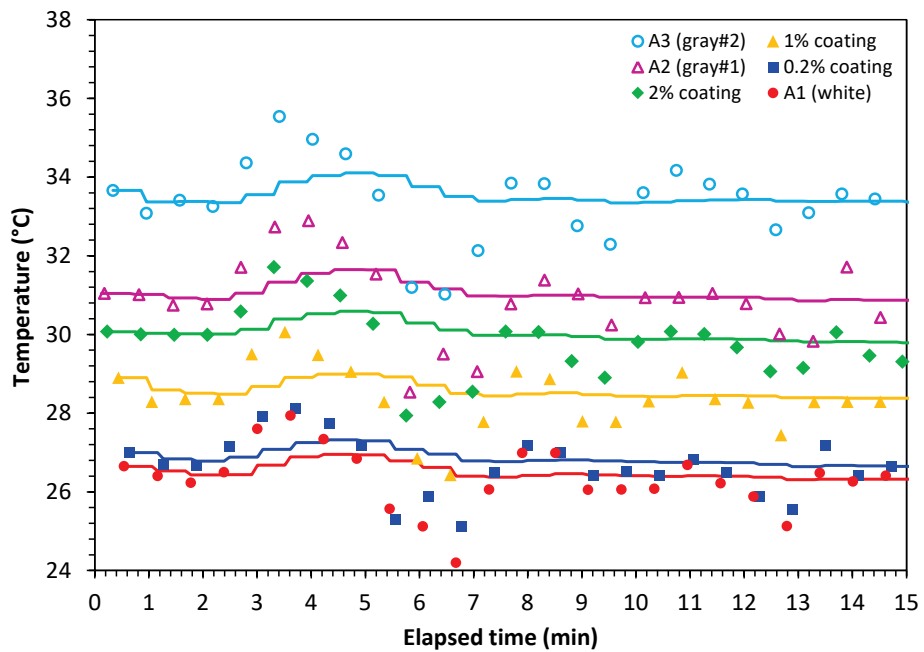


**Figure 15. Top view of Set D on the platter. Clockwise from left: 2% coating, ruby crystal gray, A2 (gray#1), ruby crystal clear, A1 (white), and ruby crystal white.**



(a)



(b)

**Figure 16. Time series of (a) weather and (b) specimen temperatures measured during Trial 5C. In panel b, symbols are instantaneous values and lines are cumulative means.**

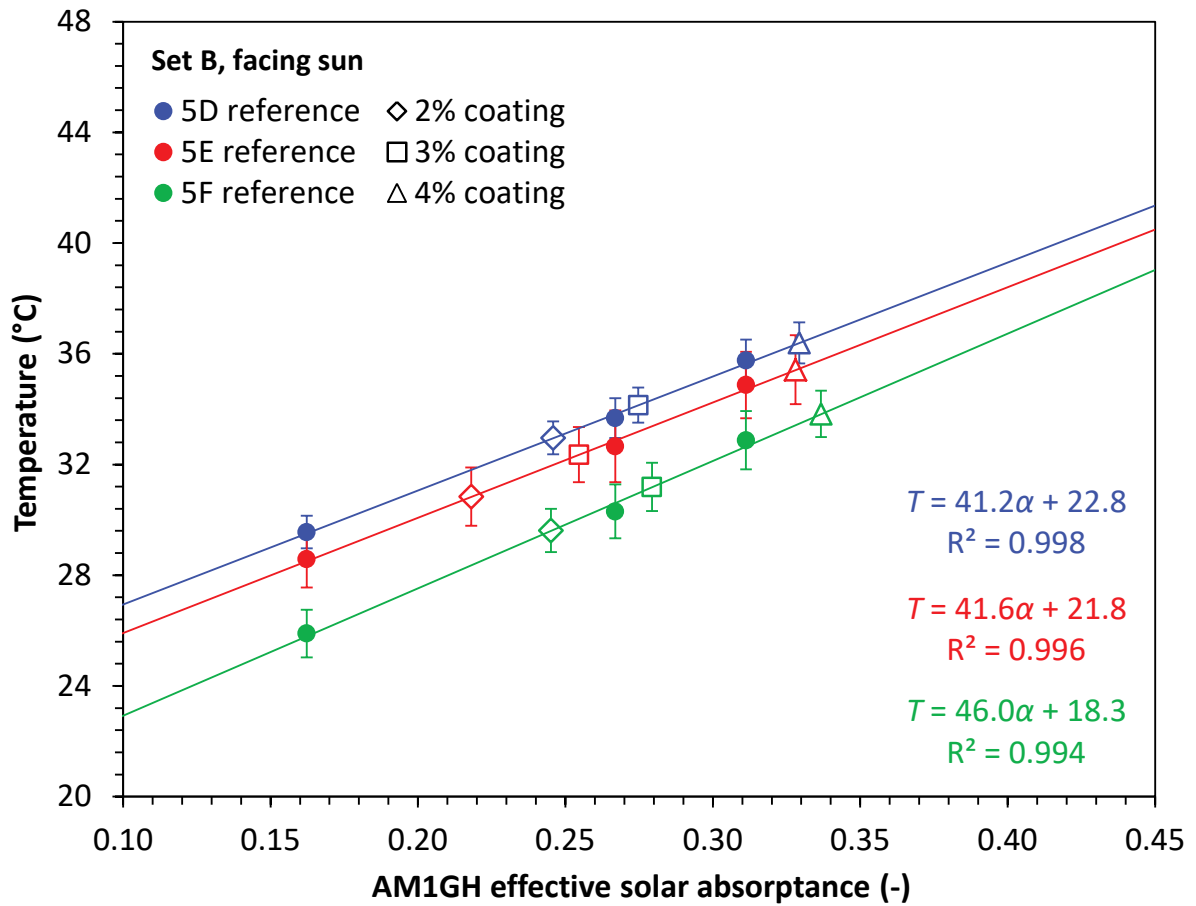


Figure 17. Determination of test specimen ESA from final mean temperatures of test and reference specimens, shown for Trials 5D – 5F (Set B, facing sun).

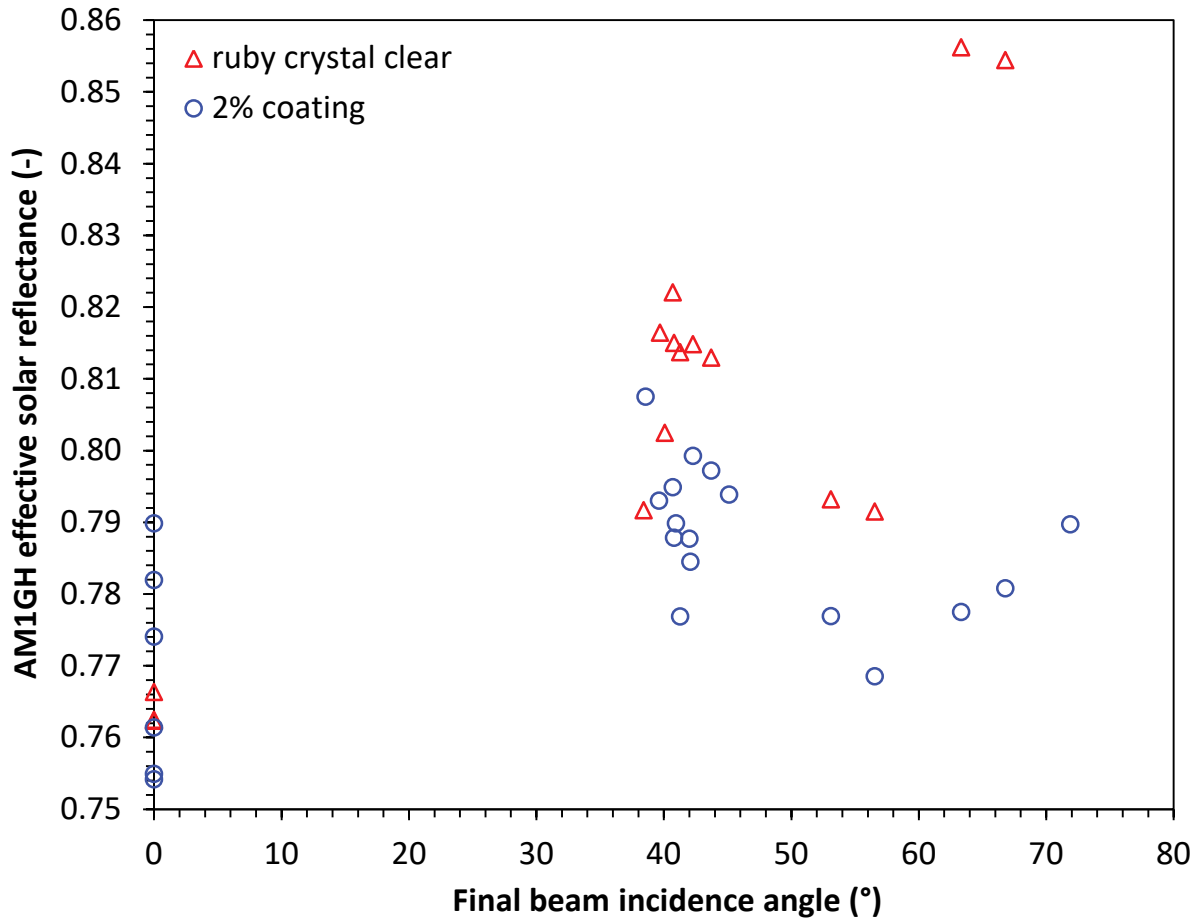


Figure 18. Variation of ESR with solar beam incidence angle for ruby crystal clear and 2% ruby coating.

Table 1. Radiative properties of fluorescent test specimens.

Description	Specimen thickness (mm)	Thermal emittance	Pure AM1GH solar reflectance w/o window
0.2% coating	1.4	0.885	0.732
1% coating	1.6	0.876	0.679
2% coating	1.6	0.880	0.640
3% coating	1.7	0.884	0.626
4% coating	1.6	0.885	0.588
ruby crystal clear	4	0.875	0.434

**Table 2. Radiative properties of non-fluorescent reference specimens, including solar reflectances measured without and with a quartz window over the spectrophotometer's reflectance port. Each specimen is 75 mm by 75 mm.**

Code	Description	Coating dry film thickness (μm)	Specimen thickness (mm)	Thermal emittance	AM1GH solar reflectance w/o window	AM1GH solar reflectance w/ window
A1	white	120	1.1	0.888	0.838	0.762
A2	gray #1	108	1.1	0.888	0.733	0.665
A3	gray #2	169	1.2	0.895	0.689	0.615
A4	gray #3	248	1.2	0.886	0.593	0.547
A5	gray #4	214	1.2	0.900	0.494	0.463
A6	gray #5	214	1.2	0.897	0.378	0.366
A7	gray #6	174	1.2	0.905	0.253	0.264
A8	gray #7	217	1.2	0.918	0.123	0.165
A9	black	106	1.1	0.926	0.039	0.102
A10	ruby crystal white		4	0.911	0.769	
A11	ruby crystal gray		4	0.912	0.638	

**Table 3. Conditions and outcomes of Trials in Experiment 5 (i/iii).**

Trial	5A	5B	5C	5D	5E	5F	5G	5H	5I
specimen set	A	A	A	B	B	B	C	C	C
specimen orientation <sup>a</sup>	FS								
date (2016-MM-DD)	09-27	09-28	09-28	09-27	09-28	09-28	09-27	09-27	09-28
measurement start (LDT)	13:43	12:35	15:17	17:34	12:00	16:21	14:36	15:51	13:16
spin-up time (min)	10	10	10	10	10	10	10	10	10
measurement time (min)	15.5	15.5	15.3	15.3	15.6	15.5	15.5	15.4	15.7
measurement revolutions	25	25	25	25	25	25	25	25	25
initial solar elevation (°)	48.8	49.3	38.6	15.3	47.5	28.5	44.2	33.7	49.5
final solar elevation (°)	47.8	49.7	36.4	12.4	48.5	25.8	42.3	31.2	49.0
final beam incidence angle (°)	0	0	0	0	0	0	0	0	0
mean solar irradiance (kW/m <sup>2</sup> )	1.063	1.049	1.067	0.862	1.043	0.984	0.976	0.920	1.069
s.d.	0.009	0.004	0.004	0.019	0.003	0.007	0.145	0.129	0.003
mean wind speed (m/s)	0.16	0.33	0.31	0.00	0.22	0.14	0.11	0.02	0.27
s.d.	0.17	0.22	0.32	0.02	0.15	0.14	0.18	0.06	0.21
mean air temperature (°C)	27.8	19.1	19.5	24.7	19.4	18.4	32.5	32.8	19.5
s.d.	0.49	0.89	0.77	0.35	0.96	0.66	2.94	0.79	0.81
ruby crystal clear ESR							0.762	0.766	0.762
0.2% coating ESR	0.826	0.824	0.829						
1% coating ESR	0.838	0.825	0.792						
2% coating ESR	0.790	0.774	0.761	0.754	0.782	0.755			
3% coating ESR				0.725	0.745	0.721			
4% coating ESR				0.671	0.672	0.663			

<sup>a</sup> FS = facing sun; H = horizontal.

**Table 3 (continued, ii/iii).**

Trial	5J	5K	5L	5M	5N	5O	5P	5Q	5R
specimen set	A	A	A	B	B	B	C	C	C
specimen orientation <sup>a</sup>	H	H	H	H	H	H	H	H	H
date (2016-MM-DD)	09-21	09-24	09-26	09-22	09-26	09-27	09-23	09-26	09-27
measurement start (LDT)	14:16	11:17	12:32	11:59	13:31	11:46	12:38	13:01	12:28
spin-up time (min)	10	10	10	10	10	10	10	10	10
measurement time (min)	33.5	32.7	15.5	32.7	15.5	15.3	33.0	15.4	15.5
measurement revolutions	50	50	25	50	25	25	50	25	25
initial solar elevation (°)	48.6	44.6	50.0	49.4	49.8	46.7	51.3	50.5	49.5
final solar elevation (°)	44.9	48.0	50.4	51.4	49.0	47.9	51.6	50.3	49.9
final beam incidence angle (°)	45.1	42.0	39.6	38.6	41.0	42.1	38.4	39.7	40.1
mean solar irradiance (kW/m <sup>2</sup> )	0.807	0.783	0.861	0.895	0.819	0.906	0.876	0.861	0.895
s.d.	0.040	0.015	0.003	0.008	0.042	0.004	0.003	0.003	0.010
mean wind speed (m/s)	0.33	0.14	0.25	0.36	0.16	0.02	0.36	0.22	0.08
s.d.	0.33	0.19	0.25	0.33	0.22	0.07	0.33	0.25	0.11
mean air temperature (°C)	21.5	24.6	32.7	20.3	33.6	28.3	22.4	33.5	28.6
s.d.	1.21	0.86	0.82	1.16	0.83	0.78	0.99	0.76	0.62
ruby crystal clear ESR							0.792	0.816	0.802
0.2% coating ESR	0.851	0.854	0.861						
1% coating ESR	0.844	0.841	0.838						
2% coating ESR	0.794	0.788	0.793	0.807	0.790	0.784			
3% coating ESR				0.776	0.761	0.747			
4% coating ESR				0.704	0.682	0.683			

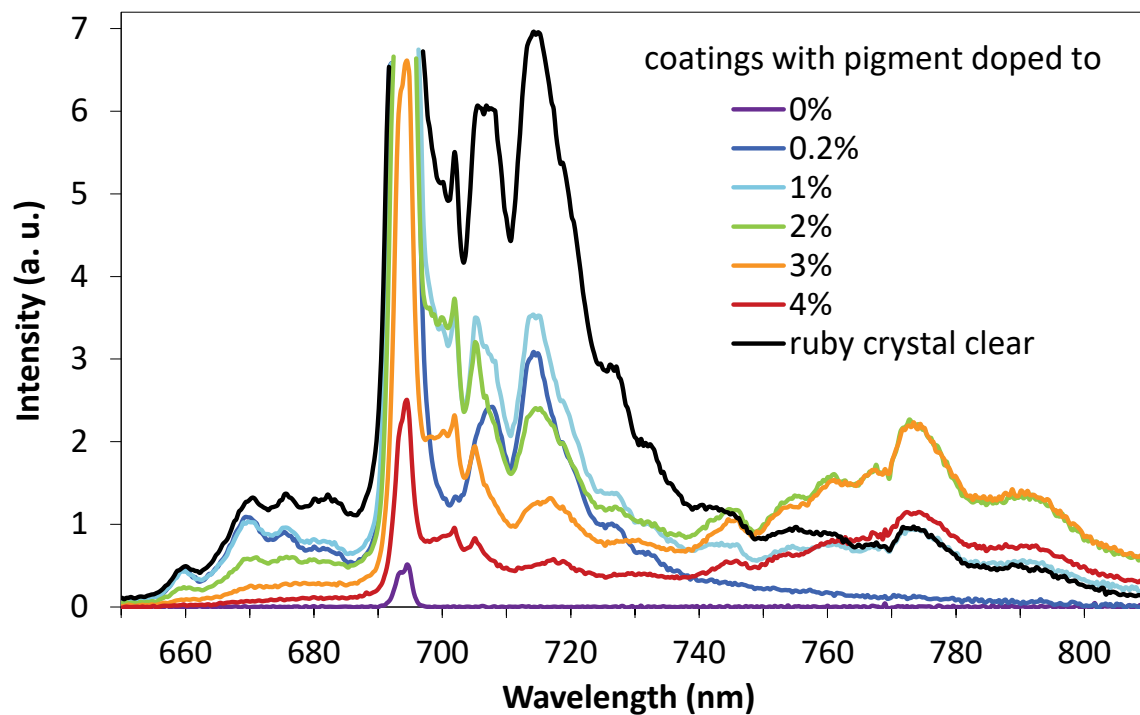
**Table 3 (continued, iii/iii).**

Trial	5S/i	5S/ii	5S/ii i	5S/i v	5S/ v	5S/ vi	5S/ vii	5S/v iii	5S/i x	5S/ x	5T	5U
specimen set	D	D	D	D	D	D	D	D	D	D	E	E
specimen orientation <sup>a</sup>	H	H	H	H	H	H	H	H	H	H	FS	H
date (2016-MM-DD)	09- 29	09- 29	09- 29	09- 29	09- 29	09- 29	09- 29	09- 29	09- 29	09- 29	09- 28	09- 26
measurement start (LDT)	12:3 8	12:5 6	13:1 3	13:3 3	13:5 2	15:1 0	15:3 3	16:1 3	16:3 3	17:0 0	14:1 0	10:5 6
spin-up time (min)	10	1	1	1	1	10	1	10	1	5	10	10
measurement time (min)	15.7	15.7	15.7	15.7	15.8	15.7	15.7	15.7	15.7	16.3	15.4	9.5
measurement revolutions	25	25	25	25	25	25	25	25	25	25	25	15
initial solar elevation (°)	49.1	49.3	49.2	48.6	47.5	39.2	35.9	29.4	26.0	21.1	46.5	41.4
final solar elevation (°)	49.3	49.2	48.7	47.7	46.3	36.9	33.5	26.7	23.2	18.1	45.0	42.6
final beam incidence angle (°)	40.7	40.8	41.3	42.3	43.7	53.1	56.6	63.3	66.8	71.9	0	47.4
mean solar irradiance (kW/m <sup>2</sup> )	0.85	0.85	0.84	0.83	0.81	0.64	0.58	0.53	0.46	0.32	1.04	0.75
s.d.	0	3	8	3	4	9	4	4	8	2	3	9
	0.00	0.00	0.00	0.00	0.00	0.01	0.01	0.01	0.01	0.05	0.00	0.00
	3	3	3	5	6	1	4	4	6	5	3	5
mean wind speed (m/s)	0.20	0.12	0.18	0.13	0.14	0.24	0.17	0.16	0.07	0.16	0.16	0.28
s.d.	0.17	0.15	0.25	0.18	0.18	0.26	0.22	0.17	0.14	0.18	0.18	0.20
mean air temperature (°C)	18.0	18.6	18.6	18.4	18.2	19.4	19.2	19.0	19.7	17.9	20.1	28.8
s.d.	1.16	1.26	1.34	1.21	1.09	1.42	1.04	1.16	0.89	0.84	0.84	0.51
ruby crystal clear ESR	0.82	0.81	0.81	0.81	0.81	0.79	0.79	0.85	0.85	0.91		
0.2% coating ESR	2	5	4	5	3	3	2	6	4	0		
1% coating ESR												
2% coating ESR	0.79	0.78	0.77	0.79	0.79	0.77	0.76	0.77	0.78	0.79		
3% coating ESR	5	8	7	9	7	7	8	7	1	0		
4% coating ESR												

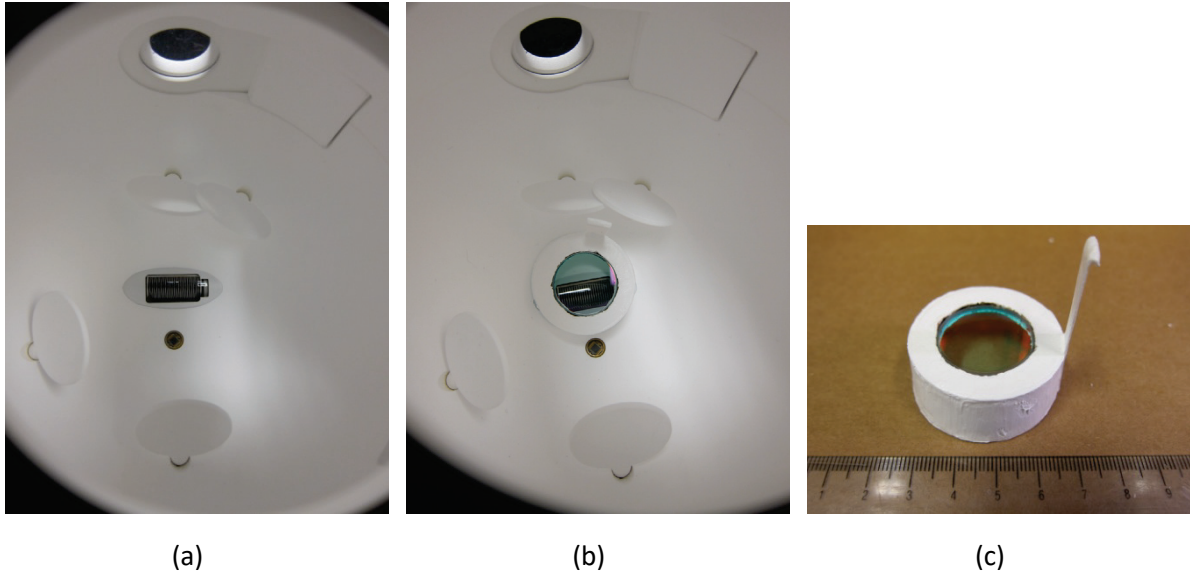
**Table 4. ESRs of fluorescent specimens by measurement orientation, showing sample count, mean, and standard deviation. Horizontal measurements include only those in which the final solar elevation angle was at least 40°. Also shown are pure SR and fluorescence benefit (ESR facing sun – pure SR).**

effective solar reflectance	ESR facing sun			ESR horizontal			ESR horizontal – ESR facing sun	AM1GH pure SR	fluorescence benefit (ESR facing sun – AM1GH pure SR)
	count	mean	s.d.	count	mean	s.d.			
ruby crystal clear	3	0.764	0.002	8	0.811	0.010	0.047	0.434	0.330
0.2% coating	3	0.826	0.002	3	0.855	0.005	0.029	0.732	0.095
1% coating	3	0.818	0.023	3	0.841	0.003	0.023	0.679	0.140
2% coating	6	0.769	0.015	11	0.792	0.008	0.023	0.640	0.130
3% coating	3	0.730	0.013	3	0.761	0.015	0.031	0.626	0.104
4% coating	3	0.669	0.005	3	0.689	0.012	0.021	0.588	0.081

## A. Electronic Supplementary Material



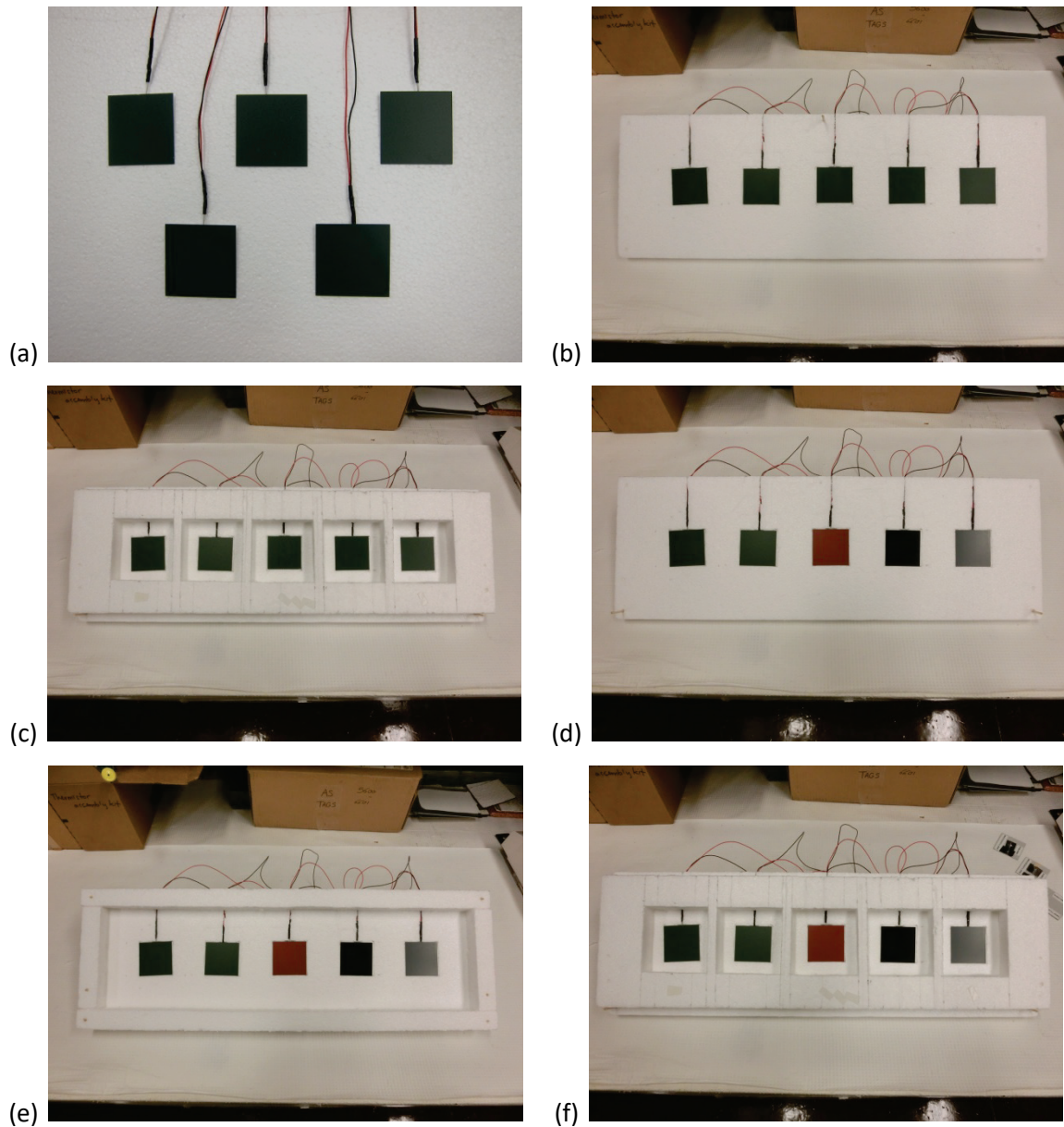
ESM Figure A-1. More detail of the spectra in Figure 5. Note that the nominal 0% pigment must contain a trace of Cr, since a double peak is visible near 694 nm.



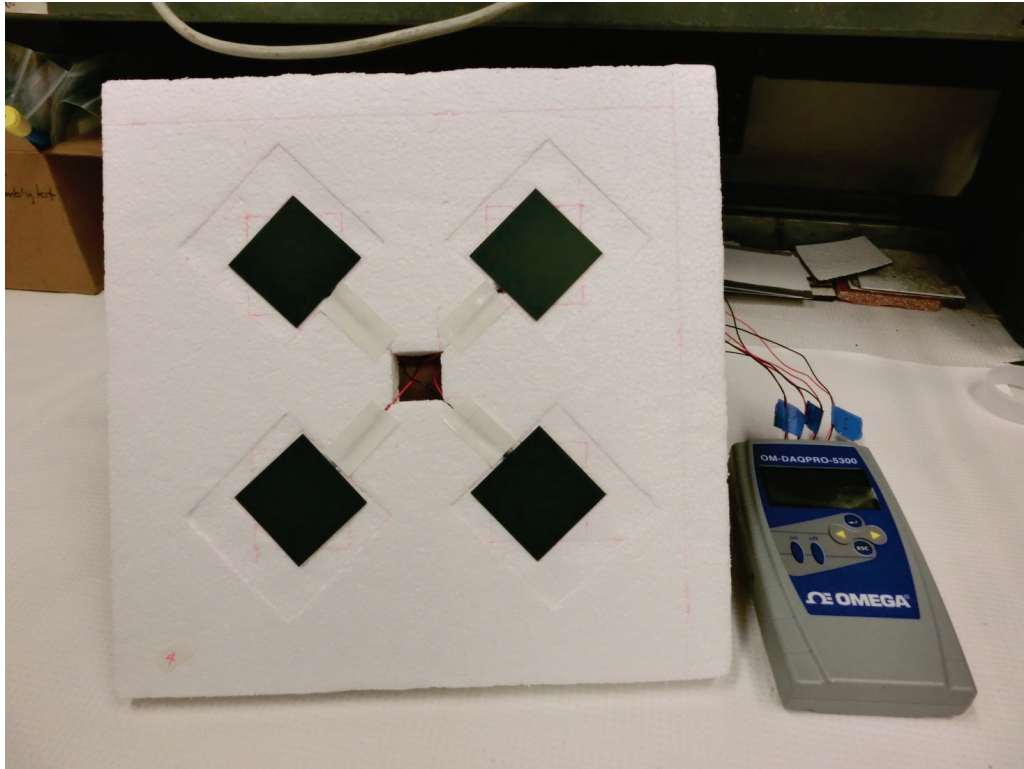
**ESM Figure A-2. Photomultiplier tube sensor (250 – 900 nm) in the integrating sphere of a UV-VIS-NIR spectrophotometer (a) exposed and (b) covered with a removable filter. The filter (c) is mounted in a paper cup that has been painted bright white. It passes 90 to 95% of light from 400 to 650 nm, and reflects nearly 100% of light from 650 to 865 nm.**



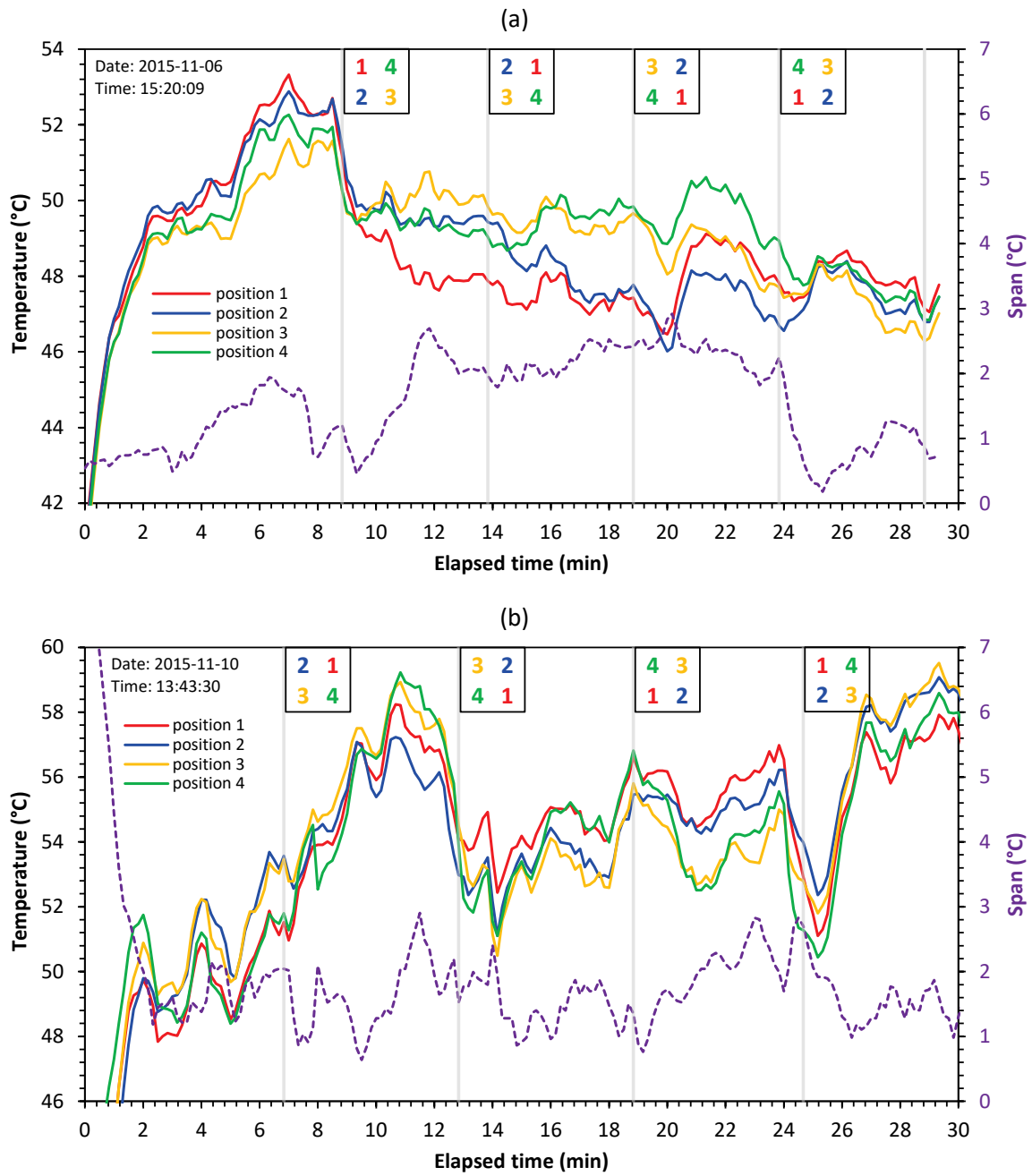
**ESM Figure A-3. Reclining chair with towel used to support specimens in Experiment 0. Note that this photo shows a set of specimens different from that used in Experiment 0.**



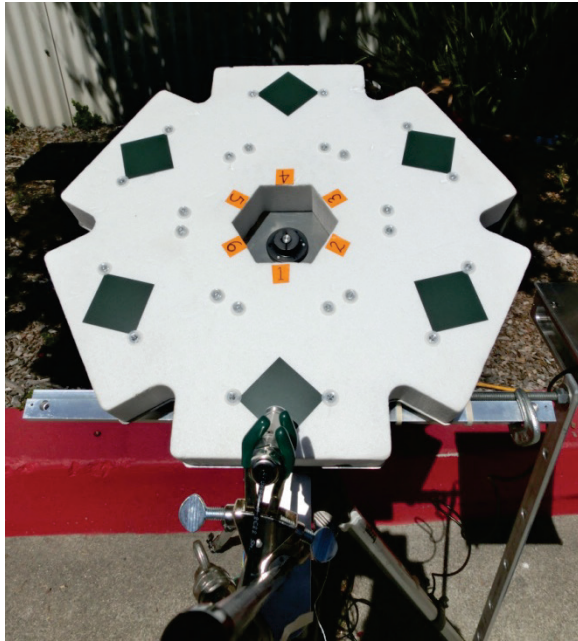
**ESM Figure A-4. Apparata and specimens (50 mm by 50 mm) used in Experiment 2, including (a) Trial 2A, five duplicate specimens arranged in two rows at the center of a 36 cm by 38 cm by 2.5 cm foam board; (b) Trial 2B, the five duplicates arranged in one row on a 20 cm by 61 cm by 2.5 cm foam board; (c) Trial 2C, the five duplicates in a cavity array (9 cm by 9 cm, 25 mm deep); (d) Trial 2D, five different specimens exposed as in 2B; (e) Trial 2E, adding a parapet-style wind break (25 mm height, 5 cm from the specimen row) to the 2D setup; and (f) Trial 2F, five different specimens exposed as in 2C.**



**ESM Figure A-5. Duplicate non-fluorescent specimens on a manually rotated platform with four very shallow cavities. The specimens are arranged in a two by two array on a 33 by 33 by 2.5 cm foam board, with 5 cm spacing. The margin on each side is 6.4 cm.**



**ESM Figure A-6. Surface temperatures and surface temperature range of duplicate non-fluorescent specimens measured on a manually rotated platform, measured in (a) Trial 3A and (b) Trial 3B of Experiment 3.**

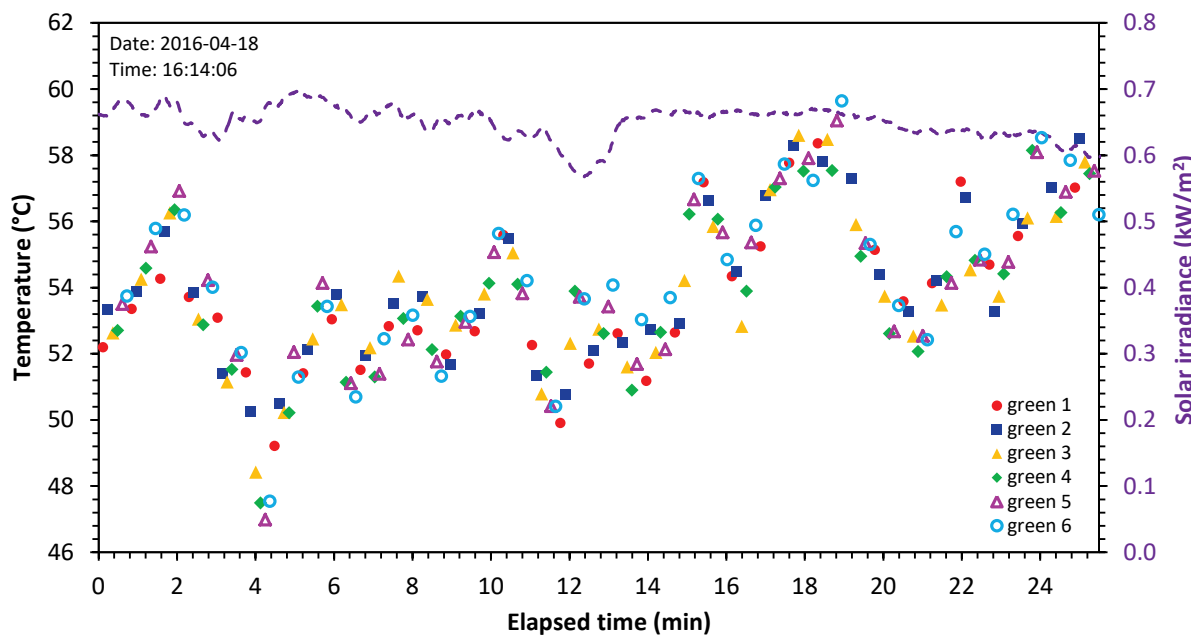


(a)

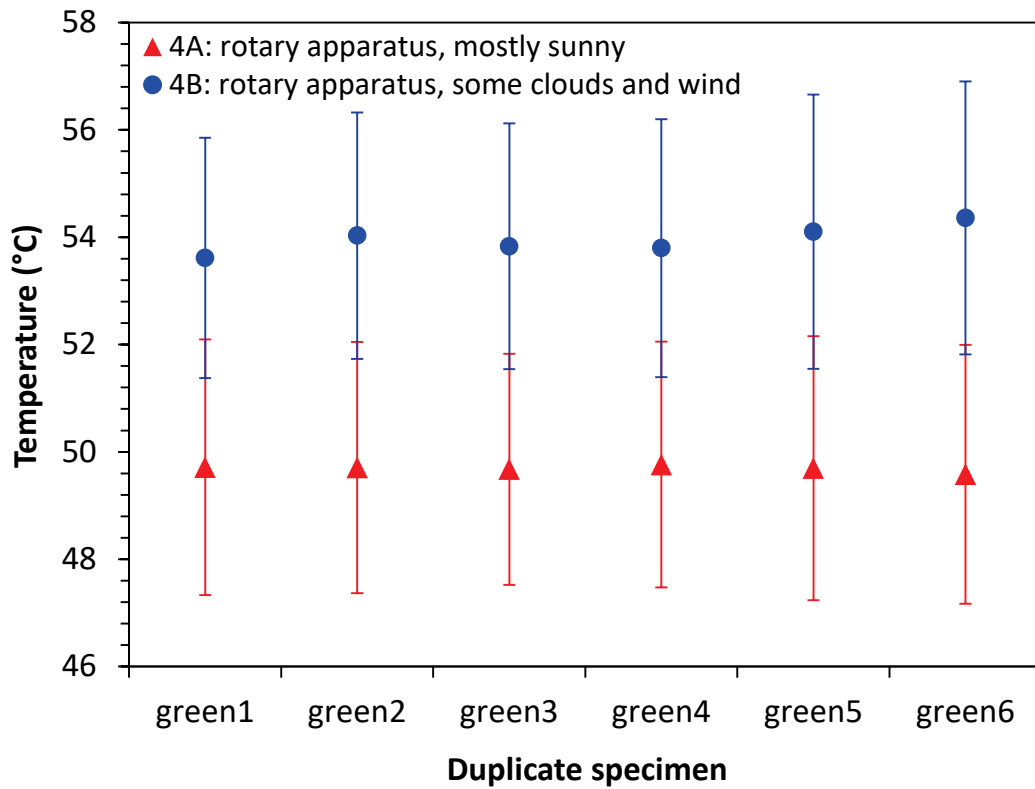


(b)

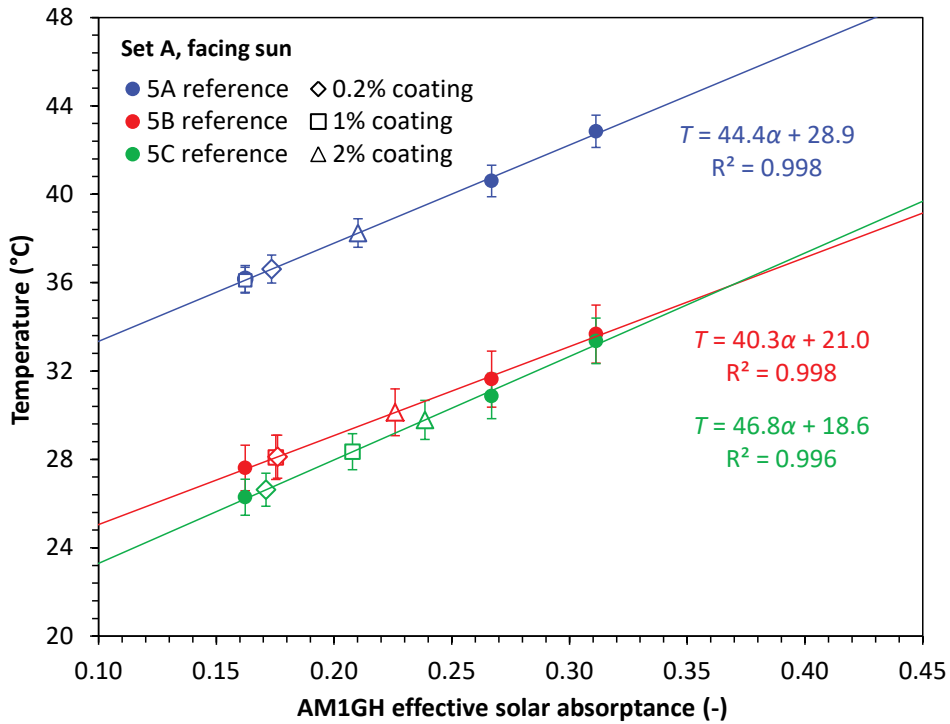
**ESM Figure A-7. Images of the initial programmable rotary apparatus configured for (a) Trials 4A and 4B (six duplicate green specimens) and (b) Trials 4C and 4D (six gray-scale reference specimens). The fixed-position infrared thermometer is shown in foreground.**



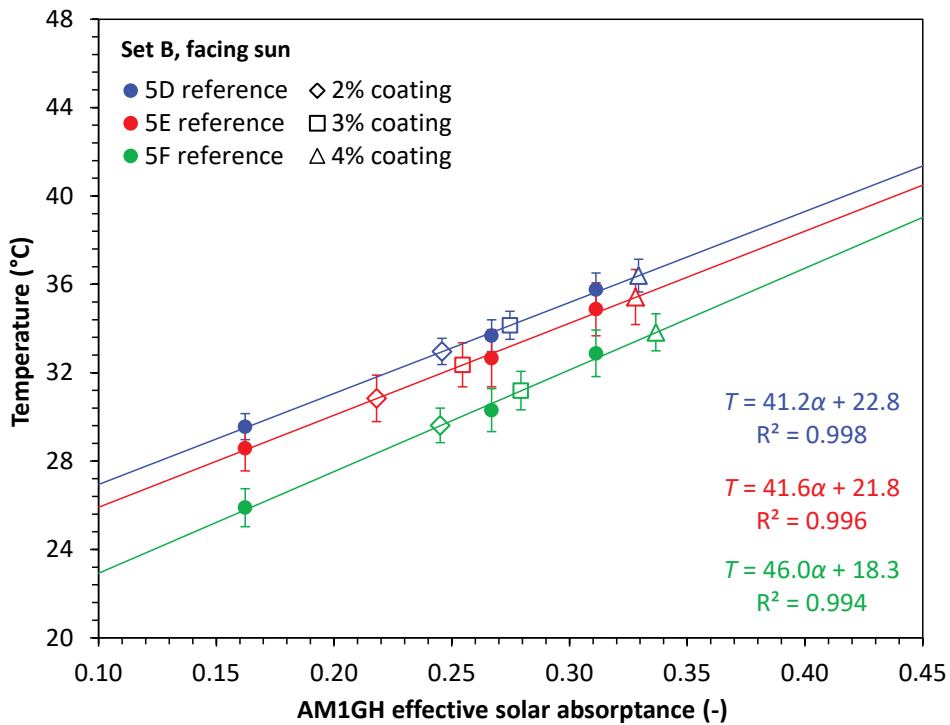
**ESM Figure A-8. Instantaneous surface temperatures of six duplicate green specimens measured with the initial programmable rotary apparatus in Trial 4B. Also shown is global horizontal solar irradiance.**



**ESM Figure A-9. Means and standard deviations of duplicate green specimen temperatures measured with the initial programmable rotary apparatus in Trials 4A and 4B.**

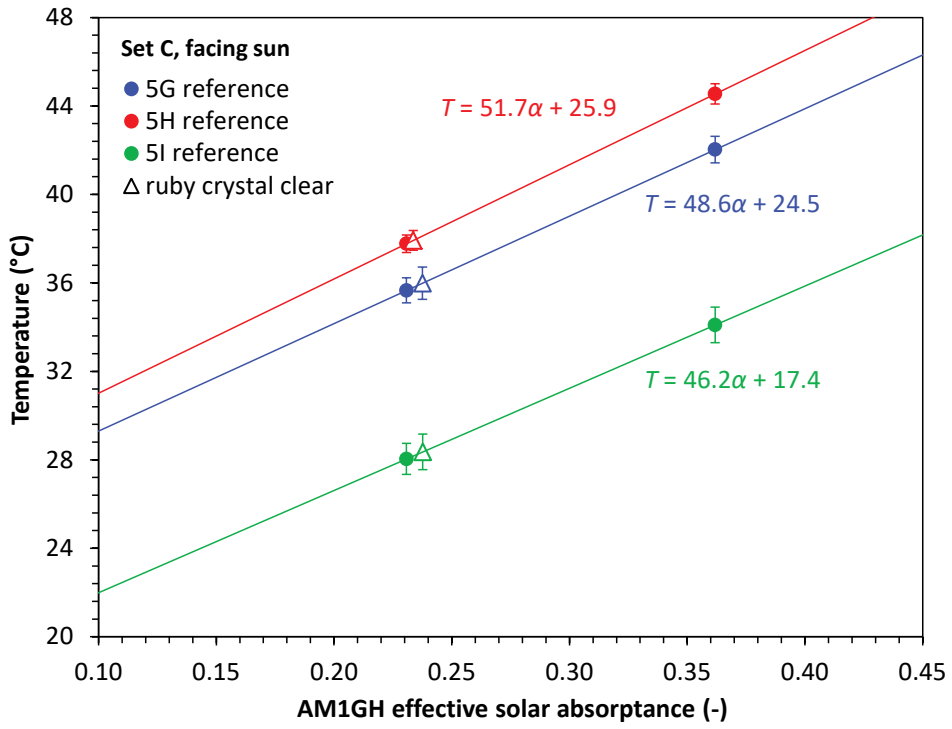


(a)



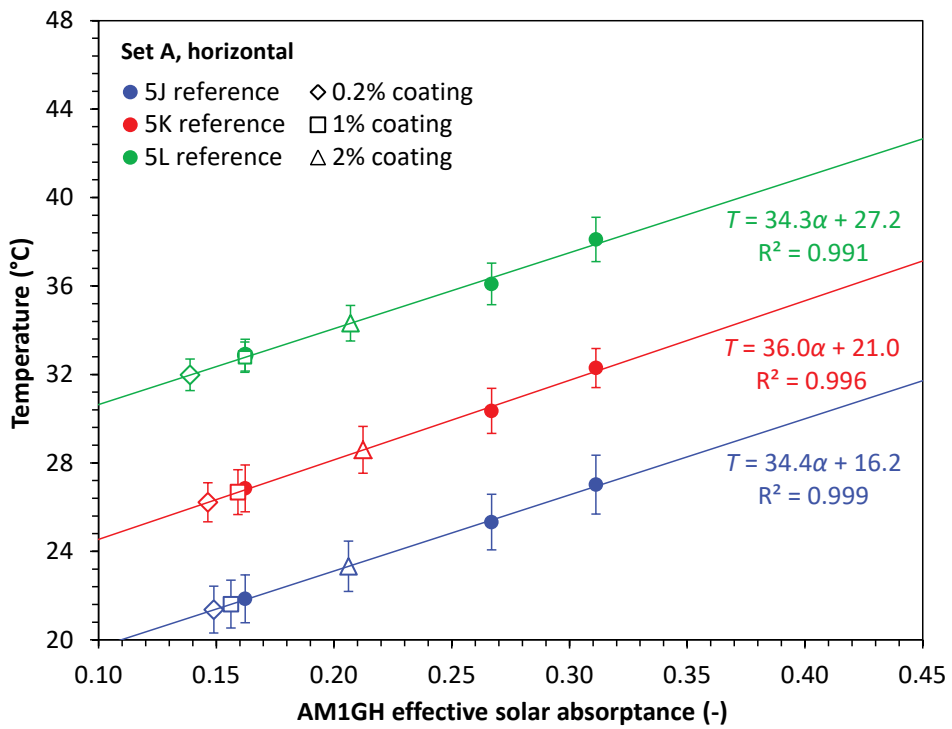
(b)

**ESM Figure A-10. Determination of test specimen ESA from final mean temperatures of test and reference specimens, shown for (a) Trials 5A – 5C (Set A, facing sun); (b) Trials 5D – 5F (Set B, facing sun); (c) Trials 5G – 5I (Set C, facing sun); (d) Trials 5J – 5L (Set A, horizontal); (e) Trials 5M – 5O (Set B, horizontal); and (f) Trials 5P – 5R (Set C, horizontal. Note that Trial 5M used reference A4 (gray#3) in place of reference A3 (gray#2).**



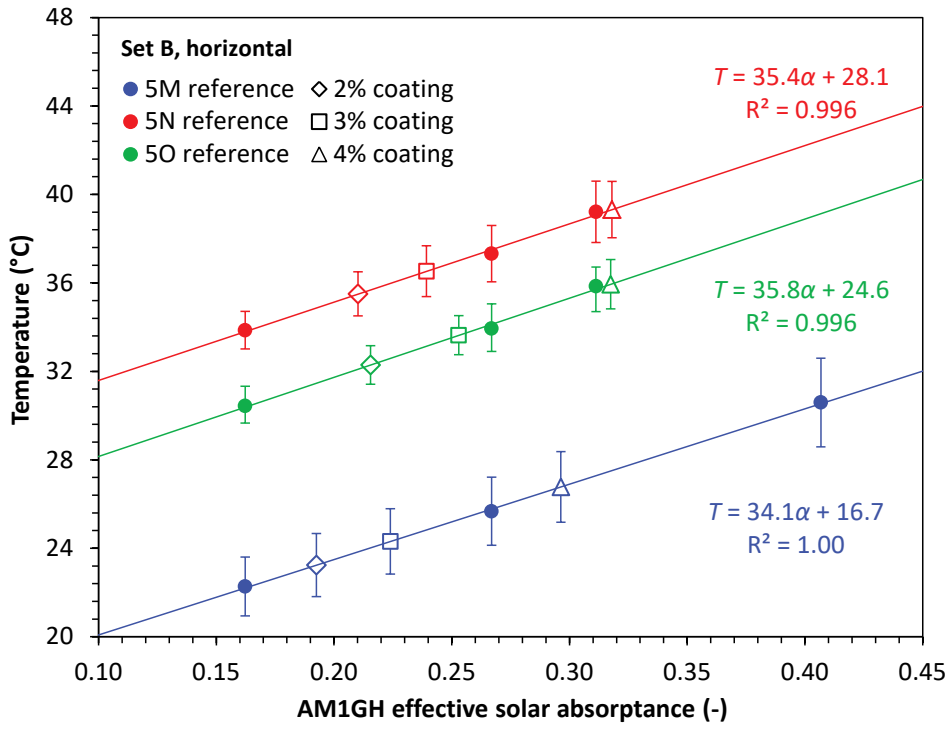
(c)

ESM Figure A-10 (continued)

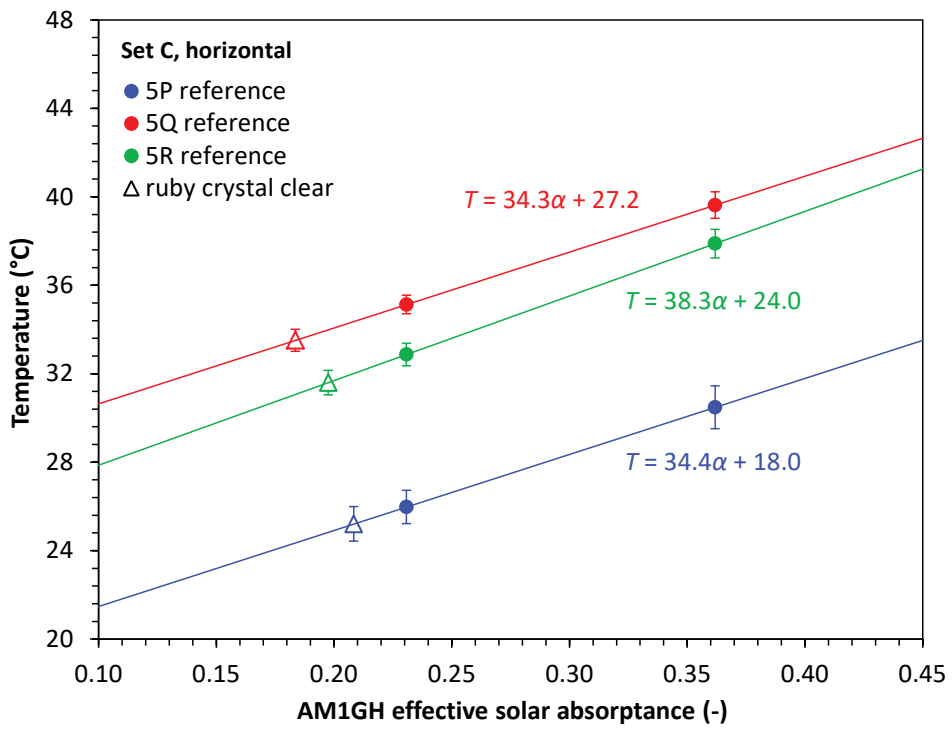


(d)

ESM Figure A-10 (continued)

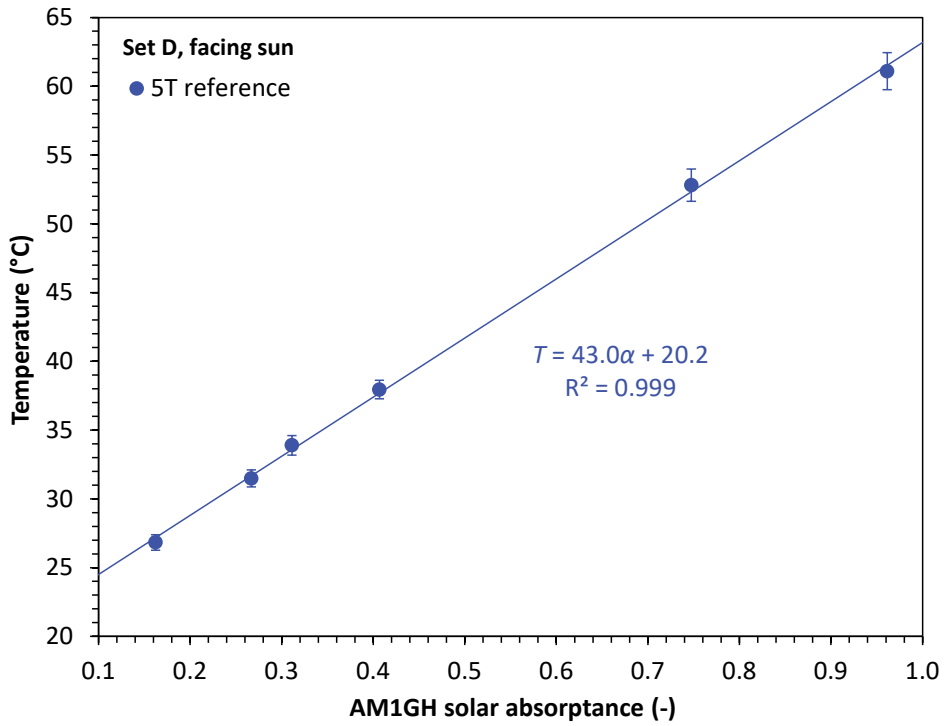


(e)

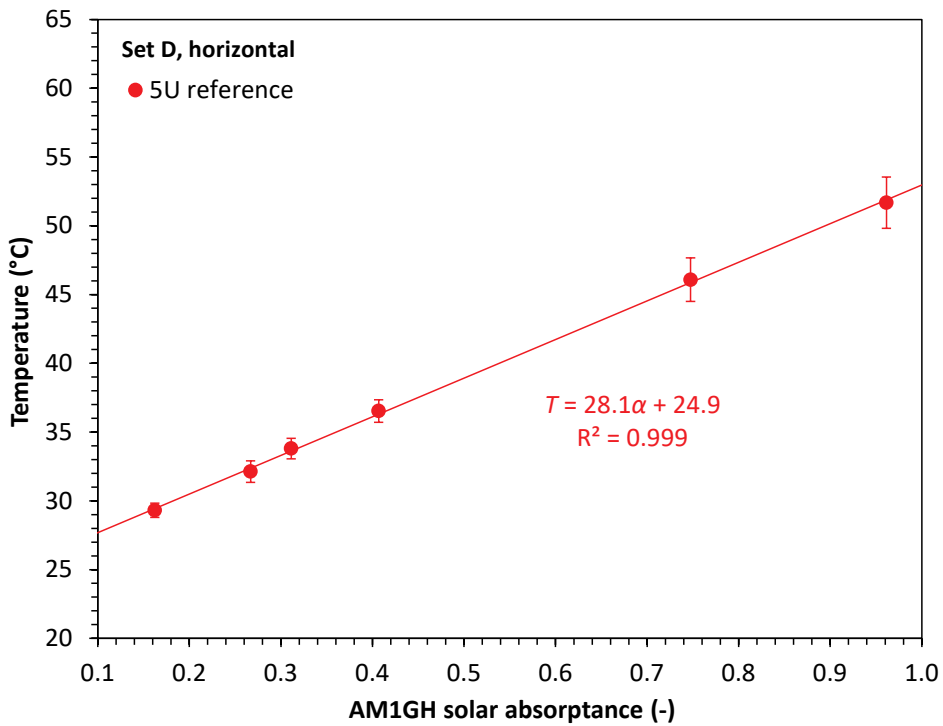


(f)

ESM Figure A-10 (continued)



(a)



(b)

ESM Figure A-11. Final mean temperature versus pure SA for non-fluorescent reference specimens, shown for (a) Trial 5T (Set E, facing sun) and (b) Trial 5U (Set E, horizontal).

**ESM Table A-1. Measurement sensors and protocols used in calorimetric experiments.**

	Experiment 0A	Experiment 0B	Experiment 1	Experiment 2	Experiment 3	Experiment 4	Experiment 5 (final apparatus)
Specimen surface temperature							
Sensor type	Thermistor, NTC 10K ohm	Handheld infrared thermometer	Thermistor, NTC 10K ohm	Thermistor, NTC 10K ohm	Thermistor, NTC 10K ohm	Fixed-mount infrared thermometer	Same as Experiment 4
Sensor make and model	Omega 44006	VWR Traceable Infrared Thermometer (Cat. No. 36934-178)	Omega 44006	US Sensor PR103J2	US Sensor PR103J2	Omega OS151-MT	Same as Experiment 4
Sensor range	-80 to 120 °C	-60 to 500 °C	-80 to 120 °C	-55 to 80 °C	-55 to 80 °C	0 to 250°C	Same as Experiment 4
Sensor accuracy (nominal)	unknown	±(2% + 1 °C) %	unknown	±0.05 °C	±0.05 °C	±1% of reading or ±1°C, whichever is greater	Same as Experiment 4
Sensor repeatability (nominal)	unknown	unknown	unknown	unknown	unknown	±0.5% of reading or ±0.5°C, whichever is greater	Same as Experiment 4
Sensor interchangeability	±0.2 °C (0 to 70 °C)	—	±0.2 °C (0 to 70 °C)	±0.05 °C (0 to 50 °C)	±0.05 °C (0 to 50 °C)	unknown	Same as Experiment 4
Sensor features		adjustable emissivity				15:1 field of view;	Same as Experiment 4

	Experiment 0A	Experiment 0B	Experiment 1	Experiment 2	Experiment 3	Experiment 4	Experiment 5 (final apparatus)
						emissivity fixed at 0.95	
Protocol	Sensors attached to back of specimen with aluminum tape; 9 measurements logged over a period of 11 min	Instrument held briefly above each of 9 specimens; 8 measurement sets performed over a period of 30 min	Sensor attached to back of specimen with thermal paste and aluminum tape; measurements logged every 1 sec over a period of 1-2 hrs	Sensor attached to back of specimen with thermal paste and aluminum tape; measurements logged every 10 sec over a period of 20 min	Sensor attached to back of specimen with thermal paste and aluminum tape; measurements logged every 10 sec over a period of 20 min (3A and 3B) or 6 min (3C)	To reduce shadows, sensor mounted ~3.8 cm from center of specimen, with 55-65° angle between sensor axis and specimen plane; waited 4-5 sec for reading to stabilize	Sensor mounted 2.5 cm (along line of sight) from center of specimen, with 45° angle between sensor axis and specimen plane.
Ambient air temperature							
Sensor type	Old-style bulb thermometer	Same as Experiment 0A	Thermistor, NTC 10K ohm	Same as Experiment 1	Same as Experiment 1	None	Thermistor, NTC 10K ohm
Sensor make and model			Omega 44006	Same as Experiment 1	Same as Experiment 1		US Sensor KS103G2
Sensor range	-30 to 50 °C	Same as Experiment 0A	-80 to 120 °C	Same as Experiment 1	Same as Experiment 1		-80 to 135 °C
Sensor accuracy	± 0.5 °C	Same as Experiment 0A	Unknown	Same as Experiment 1	Same as Experiment 1		see interchangeability
Sensor interchangeability			±0.2 °C (0 to 70 °C)	Same as Experiment 1	Same as Experiment 1		±0.1 °C (0 to 70 °C)

	Experiment 0A	Experiment 0B	Experiment 1	Experiment 2	Experiment 3	Experiment 4	Experiment 5 (final apparatus)
Sensor features							
Protocol	Measurements before and after experiment. Sensor in shade, height 1.5 m	Measurements before, at midpoint, and after experiment. Sensor in shade, height 1.5 m	Sensor installed on the back side of apparatus; measurements logged every 1 sec over a period of 1 to 2 hours	Sensor installed on the back side of apparatus; measurements logged every 10 sec over a period of 20 min	Sensor installed on the back side of apparatus; measurements logged every 10 sec over a period of 20 min (3A and 3B) or 6 min (3C)		Sensor mounted on the underside of the specimen platter, shaded from sunlight.
Solar irradiance							
Sensor type	None	None	Silicon pyranometer	Same as Experiment 1	None	Same as Experiment 1	Same as Experiment 1
Sensor make and model			Kipp & Zonen SP Lite2	Same as Experiment 1		Same as Experiment 1	Same as Experiment 1
Sensor spectral range			400 to 1100 nm	Same as Experiment 1		Same as Experiment 1	Same as Experiment 1
Sensor max irradiance			2000 W/m <sup>2</sup>	Same as Experiment 1		Same as Experiment 1	Same as Experiment 1
Sensor accuracy			Unknown	Same as Experiment 1		Same as Experiment 1	Same as Experiment 1
Protocol			Sensor mounted on the front face of	Sensor placed immediately adjacent to		Sensor placed within 2 m of apparatus, in	Sensor placed on the ground within 1 m of apparatus. Sensor

	Experiment 0A	Experiment 0B	Experiment 1	Experiment 2	Experiment 3	Experiment 4	Experiment 5 (final apparatus)
			apparatus; measurements logged every 1 sec over a period of 1 to 2 hours	apparatus and tilted equivalently; measurements logged every 10 sec over a period of 20 min		horizontal plane	orientation (horizontal or tilted facing the sun) for each trial matched that of the specimens.
Wind speed							
Sensor type	None	None	Handheld vane anemometer	None	None	None	3-cup anemometer
Sensor make and model			PCE Instruments Anemometer PCE-AM 81				Adafruit product 1733
Sensor range			0.4 to 30 m/s				0.5 to 32 m/s
Sensor accuracy			±3% full scale (<20 m/s); ±4% full scale (>20 m/s)				resolution 0.1 m/s; worst-case accuracy 1 m/s
Protocol	Low wind speed required (a cloth on apparatus must not move)	Low wind speed required (a cloth on apparatus must not move)	Sensor placed behind apparatus with propeller oriented for measuring airflow parallel				Sensor placed on the ground within 1 m of apparatus

	Experiment 0A	Experiment 0B	Experiment 1	Experiment 2	Experiment 3	Experiment 4	Experiment 5 (final apparatus)
			to apparatus; recorded maximum wind speed over experiment duration				
Data acquisition system							
Instrument type	Portable handheld data logger	None (measurements recorded manually)	Portable handheld data logger	Portable handheld data logger	Portable handheld data logger	Portable handheld data logger	Multifunction data acquisition device with Python application programming interface
Instrument make and model	Omega OM-DAQPRO-5300		Omega OM-DAQPRO-5300	Omega OM-DAQPRO-5300	Omega OM-DAQPRO-5300	Omega OM-DAQPRO-5300	LabJack T7

**Task Report Appendix B:  
Pre-print of ruby pigment article (Berdahl et al. 2016)**

# **Fluorescent cooling of objects exposed to sunlight – the ruby example**

Paul Berdahl<sup>1\*</sup>, Sharon S. Chen<sup>1</sup>, Hugo Destailats<sup>1</sup>, Thomas W. Kirchstetter<sup>1</sup>,  
Ronnen M. Levinson<sup>1</sup>, and Michael A. Zalich<sup>2</sup>

<sup>1</sup> Heat Island Group, Lawrence Berkeley National Laboratory

<sup>2</sup> PPG Industries, Inc., Coatings Innovation Center, Allison Park, PA 15101, USA

\*Corresponding author, paul.berdahl@gmail.com

## **Abstract**

Particularly in hot climates, various pigments are used to formulate desired non-white colors that stay cooler in the sun than alternatives. These cool pigments provide a high near-infrared (NIR) reflectance in the solar infrared range of 700 to 2500 nm, and also a color specified by a reflectance spectrum in the 400 to 700 nm visible range. Still cooler materials can be formulated by also utilizing the phenomenon of fluorescence (photoluminescence). Ruby,  $\text{Al}_2\text{O}_3:\text{Cr}$ , is a prime example, with efficient emission in the deep red (~694 nm) and near infrared (700-800 nm). A layer of synthetic ruby crystals on a white surface having an attractive red color can remain cooler in the sun than conventional red materials. Ruby particles can also be used as a red/pink pigment. Increasing the Cr:Al ratio produces a stronger (darker) pigment but doping above ~3 wt %  $\text{Cr}_2\text{O}_3$  causes concentration quenching of the fluorescence. The system quantum efficiency for lightly doped ruby-pigmented coatings over white is high,  $0.83 \pm 0.10$ .

## **1. Introduction**

The purpose of this paper is to introduce a novel method for reducing the temperature of (non-white) colored materials exposed to sunlight, by utilizing the phenomenon of fluorescence. In order to illustrate the principle, we use the example of chromium-doped aluminum oxide, i.e., ruby. Of course, it is well known that fluorescent emission transports radiant energy, but its application to reduce the temperature of objects exposed to sunlight is novel.

There are a number of applications in which it is desirable to reject solar heat. These include building envelopes (roofs, walls, etc.) to reduce air conditioning energy use [1-4]. A similar need occurs if materials such as vinyl plastics can be damaged by excessive heat. Automobiles in hot

climates likewise benefit from minimizing solar heating [5]. Further uses are cooling instrumentation enclosures and storage tanks, and cooling ships and military vehicles to reduce their thermal radiation signature [6]. Cool roofing is a key application and a focus of this paper.

In maintaining sunlit objects at low temperatures, high solar reflectance is of course quite beneficial. If some of the solar flux cannot be reflected, then high thermal-infrared emittance and efficient convective cooling are desired. White coatings have suitable solar reflectance and thermal emittance properties, and are appropriate for many applications. On the other hand for aesthetic reasons (or for camouflage) white or other light colors may not be suitable. Building energy codes may require cool roofing. However, manufacturers of roofing materials are then faced with a palette of mostly pastel colors not attractive for their customers. For this reason “cool” colors are needed.

Over the past several decades, cool colored roofing has increased in popularity. For the materials designers, the problem has been to match a desired color (spectral reflectance in the 400 to 700 nm visible range) while maximizing solar reflectance. This has been done mainly by minimizing absorption in the solar near-infrared range (NIR, *ca.* 700 to 2500 nm) [7,8]. Thus non-selective blacks such as carbon black and iron oxide magnetite black are omitted from recipes, and selective blacks such as mixed metal oxides of iron and chromium are used. In the NIR, the selective blacks have lower absorptance and also fairly high reflectance. Durable and cool pigments are available in a variety of colors, mainly based on inorganic mixed oxides containing transition metals. Some organic pigments are also useful and produce vivid colors. However the cost and durability of organics are limitations.

The modern strategy of color combined with high-NIR reflectance is effective but *passive*. Even higher performance is possible by utilizing the *active* phenomenon of fluorescence. Absorbed photons will not only produce heat but also cause fluorescence.

A prototypical fluorescent material is ruby, aluminum oxide doped with chromium. When lightly doped ruby is excited with ultraviolet (UV) or visible light, it fluoresces at 692.9 and 694.3 nm, a doublet called the R-lines [9]. The absorption strength is weak in the red part of the spectrum, and also weak in the blue. Thus the color of ruby varies from pink at low doping to a bluish red as more chromium is added. At high concentrations of chromium (*ca.* 1%), an additional emission spectrum extending from about 655 to beyond 800 nm is particularly apparent [10-13]. The 700-800 nm emission is thought to be due to neighboring pairs and possibly other clusters, of Cr<sup>3+</sup> ions. At higher doping, first the R-lines are extinguished (concentration quenching), and then the additional spectrum also fades away.

Ruby certainly has remarkable optical properties. The first optical laser was fabricated from a lightly doped ruby crystal with silvered end faces, exposed to the light from a flash lamp [9]. Also, the spectral shift of the fluorescent R lines is used to measure pressure [14] and the brightness and decay time can be used to measure temperature [15].

As a first experiment to verify the cooling due to ruby fluorescence, inexpensive commercial synthetic ruby gems were employed. An array of square pyramidal crystals was attached to a bright white substrate (TiO<sub>2</sub> pigmented coating) using a transparent acrylic overcoat. An off-white sample with a calibrated solar reflectance of 0.65 was used for comparison. Both samples were mounted on an insulating substrate and exposed to full sunlight on a clear day. The reference sample's temperature was 21.3 °C above air temperature whereas the ruby-covered sample was only 14.8 °C above air temperature. Therefore the effective solar reflectance (ESR) (corrected for some exposed substrate) was larger than 0.65, and estimated to be about 0.71. (Effective solar reflectance is the fraction of incident solar energy that is rejected by reflectance *and* fluorescence. Additional, more complete, measurements on another ruby-crystal-covered substrate are reported below.) Thus the concept of utilizing chromium-doped alumina to provide reddish colors that are cool in the sun seemed worthy of further investigation.

## 2. Performance of array of synthetic ruby crystals

Polished ruby crystals intended for the jewelry industry were purchased from a commercial supplier. The cost was about 60 USD per lot of 200 crystals. The footprint of each crystal is a 5 mm x 5 mm square with a chamfered pyramidal shape about 2.6 mm high. A 75 mm square aluminum substrate was coated with 3 layers of an acrylic white paint. The crystals were arranged in a square array to cover the substrate and coated with two coats of clear acrylic. The white underlay enhances absorption of excitation light that may pass through the ruby and also reflects fluorescent emission that strikes the substrate. The clear acrylic coating holds the crystals in place and also raises the thermal emittance to 0.89 from 0.71. Figure 1(A) shows the appearance of the crystal array in full sun; the red color is dark, having reflectance in the center of the visual range at 550 nm of only 0.044. The fluorescence is not visible in Fig. 1(A) because the camera (and eye) is not very sensitive at 694 nm and is completely insensitive in the 700 to 800 NIR range. Fig. 1 (B) shows the glow of the array at 694 (and 655 -700) nm when excited by UV in the dark. The fluorescence tends to emerge from the edges of the crystals.

Temperature measurements in full sun were used to estimate the effective solar absorptance of the crystal array and, by subtracting from unity, its effective solar reflectance. Temperature rise in the sun is roughly proportional to solar absorptance. Calibrated non-fluorescent gray and white samples were used for comparison, as was a reference ruby array over-coated with an opaque white paint. The white array was used to check that convective cooling was not unduly enhanced by surface roughness. A first estimate, made by interpolating between calibrated gray and white samples, yielded an effective absorptance of 0.262. A second estimate used the white-coated ruby crystal array as a reference, and employed estimates of the solar flux (1050 W m<sup>-2</sup>) and of the longwave radiative cooling of a blackbody emitter, referred to ambient air temperature (70 W m<sup>-2</sup>), to infer the sum of the radiative and convective heat transfer coefficients of  $h_r + h_c = 14.7 \text{ W m}^{-2} \text{ K}^{-1}$ . These coefficients were then used to compute the effective solar absorptance of the ruby crystal array as 0.264. Averaging the two estimates of

absorptance and subtracting from unity yields  $ESR = 0.737 \pm 0.010$ . Spectrometer measurement, excluding the fluorescence, yields solar reflectance  $SR = 0.434$ . Thus the fluorescence contribution (“boost”), the difference  $ESR-SR$ , is about 0.30; the fluorescent energy flux is over  $300 \text{ W m}^{-2}$ . The ruby array is as cool in the sun as typical white commercial materials with  $SR$  in the range of  $[0.65, 0.85]$ , but is quite visually dark.

### 3. Combustion synthesis of ruby powder

The combustion synthesis method of Kingsley and Patil [16] was chosen as a convenient method for synthesizing small quantities of ruby powder with various chromium concentrations. Briefly, hydrated nitrates of aluminum and chromium are dissolved in water, as is sufficient urea (fuel) for a combustion reaction. A glass beaker containing the solution is placed in a  $500 \text{ }^\circ\text{C}$  furnace. After boiling for several minutes, the dehydrated solution ignites for several seconds. What remains in the beaker is a fluffy pink product consisting of  $\text{Al}_2\text{O}_3:\text{Cr}$ . The yield is  $\sim 95\%$  crystalline  $\alpha$ -phase alumina with  $\gamma$ -phase alumina as a second phase. The Cr doped  $\gamma$  phase is easily identified as its color is not pink. Depending on the Cr concentration, this phase is green, yellow or white [17]. The unwanted  $\gamma$  phase was physically removed, although we also verified that annealing it at  $1200 \text{ }^\circ\text{C}$  for two hours in air can convert it to the  $\alpha$  phase.

In preparing various ruby powders, we found that some excess fuel improved preparation of larger lots. Further, higher furnace temperatures were beneficial for higher Cr doping. The combustion process is more rapid at higher furnace temperatures, though if it is too fast the product is dispersed inside the furnace.

X-ray fluorescence (XRF) verified the expected chromium concentration for two of the samples (1%, 3%). (In this paper, we express the doping by means of  $w$ , the weight fraction of  $\text{Cr}_2\text{O}_3$  in  $\text{Al}_2\text{O}_3$ . A common alternative is to use  $x$ , the ratio of numbers of Cr to Al atoms;  $x = 0.67 w$ .) BET-measured surface area varied considerably from run to run, with typical values of  $1 \text{ m}^2\text{g}^{-1}$ , ranging up to  $11 \text{ m}^2\text{g}^{-1}$  with higher furnace temperatures. Electron micrographs (Fig. 2) show slab-like particles with typical thickness of 2 to  $5 \text{ }\mu\text{m}$ . The morphology is likely a replica of the walls of foam just prior to combustion. After each synthesis a small UV lamp was used to visually check for the expected red fluorescence. X-ray diffraction also was used to verify that the observed peaks are those of the  $\alpha$  phase of alumina.

To measure optical properties, the powders were mixed with a transparent acrylic paint using a spatula on a smooth glass surface, and spread as a  $\sim 500 \text{ }\mu\text{m}$  coating onto a white substrate (75 mm square of aluminum with three coats of an artists’ titanium dioxide white). This process is crude but simple. About 3 g of pigment was used in each coating. In what follows, the coatings are identified by the weight fraction of chromium oxide in the alumina pigment: 0.0%, 0.2%, 1%, 2%, 3%, and 4%.

## 4. Spectral fluorescence and Effective Solar Reflectance (ESR)

The optical setup included a 6 V lamp (tungsten filament, xenon gas fill), a filter to block excitation light in the spectral range of emission, a 150 mm integrating sphere, and an Ocean Optics spectrometer with silicon array detector. The spectrometer was calibrated using the tungsten lamp filament as a reference at an assumed temperature of 3000 K.

Figure 3 shows the spectral emission of the ruby-pigmented coatings and the crystal array. Comparable data for two ruby crystals may be found in [12]. The sharp peak at 694 nm is highest in the low concentration samples (0.2%, 1%) and diminishes monotonically with higher doping. Particularly at higher doping, emission ranges all the way from 655 to ~800 nm.

ESR measurements were performed on each of the 75 mm square samples by placing them on a thermally insulating substrate in full sunlight, next to calibrated non-fluorescent white and light gray samples of known solar reflectance (SR). Thermistors underneath the samples determined the temperatures, and the ESR values were then determined by interpolation. For comparison, the regular SR was determined with a Perkin Elmer Lambda 900 spectrometer fitted with a 150 mm integrating sphere. A standard solar spectrum for clear sky conditions with the sun high in the sky was used as a weighting function [18]. The short-wave part of the spectrum was detected with a photomultiplier tube (out to ~ 860 nm), and the long-wave part was detected with a PbS semiconductor detector. Now, the ruby fluorescence interferes slightly with the reflectance measurement since, for example, when the sample is illuminated with blue light it reflects blue light but also glows with red and near-infrared light detected by the phototube. For this reason, we used an interference filter placed over the phototube to greatly reduce its sensitivity to red and near infrared light. This filter allowed us to measure the reflectance spectrum excluding the fluorescence. Measurements without the filter then allowed us to evaluate the reflectance correction needed to account for fluorescence. This correction had the spectral shape of the well-known ruby excitation spectrum [9] and was largest at 0.081 at 560 nm for the 1% sample. The ESR results for the ruby pigmented coatings are shown in Fig. 4, along with SR measurements and reflectance at 550 nm. These coatings are not as dark as the ruby crystal array but nonetheless exhibit a fluorescence contribution (ESR-SR) of up to 0.16.

## 5. Determination of quantum efficiency

It is assumed that all of the photons not reflected in the UV and the 400 to 700 nm visible range are absorbed by  $\text{Cr}^{3+}$  ions. This approximation is based on the idea that other weak absorption centers present, for example in the undoped  $\text{Al}_2\text{O}_3$  sample, are not able to successfully compete for photons with the chromium ions. Particularly in the 650 to 700 nm

range the  $\text{Cr}^{3+}$  absorption may be slightly overestimated. Beyond 700 nm, there is still some absorption but it is relatively weak and will be neglected (Fig. 5).

The reflectance spectra in Fig. 5 show the two sharp absorption dips corresponding to the main ruby emission lines, and also some features at longer wavelength. This structure is a consequence of time reversal invariance, in that photon emission processes can proceed in reverse, causing absorption. Also, it is interesting that the baselines in this figure are lower with higher doping. We do not understand the reasons for this absorption but note that a similar phenomenon has been observed in a multiple scattering environment by another group [19].

The number of fluoresced photons can be estimated based on the energy content in the ESR-SR fluorescent contribution and the wavelength distribution in Fig. 4. Division by the number of photons absorbed then yields the quantum efficiency data shown in Table 1. The typical  $\text{Cr}_2\text{O}_3$  content of the ruby crystals was determined by X-ray fluorescence to be 0.9%; analysis of the very lightest and darkest crystals showed a range of 0.6% to 1.8%.

**Table 1. Performance of eight samples. Visual reflectance, ESR, ESR-SR, energy efficiency, and quantum efficiency.**

Sample	Cr <sub>2</sub> O <sub>3</sub> content (wt % in Al <sub>2</sub> O <sub>3</sub> )	Reflectance at 550 nm	Effective Solar Reflectance (ESR)	Fluorescence Contribution, (ESR-SR)	Energy efficiency	Quantum efficiency
Crystal array 1	~ 0.9	0.04	0.706	0.293	0.70	0.95
Crystal array 2	~ 0.9	0.044	0.737	0.303	0.72	0.98
Coating	0.0	0.923	0.828	0.00	0	0
Coating	0.2	0.540	0.824	0.092	0.56	0.93
Coating	1	0.366	0.807	0.128	0.55	0.74
Coating	2	0.301	0.805	0.165	0.62	0.83
Coating	3	0.261	0.780	0.154	0.56	0.74
Coating	4	0.203	0.637	0.049	0.16	0.21

The white substrate has a reflectance of about 0.933 at 700 nm. Since half of the photons are emitted toward the substrate, the highest possible system quantum efficiency is about 0.97. Thus the crystal arrays have very high quantum efficiencies, and the films pigmented with ruby are in the range of  $0.83 \pm 0.10$  for doping  $\leq 3\%$ . The relatively large uncertainty in the quantum efficiency is believed to reflect experimental errors in ESR of roughly 0.01. By 4%, the quantum efficiency decreases dramatically to 0.21.

## 6. Limitations of ruby powder as a red pigment

We have shown that doping above 3% of Cr<sub>2</sub>O<sub>3</sub> leads to much reduced fluorescence. If we elect to use 3% or less dopant, the absorption strength of the pigment is limited. The average optical absorption cross section of the Cr<sup>3+</sup> ion in the portion of the solar spectrum absorbed by ruby is roughly  $1 \times 10^{19} \text{ cm}^2$  [9]. The concentration of ions at 3% is  $\sim 6 \times 10^{20} \text{ cm}^3$ . For the product of these numbers and the layer thickness  $d$  to be unity,  $d \sim 160 \mu\text{m}$ . Now some commercial coatings (paints) are as thin as  $20 \mu\text{m}$ , so it is clear that the ruby pigments are “weak.” In commercial coatings applications, maximum pigment volume concentrations are on the order of 50 %, which would require twice the film thickness. On the other hand, efficient use of the fluorescence requires a reflective underlayer, which halves the needed thickness. Further, introduction of some scattering may enhance absorption efficiency at the expense of a lighter color. However, the main point is that the limited pigment tinting strength is an issue in applications in which film thickness is constrained.

The color of the coatings studied here range from light red to pink, in contrast to the darker array of ruby crystals. The reason is light scattering due to the difference in ruby refractive index ( $\sim 1.76$ ) and that of the polymer medium ( $\sim 1.5$ ). Reduction of light scattering can be obtained by using larger particles, with fewer interfaces per unit volume, or by using nanoparticles with diameters well below 100 nm. Also, the medium can possibly be engineered to have a high and matching refractive index (scattering is proportional to the square of the difference in refractive indices).

Finally, we point out that aluminum oxide particles are hard and abrasive, so care is required to avoid damage to coating manufacturing equipment.

## 7. Fluorescent pigments other than ruby

While the fluorescence of ruby is remarkable, with high quantum efficiency, our example is not unique. Other solid-state laser materials like Nd-doped YAG (yttrium aluminum garnet) are obvious possibilities. The study of IR fluorescence in historical pigments [20] has shown that the cadmium pigments CdS, CdSe and their alloys fluoresce [21], as do some alkali earth copper silicates [22, 23] such as Egyptian blue ( $\text{CaCuSi}_4\text{O}_{10}$ ) and Han blue ( $\text{BaCuSi}_4\text{O}_{10}$ ). Decades of research on phosphors for color television, for mercury-vapor fluorescent lamps, and more recently for light emitting diodes, has led to a wide variety of efficient compounds that fluoresce in the visible [24, 25]. Doubtless some of these compounds can be modified for emission in the near infrared. Further candidate materials for NIR fluorescence may be found in sister applications. These include pigments for labeling, including nanoparticles for biological applications, direct-bandgap semiconductors considered for photovoltaics, and chromophores for application in fluorescent solar concentrators [26, 27].

For applications to cooling of sunlit materials, beyond fluorescence, we need interesting color, compatibility with high NIR reflectance, durability, and minimal toxicity.

## 8. Summary

In summary, we have introduced the idea of utilizing fluorescence to reduce the temperature of objects in sunlight, using ruby as an example. We have also used temperature measurements in sunlight, together with spectral measurements of reflectance and fluorescence, to determine the quantum efficiency of the fluorescence process.

## Acknowledgments

M. L. Shiao pointed out to P. B. that innovation in cool roofing materials is needed. Colleagues at Shepherd Color (S. Boocock, J. Peake) advised us on solid-state synthesis of mixed metal oxide pigments. We thank M. Levitus of Arizona State University for assistance with early fluorescence measurements, X. Song of the LBNL electrochemistry group for assistance with

BET measurements, N. Bronstein of University of California at Berkeley for bringing Refs. 26 and 27 to our attention, and D. McHenry of PPG Industries for XRF measurements. This work was supported by the Assistant Secretary for Energy Efficiency and Renewable Energy, Building Technologies Office of the US Department of Energy under Contract No. [DE-AC02-05CH11231](#). Additional support was provided by the California Energy Commission under Agreement EPC-14-010.

## References

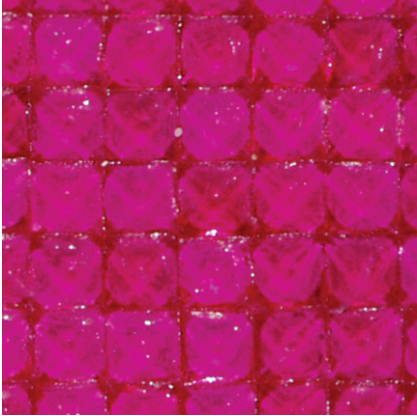
1. J. A. Reagan and D. M. Acklam, Solar reflectivity of common building materials and its influence on the roof heat gain of typical southwestern USA residences, *Energy & Buildings* **2**, 237-248 (1979).
2. A. H. Rosenfeld, H. Akbari, J. J. Romm, and M. Pomerantz, Cool communities: strategies for heat island mitigation and smog reduction, *Energy & Buildings* **28**, 51-62 (1998).
3. M. Pomerantz, H. Akbari, P. Berdahl, S. J. Konopacki, H. Taha, and A. H. Rosenfeld, [Reflective surfaces for cooler buildings and cities](#), *Philosophical Magazine Part B* **79**, 1457-1476 (1999).
4. H. Akbari, R. Levinson, L. Rainer, Monitoring the energy-use effects of cool roofs on California commercial buildings, *Energy & Buildings* **37**, 1007-1016 (2005).
5. R. Levinson, H. Pan, G. Ban-Weiss, P. Rosado, R. Paolini, and H. Akbari, Potential benefits of solar reflective car shells: cooler cabins, fuel savings and emission reductions, *Applied Energy* **88**, 4343-4357 (2011).
6. R. F. Brady and L. V. Wake, Principles and formulations for organic coatings with tailored infrared properties, *Prog. in Organic Coatings* **20**, 1-25 (1992).
7. R. Levinson, P. Berdahl, H. Akbari, W. Miller, I. Joedicke, J. Reilly, Y. Suzuki, and M. Vondran, Methods of creating solar-reflective nonwhite surfaces and their applications to residential roofing materials, *Solar Energy Materials and Solar Cells* **91**, 304-314 (2007).
8. R. Levinson, P. Berdahl, and H. Akbari, Solar spectral optical properties of pigments, Parts I and II, *Solar Energy Materials and Solar Cells* **89**, 319-349 and 351-389 (2005).
9. T. H. Maiman, R. H. Hoskins, I. J. D'Haenens, C. K. Asawa, and V. Evtuhov, Stimulated optical emission in fluorescent solids. II. Spectroscopy and stimulated emission in ruby, *Phys. Rev.* **123**, 1151-1157 (1961).
10. N. A. Tolstoi, Liu Shun'-fu, and M. E. Lapidus, The luminescence kinetics of chromium luminophors. III. Ruby, *Optics & Spectroscopy* **13**, #2, 133-136 (1962).

11. A. L. Schawlow, D. L. Wood, and A. M. Clogston, Electronic spectra of exchange-coupled ion pairs in crystals, *Phys. Rev. Lett.* **3**, 271-273 (1959).
12. R. C. Powell, B. DiBartolo, B. Birang and C. S. Naiman, Fluorescence studies of energy transfer between single and pair Cr<sup>3+</sup> systems in Al<sub>2</sub>O<sub>3</sub>, *Phys. Rev.* **155**, 299-308 (1967).
13. R. C. Powell and B. DiBartolo, Optical properties of heavily doped ruby, *Phys. Stat. Sol. (a)* **10**, 315-357 (1972).
14. J. D. Barnett, S. Block, and G. J. Piermarini, An optical fluorescence system for quantitative pressure measurement in the diamond-anvil cell, *Rev. Sci. Instruments* **44**, 1-9 (1973).
15. C. Pflitsch, R. A. Siddiqui, and B. Atakan, Phosphorescence properties of sol-gel derived ruby measured as functions of temperature and Cr<sup>3+</sup> content, *Appl. Phys. A* **90**, 527-532 (2008).
16. J. J. Kingsley and K. C. Patil, A novel combustion process for the synthesis of fine particle  $\alpha$ -alumina and related oxide materials, *Materials Letters* **6**, 427-432 (1988).
17. S. Cava, R. Beninca, S. M. Tebcherani, I. A. Souza, C. A. Paskocimas, E. Longo, and J. A. Varela, Structural and spectroscopic characterization of Al<sub>2-x</sub>Cr<sub>x</sub>O<sub>3</sub> powders obtained by polymeric precursor method, *J. Sol-Gel Sci. Techn.* **43**, 131-136 (2007).
18. R. Levinson, H. Akbari, P. Berdahl, Measuring solar reflectance - part I: defining a metric that accurately predicts solar heat gain, *Solar Energy* **84**, 1717-1744 (2010).
19. C. Wang and Z Zhao, Transparent polycrystalline ruby ceramic by spark plasma sintering, *Materials Research Bulletin* **45**, 1127-1131 (2010).
20. A. Romani, C. Clementi, C. Miliani, and G. Favaro, Fluorescence spectroscopy: a powerful technique for noninvasive characterization of artwork, *Accounts of Chemical Research* **43**, 837-846 (2010).
21. M. Thoury, J. K. Delaney, E. Rene de la Rie, M. Palmer, K. Morales, and J. Krueger, Near-infrared luminescence of cadmium pigments: in situ identification and mapping in paintings, *Appl. Spectroscopy* **65**, 939-951 (2011).
22. G. Pozza, D. Ajo, G. Chiari, F. De Zuane, and M. Favaro, Photoluminescence of the inorganic pigments, Egyptian Blue, Han blue, and Han purple, *J. of Cultural Heritage* **1**, 393-398 (2000).
23. G. Accorsi, G. Verri, M. Bolognesi, N. Armaroli, C. Clementi, and Aldo Romani, The exceptional near-infrared luminescence properties of cuprorivaite (Egyptian blue), *Chem. Commun.* 3392-3394 (2009).
24. W. M. Yen and M. J Weber, *Inorganic phosphors: compositions, preparation, and optical properties*, CRC Press, Boca Raton, Florida 33487 USA (2004)

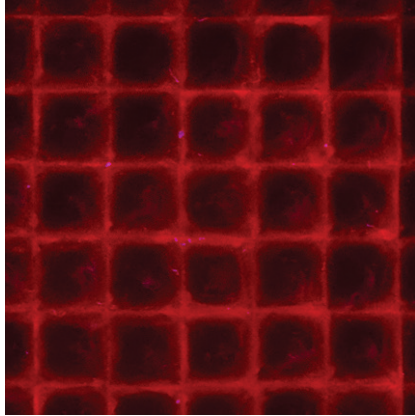
25. W. M. Yen, S. Shionoya, and H. Yamamoto, eds., *Fundamentals of phosphors*, CRC Press, Taylor and Francis Group, Boca Raton, Florida 33487 USA (2007).

26. P. S. Friedman and C. R. Parent, Luminescent solar concentrator development, project report SERI/STR-211-3149 for the Solar Energy Research Institute (1987).

27. M. G. Devije and P. P. C. Verbunt, Thirty years of luminescent solar concentrator research: solar energy for the built environment, *Adv. Energy Mater.* **2**, 12-35 (2012).



(A)



(B)

Fig. 1. Photographs of a portion of the ruby crystal array (A) in sunlight (B) when illuminated by ultraviolet radiation in the dark.

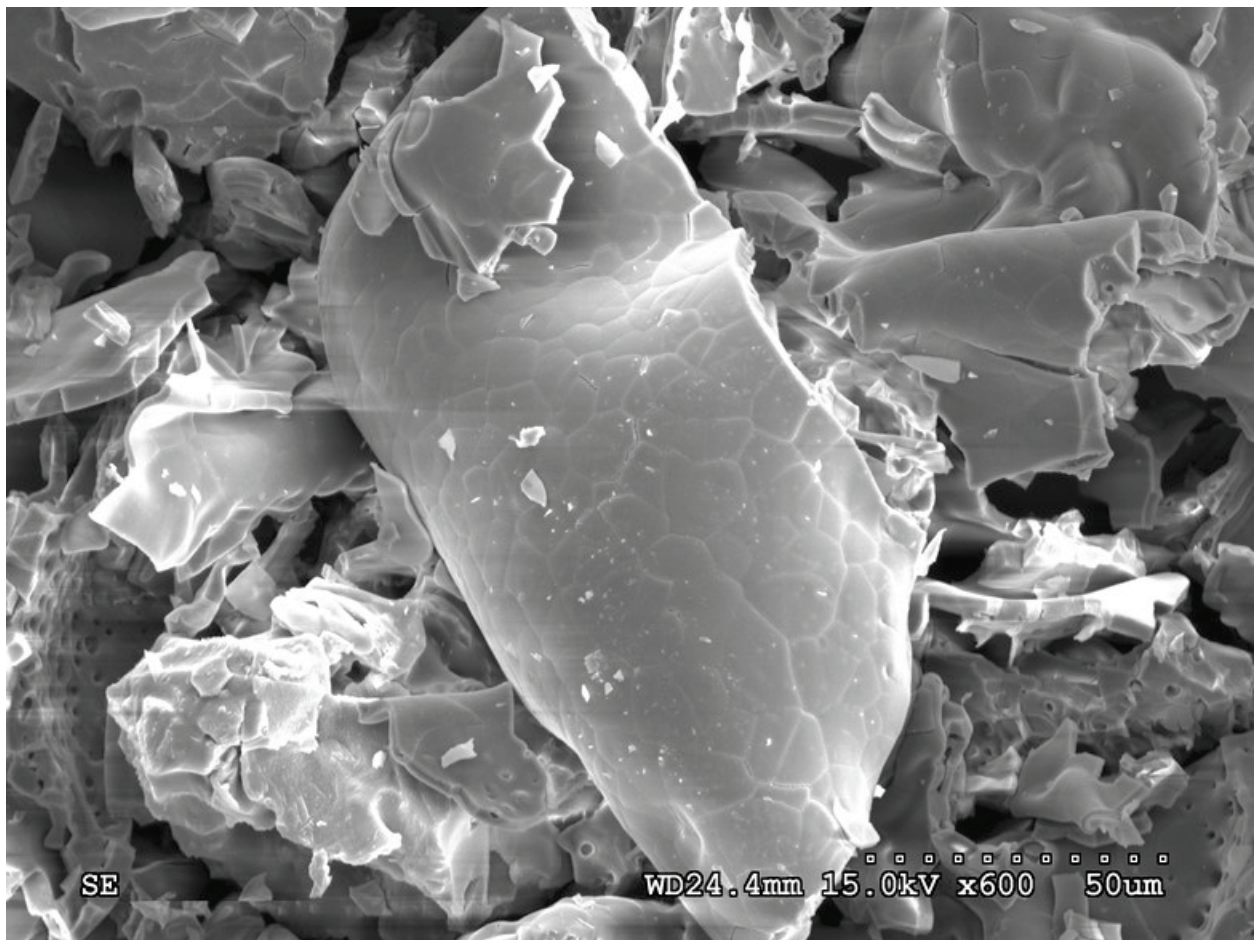


Fig. 2. (A) Low-resolution scanning electron micrograph of  $\text{Al}_2\text{O}_3\text{:Cr}$  combustion product.

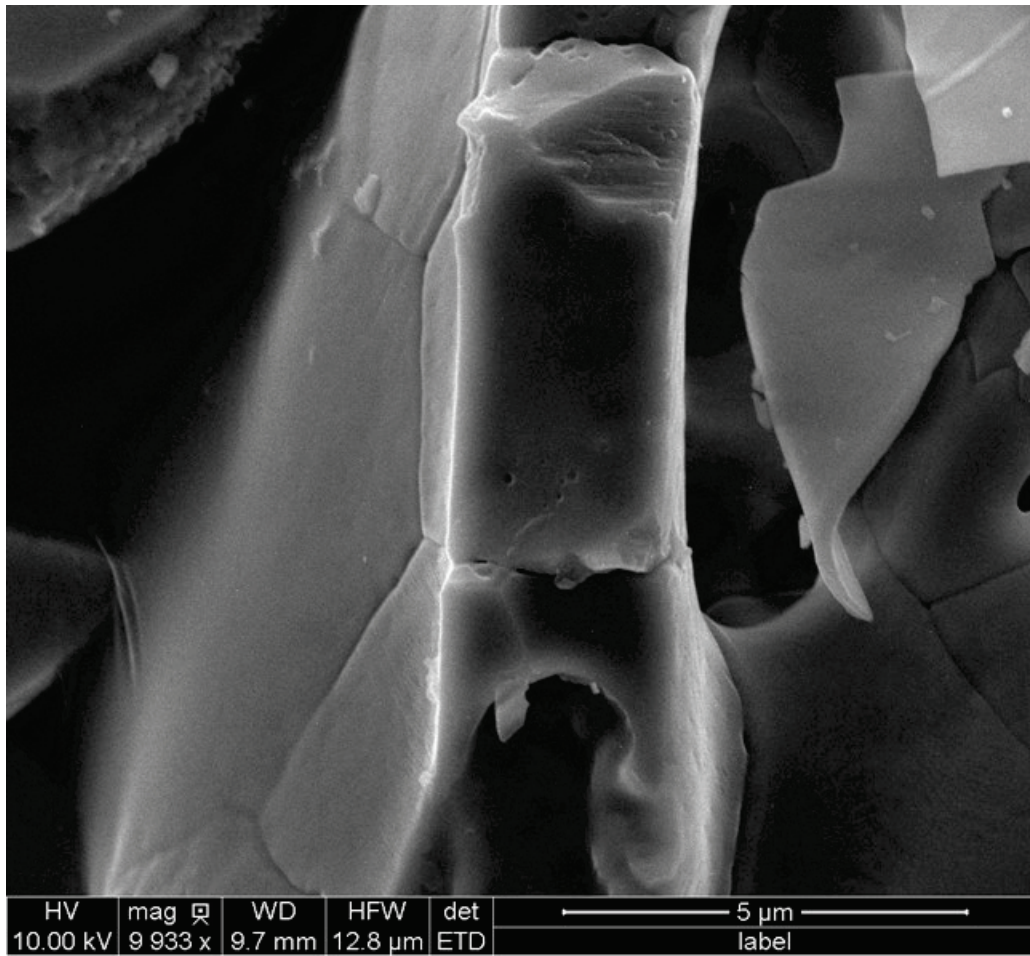


Fig. 2 (B) Scanning electron micrograph of  $\text{Al}_2\text{O}_3:\text{Cr}$  combustion product.

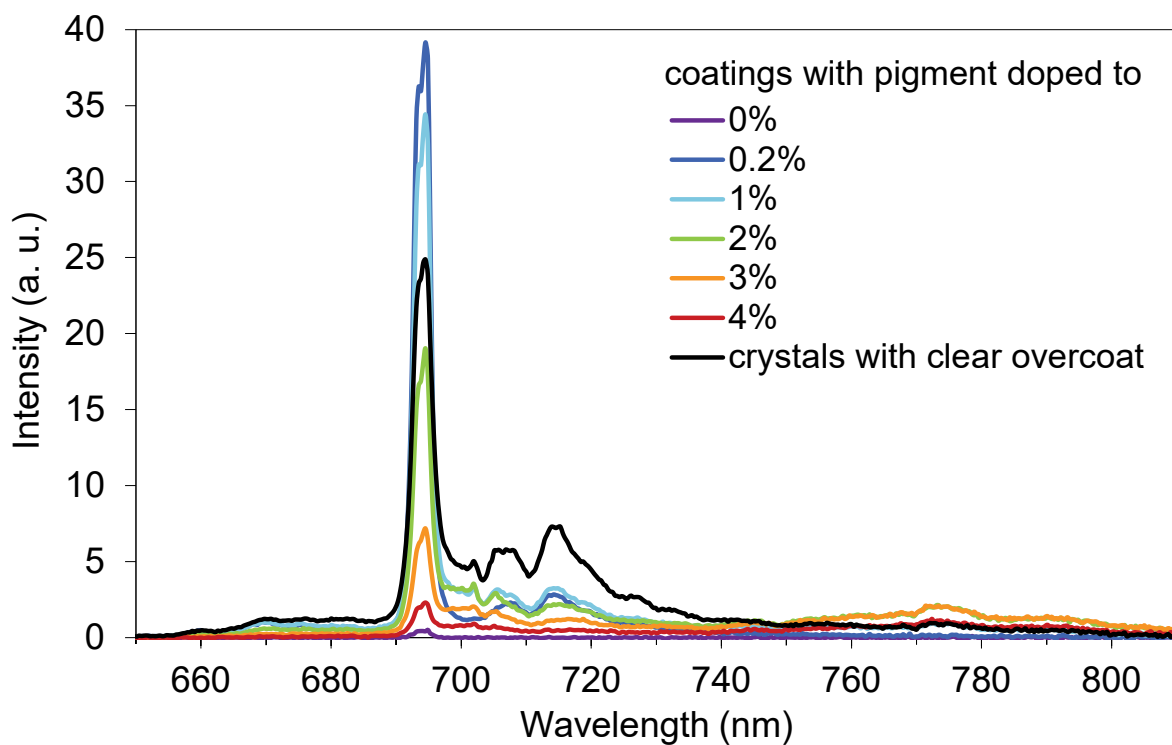


Fig. 3 (A) Spectral fluorescence of our samples. Percentages are the weight percent of  $\text{Cr}_2\text{O}_3$  in the pigments.

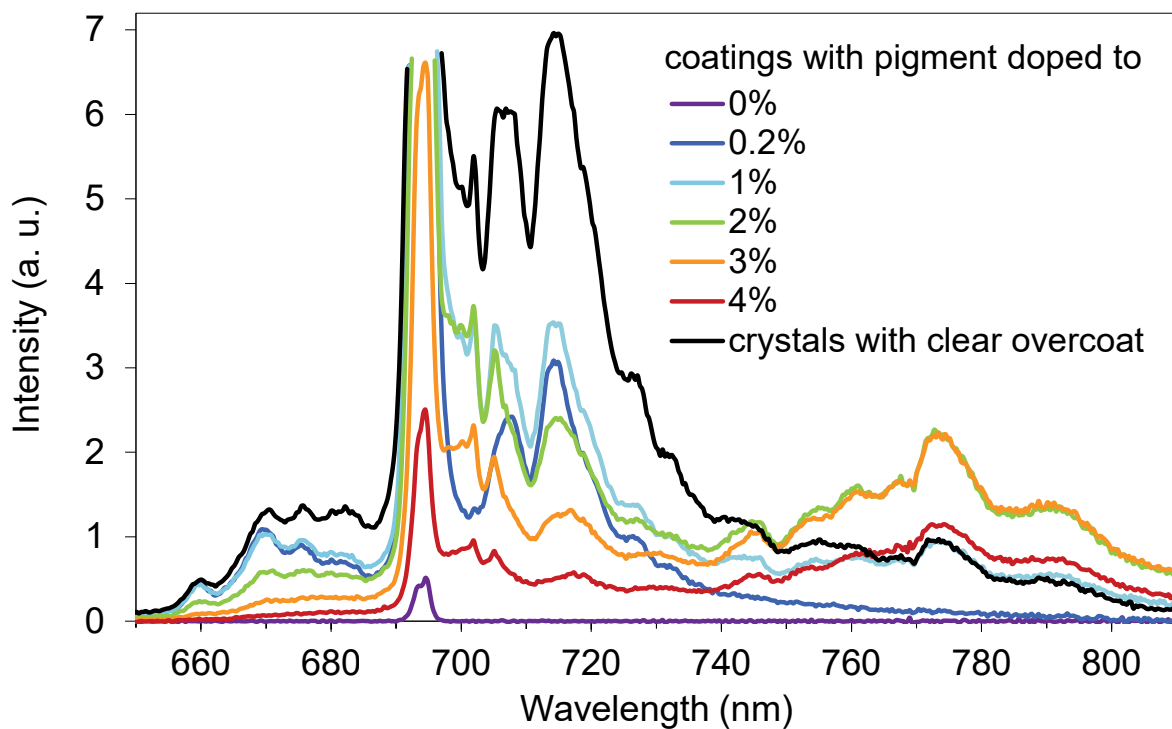


Fig. 3 (B) Details of fluorescence shown in Fig. 3 (A).

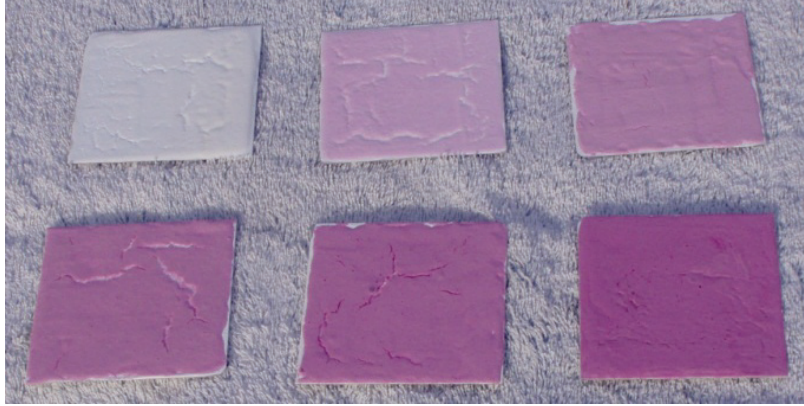


Fig. 4 (A) Coatings containing ruby powders with 0, 0.2, 1, 2, 3, and 4% doping. The darker coatings contain pigments with more chromium.

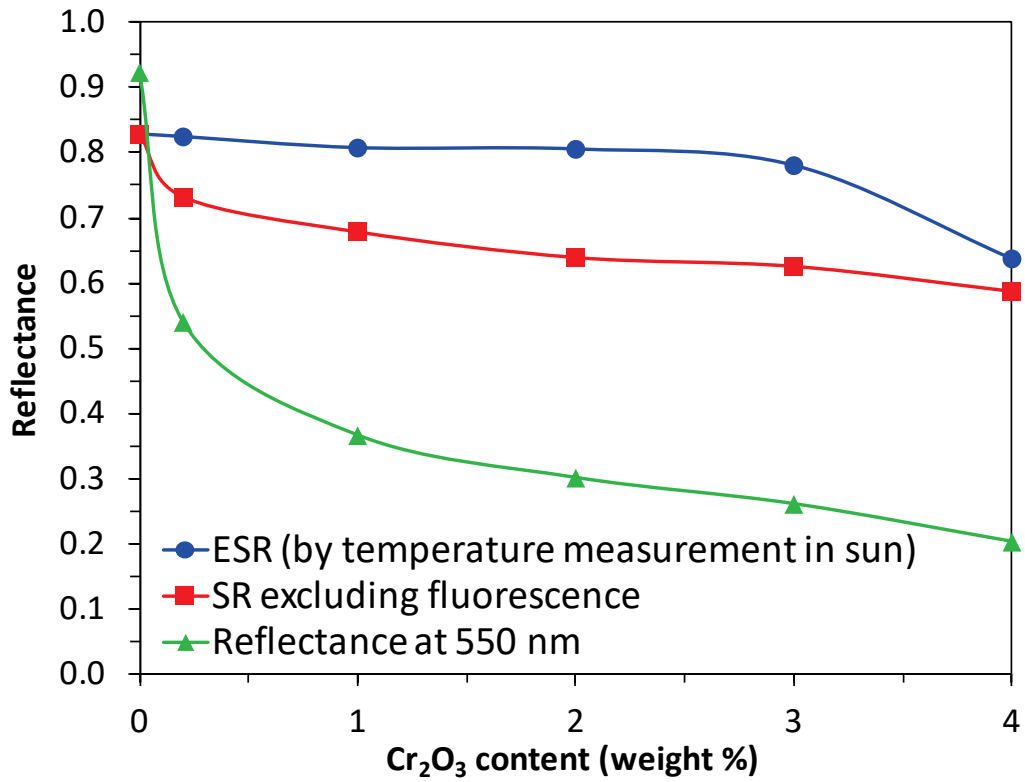


Fig. 4 (B) Effective Solar Reflectance (ESR), Solar Reflectance (SR) and visual brightness: reflectance at 550 nm.

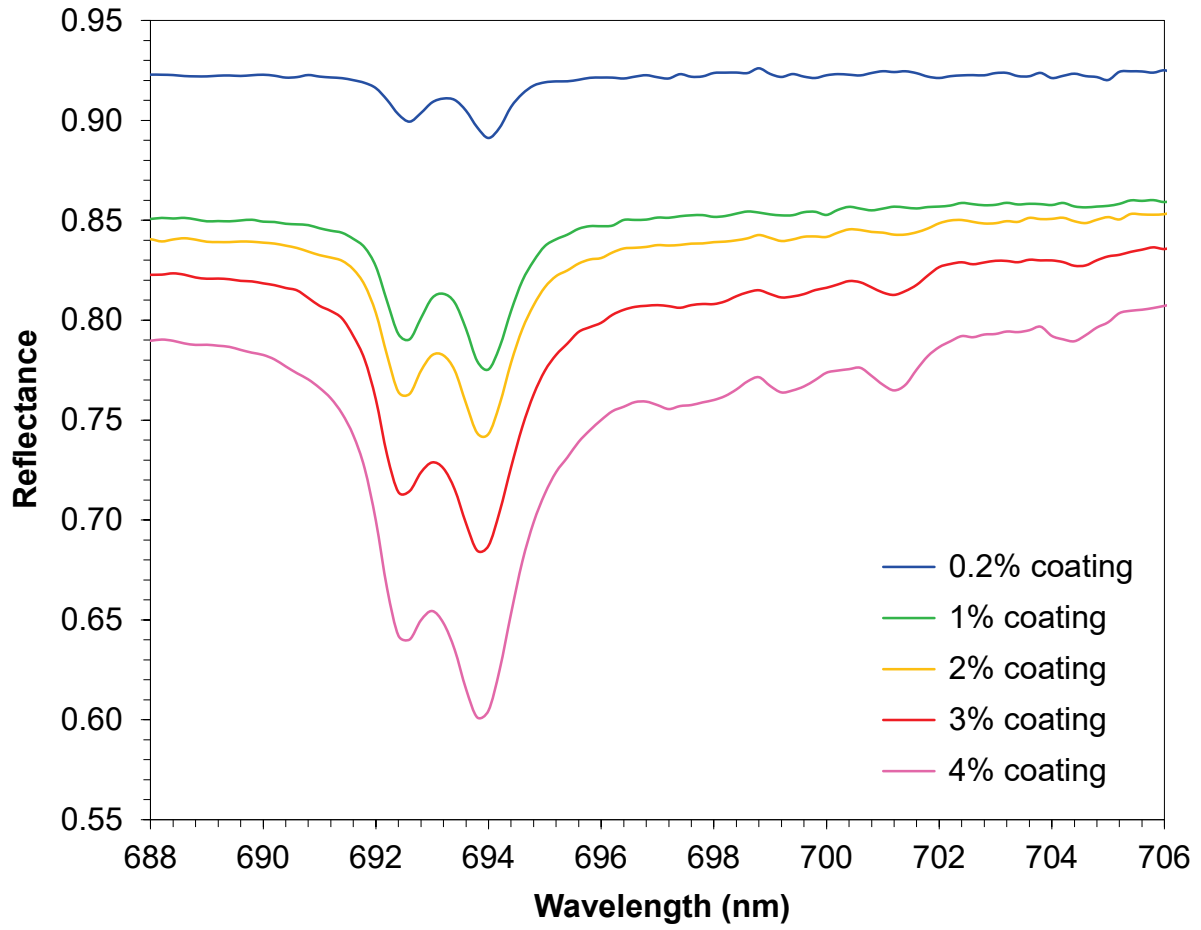


Fig. 5 High resolution reflectance spectra near the R-lines. In addition to spectral features, broadband absorption is present that increases with doping.

Task Report Appendix C:  
Pre-print of blue pigment article (Berdahl et al. 2018)

# High Quantum Yield of the Egyptian Blue Family of Infrared Phosphors ( $\text{MCuSi}_4\text{O}_{10}$ , $\text{M} = \text{Ca}, \text{Sr}, \text{Ba}$ )

Paul Berdahl<sup>a\*</sup>, Simon K. Boocock<sup>b</sup>, George C-Y Chan<sup>a</sup>, Sharon S. Chen<sup>a</sup>, Ronnen M. Levinson<sup>a</sup>, and Michael A. Zalich<sup>c</sup>

<sup>a</sup> Heat Island Group, Lawrence Berkeley National Laboratory

<sup>b</sup> Shepherd Color Company, Cincinnati, OH 45246

<sup>c</sup> PPG, Coatings Innovation Center, Allison Park, PA 15101

\* Corresponding author, paul.berdahl@gmail.com

## Abstract

The alkaline earth copper tetra-silicates, blue pigments, are interesting infrared phosphors. The Ca, Sr, and Ba variants fluoresce in the near-infrared at 909, 914, and 948 nm, respectively, with spectral widths on the order of 120 nm. The highest quantum yield  $\phi$  reported thus far is ca. 10%. We use temperature measurements in sunlight to determine this parameter. The yield depends on the pigment loading (mass per unit area)  $\omega$  with values approaching 100% as  $\omega \rightarrow 0$  for the Ca and Sr variants. Although maximum quantum yield occurs near  $\omega = 0$ , maximum fluorescence occurs near  $\omega = 70 \text{ g m}^{-2}$ , at which  $\phi = 0.7$ . The better samples show fluorescence decay times in the range of 130 to 160  $\mu\text{s}$ . The absorbing impurity CuO is often present. Good phosphor performance requires long fluorescence decay times and *very* low levels of parasitic absorption. The strong fluorescence enhances prospects for energy applications such as cooling of sunlit surfaces (to reduce air conditioning requirements) and luminescent solar concentrators.

## 1 Introduction

Egyptian blue,  $\text{CaCuSi}_4\text{O}_{10}$ , and Han blue,  $\text{BaCuSi}_4\text{O}_{10}$ , have been utilized as important blue pigments for literally thousands of years.<sup>1</sup> The strontium variant,  $\text{SrCuSi}_4\text{O}_{10}$ , is less well known but is a similar blue pigment.<sup>2</sup> Accorsi et al.<sup>3</sup> provided an early description of the fluorescence of Egyptian blue and its application to artworks from ancient Egypt. The fluorescent emission spectra of the Ca and Sr compounds are very similar, whereas the Ba compound emits at slightly longer wavelength and with a broader spectrum. An important recent paper by Borisov

et al.<sup>4</sup> displays excitation and emission spectra for the three compounds. For Egyptian blue, they also reported that the decay time  $\tau$  is about 159  $\mu\text{s}$  for their solid-state synthesized material. Grinding to reduce the particle size yields shorter decay time of 126  $\mu\text{s}$ , which they attributed to the introduction of defects by mechanical stress during grinding. This behavior is typical for phosphors.<sup>5,6</sup> Borisov et al. also found  $\tau = 139 \mu\text{s}$  for Kremer Pigmente's Egyptian blue, in agreement with the value to be reported here of 137 ( $\pm 4$ )  $\mu\text{s}$ .<sup>4</sup>

Applications of the near-infrared fluorescence of these blue compounds include optical chemosensors.<sup>4,7</sup> In these sensors excitation of two or more phosphors can produce fluorescent signals which when ratioed can be used to determine parameters such as pH. Biological labeling applications can be found in which the larger penetration depth of near-infrared vs. visible light is an advantage.<sup>8</sup> Near-infrared fluorescence also has application in optical electronics such as lasers.<sup>9</sup>

*Energy* applications of the alkaline earth copper silicate phosphors now look increasingly attractive due to high quantum yield. The application that motivates the current research is energy conservation by reducing the temperature of sunlit objects. Current technology for this purpose relies on high near-infrared reflectance.<sup>10</sup> If an architect specifies blue or another dark color for a roof rather than white, the roof can be cooler in sunlight (saving air conditioning energy) if it efficiently rejects the invisible near-infrared component of sunlight. This paper addresses the additional advantage gained if the roof also fluoresces in the deep red or near-infrared.<sup>11</sup> For luminescent solar concentrator (LSC) applications, a large thin transparent plate absorbs sunlight and then fluoresces near-infrared energy that eventually emerges from the edges of the plate for photovoltaic conversion to electricity.<sup>12,13</sup>

Long radiative lifetimes are desirable as they indicate the relative weakness of competing non-radiative relaxation mechanisms and therefore lead to higher quantum yield (efficiency) of the fluorescence process. However, long lifetimes are not sufficient for high quantum yield because parasitic absorption can lead to mere heating without fluorescence. Parasitic absorption can interfere with the excitation process, and with the emission process. Thus, both corresponding spectral ranges are important. For the specific impurity CuO, important for the present work, parasitic absorption occurs both in the excitation and in the emission spectra. If a parasitic impurity is added to (or not removed from) a fluorescent phosphor, we expect a diminished quantum yield but an unchanged decay time.

Measurements of fluorescence intensity can be used to determine the quantum yield of phosphors. However, the emitted light need not have a simple angular distribution, so an integrating sphere is needed to collect the fluorescence. Also, calibrated spectrometers are needed. Thus, complete quantum yield measurements are not convenient, and are less available in the literature than fluorescence decay lifetimes. The method of De Mello et al.<sup>14</sup> has been employed. Based on this method, the quantum yield of Kremer Egyptian blue is reported as 10.5%.<sup>3</sup> For the Sr and Ba analogs fabricated by hydrothermal synthesis, quantum yields are reported to be 8.5% and 6.9%, respectively.<sup>15</sup>

In this work, we use a novel method for determination of quantum yield, namely temperature measurements in full sunlight.<sup>11</sup> This approach is motivated by the “cool roof” application, in which we want to know how much the sunlit roof (or other facade) is cooled by its fluorescence. Test sample temperatures are compared in full sunlight with calibrated non-fluorescent gray samples, to determine the effective solar reflectance (ESR). The solar reflectance (SR) is determined in the usual way based on spectral solar reflectance (excluding fluorescence) and a standard solar spectrum. The difference ESR - SR represents the fluorescence contribution to the ESR. From this contribution, and by knowing the spectrum of the fluorescence, we can determine the number of photons emitted. The number of incident solar photons absorbed in the excitation spectral range is determined from the spectral reflectance. Finally, the quantum yield is the ratio of fluoresced to absorbed numbers of photons. We find that the pigment loading  $\omega$  (pigment mass per unit area, in  $\text{g m}^{-2}$ ) affects the quantum yield  $\phi$  with larger concentrations having lower  $\phi$ ; this effect is attributed primarily to parasitic absorption. Peak values of the quantum yield thus occur at low values of  $\omega$ , below  $10 \text{ g m}^{-2}$ . On the other hand, for a given amount of excitation radiation, peak values of fluorescence occur for  $\omega$  in the range of 20 to  $100 \text{ g m}^{-2}$ , with the larger values corresponding to situations in which parasitic absorption is less important.

## 6 Experimental and theoretical details

### 6.1 Synthesis

The barium and strontium copper silicate blue pigments were synthesized at Shepherd Color using traditional ceramic techniques. Starting raw materials, in appropriate proportions, were mixed together intimately using intensive dry blending. The dry mixtures were homogenized by screening through fine brass cloth mesh, then administered to ceramic crucibles for firing. For a source of alkali-earth the corresponding carbonate was used, barium or strontium as appropriate. For copper, finely ground copper (II) oxide was chosen, while silica was furnished as finely ground amorphous silica, free of alkali. Lanthanum was introduced as the lanthanum (III) carbonate, and was always accompanied by an equimolar amount of lithium carbonate to maintain charge balance.<sup>16</sup>

All pigments were built to a parent stoichiometry of  $M(\text{Cu})\text{Si}_4\text{O}_{10}$ , or  $M_x(\text{La})_x(\text{Li})_x(\text{Cu})_y\text{Si}_4\text{O}_{10}$ , where  $M$  is either Ba or Sr, and the coefficients  $x$  and  $y$  sum to unity. The mixed powders were calcined in air at  $850 \text{ }^\circ\text{C}$ , with a soak no shorter than five hours. The resulting fired products were coarse ground in a mortar and pestle, then fine ground once on a jet-mill, or wet-ground with fine zirconia beads in DI water to a tractable size.

Elemental composition was determined by x-ray fluorescence, which found levels of all elements (excepting lithium and oxygen) to be consistent with the target compositions.

The crystal phase of each finished pigment was confirmed by x-ray powder diffraction, by reference to patterns for parent phases found in the ICDD (International Centre for Diffraction

Data) PDF-4+ database. The barium copper tetra silicate, with equimolar lanthanum and lithium substitution for copper and barium, reported as Effenbergite,  $\text{BaCuSi}_4\text{O}_{10}$ , having powder pattern 04-007-5484. The unsubstituted strontium copper silicate analog to Han blue reported as Wesseltite, pattern 04-009-5401. The median particle sizes of the barium and the strontium compound powders were 1.3 and 49  $\mu\text{m}$ , respectively.

## 6.2 Instrumentation

Fluorescence measurements conducted at Lawrence Berkeley National Laboratory (Berkeley Lab) used a compact Ocean Optics S2000 spectrometer fitted with a 150 mm Labsphere integrating sphere. (We use the term fluorescence as a general synonym for photoluminescence, and avoid the term phosphorescence.) The light source is a tungsten incandescent lamp with xenon gas fill. The incident light is directed through a port on the top of the integrating sphere onto the sample at a port on the bottom of the sphere. A 725 nm short-pass filter with optical density 4 (attenuation better than  $10^{-4}$  in the stop band) blocks excitation light that would otherwise overlap with the fluorescence spectrum. The spectrometer receives light from the integrating sphere by means of an optical fiber and uses a diffraction grating to disperse the spectrum on a silicon array detector. The silicon detector covers a spectral range of about 500 – 1,100 nm.

Pulsed fluorescence measurements used an in-house fabricated pulse generator to drive three red light emitting diodes (620 nm) each with 1 ampere, 10  $\mu\text{s}$  pulses with  $\sim 1$  ms pulse repetition interval. The fluoresced light was passed through a 695 nm long-pass filter and focused onto a Thorlabs DET 200 fast (ns) photodiode. The photodiode output was processed by an SRS 570 low noise current preamplifier and then acquired by a Tektronix 3054 digital oscilloscope. The  $1/e$  response time of the whole detection system is approximately 3.4  $\mu\text{s}$ .

Diffuse spectral reflectance measurements were made with a Perkin-Elmer Lambda 900 UV-VIS-NIR spectrometer fitted with a 150 mm Labsphere integrating sphere. A photomultiplier tube serves as detector from 250 to 860 nm; at longer wavelengths up to 2,500 nm, a PbS photoconductive detector is employed. The standard solar spectral irradiance used to compute solar averages (AM1GH, air-mass 1 global horizontal) represents the radiation received by a horizontal surface with the sun overhead on a clear day, summing to 1,090  $\text{W m}^{-2}$ .<sup>17</sup>

## 6.3 Sample preparation

Phosphor powders are useful for screening materials. However, loose powders can introduce variability in repeated experiments depending on how the powder is packed or otherwise arranged. Powders suspended (dispersed) into a coating offer the advantage of durability, and reference samples can be used repeatedly. The phosphors have a tetragonal structure with refractive indices of 1.63 (ordinary ray, electric field perpendicular to the c-axis) and 1.59 (extraordinary ray).<sup>2, 18, 19</sup> Since the acrylic polymer has an index of  $\sim 1.5$ , scattering is reduced relative to a powder in air, and the color is a darker blue. All the pigmented coating samples used in the current work were prepared at Berkeley Lab by hand-dispersing pigments into a

transparent acrylic base (Liquitex gloss medium & varnish) with a spatula, which does not lead to an ideal dispersion. These coatings crack upon drying (and are patched to fill cracks), and do not resemble commercial coatings. Coatings are applied with a spatula over a white substrate which is itself composed of three brushed layers of an acrylic artist's white coating (total dry film thickness about 150  $\mu\text{m}$ ) on an aluminum panel. This white substrate has a reflectance of  $\sim 0.9$  from 500 to 1,000 nm, and serves to reflect excitation radiation that passes through the test coating, enhancing absorption by the phosphor. Additionally, the diffuse fluoresced emission is directed outward from the coating by the white substrate.

## 7 Theoretical considerations

It would be useful to have a complete numerical radiative transfer model for phosphor particles suspended in a medium above a white or black substrate. However, modeling the radiative performance of even non-fluorescent coatings is complex.<sup>20,21</sup> If the incident light is collimated, one needs to keep track of how the diffuse radiation field develops due to scattering. One also needs to know the differential scattering cross section of the particles. The treatment of scattering needs to be approximated unless complete solutions of the Boltzmann-type photon transport equation are to be found. Further, there are interface reflectances that depend on photon incidence angle and polarization; total internal reflection at the top interface is particularly important. Such a code is certainly achievable, but we leave this problem to others. We resort to qualitative and semi-quantitative analysis supported by experimental data.

Consider a thin phosphor-pigmented layer (coating) supported by either a white or black substrate, illuminated with excitation radiation by a beam at normal incidence. Here thin means that the phosphor only absorbs a small fraction of the incident radiation. Also, for simplicity, assume that the black and white layers are perfect, with reflectances of 0 and 1. Scattering by the phosphor is neglected. If the absorption coefficient (with units of inverse length) is  $\alpha$  and the layer thickness  $h$ , then the fraction of incident radiation absorbed by the black-backed layer is  $\alpha h$ . For the white-backed layer additional absorption is caused by the diffusely reflected radiation. As an approximation, the typical path length of the reflected radiation is increased by a factor of two. (The factor of two is exact in the limit  $\alpha h \rightarrow 0$ , but slightly smaller factors will apply in realistic situations.) Thus, the total absorbed fraction of the white-backed layer is roughly  $3 \alpha h$ . Even this value is an underestimate, due to the large reflectance for diffuse radiation ( $\sim 0.6$ ) at the underside of the top interface, due total internal reflection.<sup>20</sup> See Figure 19.

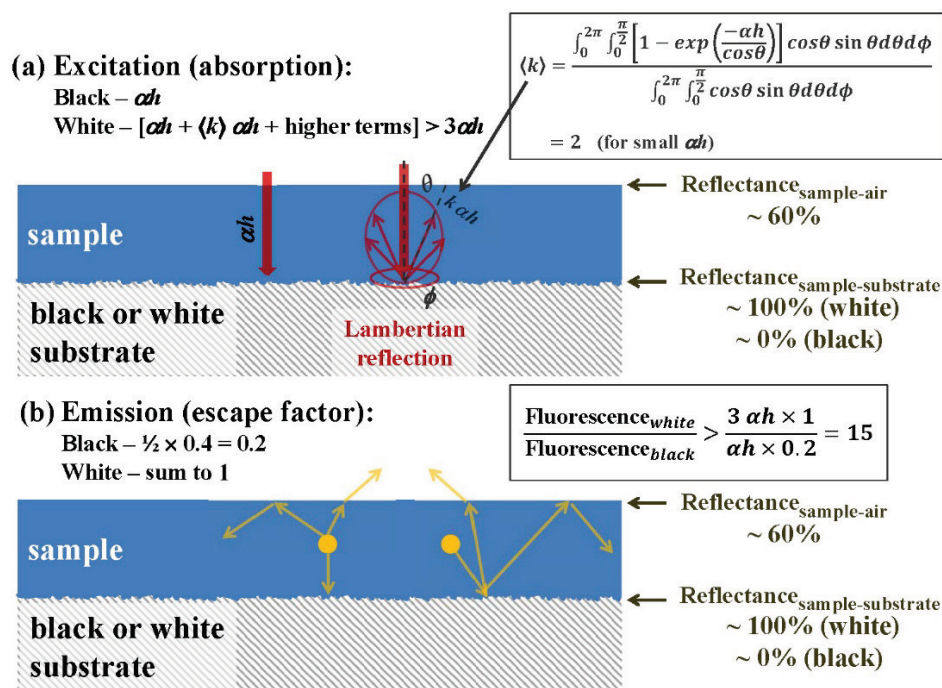


**Figure 19. Schematic depiction of radiation transport in thin blue fluorescent coatings over ideal white or black substrates. (a) Absorption of normally incident excitation radiation. (b) Emission of near-infrared fluorescence.**

Almost all of the fluoresced radiation emerges from the white-backed layer whereas only about one fifth of the radiation emerges from the black-backed layer. (Of the upward-emitted radiation, only 2/5 is transmitted by the upper interface.) Therefore, we expect the white-backed layer to fluoresce with about 15 times the intensity of the black-backed layer. In one experiment, with a coating containing  $12 \text{ g m}^{-2}$  of strontium copper silicate ( $\text{SrCuSi}_4\text{O}_{10}$ ) phosphor on a microscope slide, we found that the fluorescent intensity with a white surface below the slide was like that of a coating applied directly to a white substrate. Replacing the white surface below the slide with black electrical tape adhered underneath the slide yielded a fluorescent intensity that was smaller by a factor of 17. Thus, a reflective underlayer greatly enhances fluorescence.

As already mentioned long fluorescence decay times are desired. From the literature on phosphors generally,<sup>5,6</sup> and from Borisov et al.,<sup>4</sup> we note that larger crystalline particles, free from deleterious impurities, strain, and other defects are desirable. If small particles must be produced by grinding, reducing the decay time, post annealing may be helpful. Long decay times are indicative of the weakness of deleterious non-radiative relaxation processes and are required for high quantum yields. Of course, parasitic absorption can interfere with high

quantum yields, but it is helpful that long decay times can be measured even in the presence of parasitic absorption.

## 7.1 Determination of quantum yield

In classical measurements of quantum yield one wavelength near the center of the excitation range is used and the emission spectrum is integrated to determine the number of emitted photons. In the case at hand, the total emitted energy is determined from the ESR (effective solar reflectance) calorimetric measurement of temperature in sunlight. The fluorescence contribution to the ESR is then determined by subtracting the conventional spectrometer-measured SR (solar reflectance). (In general, the conventional SR measurement may require filters to exclude fluorescence,<sup>11</sup> but for this paper they are not needed.) The spectrum of emission is determined separately. Since the spectral distribution is known, the emitted photon flux can be determined from the energy flux.

Accounting for the number of excitation photons absorbed is more subtle. The spectral absorptance  $A$  of a sample is compared with that of a sample with no pigment,  $A_0$ . If the coating layer is optically thin, then the absorptance of the pigment can be approximated by  $A - A_0$ . If, on the other hand, the layer is optically thick, with  $A$  approaching unity, then the absorption of the substrate is nearly zero. With acceptable accuracy for our problem, in which  $A_0$  is small, we perform a linear interpolation for  $A'$ , the pigment absorption, as

$$A' = (A - A_0) / (1 - A_0). \quad (1)$$

Thus  $A' = 0$  when  $A = A_0$ , and  $A' = 1$  when  $A = 1$ . For the integration over wavelength, we multiply by the spectral photon flux of our standard solar spectrum and, for convenience, take the ends of the excitation spectrum as the points at which the excitation strength falls to 5% of its peak value, based on the spectra shown by Borisov et al.<sup>4</sup>

Also, we wish to determine the fraction of the fluoresced photons which are absorbed by the substrate with  $A_0 = 0.1$  rather than emitted by the layer. If  $A_0$  were zero, this fraction would be 0%. For a downward-directed photon, the absorption probability is approximately  $A_0$ . Such a photon may be reflected several times between the white substrate and the top of the coating; the resulting absorption probability is nevertheless  $A_0$ . An upward-directed photon is either transmitted by the top interface, with 40% probability, or reflected with 60% probability. On being reflected, it is now downward directed and consequently has probability  $A_0$  for absorption. Summing the possible outcomes, we find that the overall probability of absorption is  $0.8 A_0$ . Thus, we conclude that 8% of the fluoresced photons are absorbed by the imperfect white substrate.

The state of the art of ESR measurements is still not very well developed; however, work is being conducted to improve the technique.<sup>22</sup> This latest technique uses a rotating sample stage to ensure that identical specimens will attain equal temperatures. The basic measurement

difficulty is temperature fluctuation caused by wind. Convective heat transfer is temporally and spatially irregular due to atmospheric turbulence. Measuring only during periods of low wind speed is helpful but not a panacea. The effective solar absorptance,  $ESA = 1 - ESR$  tends to have errors on the order of 5% of ESA. Thus, for example, if  $ESA = 0.40$  ( $ESR = 0.60$ ), the uncertainty is roughly  $\pm 0.02$ . Now the fluorescence contribution to ESR may be on the order of 0.10, or even smaller, so that experimental error can be undesirably large. This difficulty is ameliorated by utilizing ESR measurements only in favorable circumstances. Most fluorescence measurements are performed on a relative basis, comparing unknown samples to a “bright” reference sample, which is in turn calibrated by the ESR technique.

## 8 Optical measurements

### 8.1 Fluorescence

After a process of screening pigment powders<sup>23</sup> for bright near-infrared fluorescence two promising materials were found to be  $SrCuSi_4O_{10}$  and a variant<sup>16</sup> of Han blue ( $BaCuSi_4O_{10}$ ) which is co-doped with La and Li. These pigments were synthesized by the solid-state reaction technique at Shepherd Color and initially screened at PPG. Selected samples were forwarded to Berkeley Lab for additional study.

Figure 20a shows fluorescence curves for five acrylic coatings pigmented with  $SrCuSi_4O_{10}$  powder. The dips at 880 and 945 nm are merely artifacts of the spectrometer system. Further, the silicon array detector has diminished sensitivity at longer wavelengths. Thus, the central wavelength in these spectra is a slightly less than 900 nm, whereas calibrated spectrometer measurements<sup>4</sup> find a nearly symmetrical broad peak at 914 nm. Despite the limitations of the spectrometer, one can see that progressing from low to high pigment concentration, the spectrum shifts slightly to longer wavelengths. One likely explanation is that the intrinsic absorption of the strontium copper silicate compound extends from shorter excitation wavelengths to the 880 nm region and thereby encroaches on the left side of the fluorescence spectrum. Additionally, we suggest that this red shift is partly due to small amounts of the black absorbing impurity CuO. CuO is a semiconductor with band edge in the 900 nm region which becomes less absorptive with increasing wavelength in the 900 nm region.<sup>24, 25</sup> Stated another way, CuO selectively attenuates the shorter wavelengths and thereby causes a small red shift.

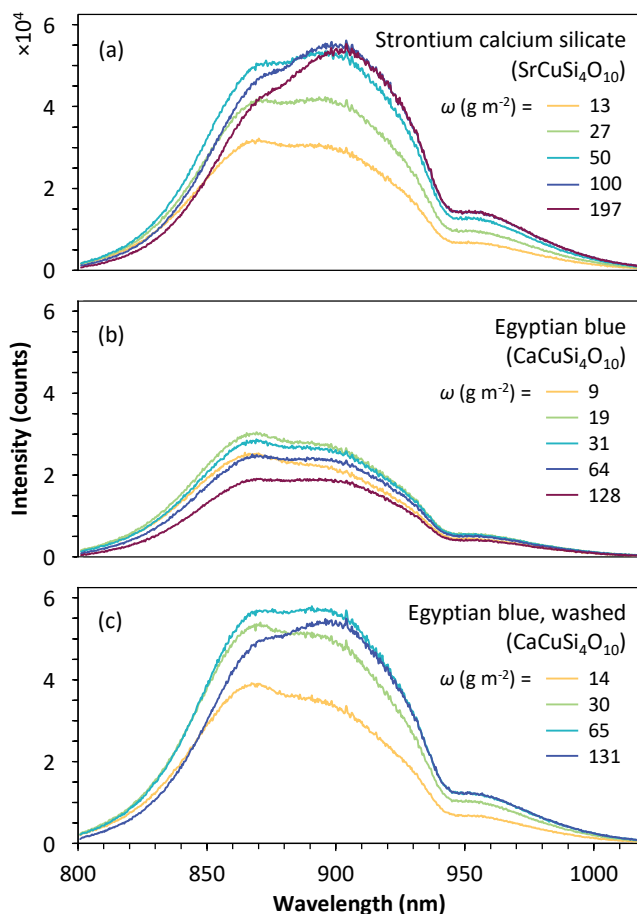


**Figure 20. Measured spectral fluorescent intensities of (a) five coatings pigmented with strontium calcium silicate; (b) five coatings with commercial Egyptian blue pigment from Kremer Pigmente; and (c) four coatings with the same commercial Egyptian blue pigment, that has been treated with HCl to reduce the amount of CuO. Each coating was applied to a white substrate.**

Figure 20b shows analogous fluorescence data, acquired as in Figure 20a, but for commercially available  $\text{CaCuSi}_4\text{O}_{10}$  (Egyptian blue from Kremer). Clearly, the Egyptian blue pigment is less fluorescent than the Sr compound. However, Figure 20c shows fluorescence data for Egyptian blue pigment that has been soaked in 0.3 M HCl for 12 hours (“washed”) to dissolve small amounts of CuO. The fluorescence of the purified Egyptian blue pigment is then quite comparable to that of  $\text{SrCuSi}_4\text{O}_{10}$  (strontium calcium silicate).

Decay time measurements are summarized in Figure 21. The curves are normalized to unity at zero time, then displaced vertically by 10% from one another for clarity. The top three curves are linear on the logarithmic plots, for which the experimental uncertainties are about  $\pm 4 \mu\text{s}$ . The La and Li doped Han blue ( $\text{BaCuSi}_4\text{O}_{10}$ ) data deviate from a straight line. One possible explanation is the presence of an additional, shorter time constant. It is tempting to think that it might contain some Han purple ( $\text{BaCuSi}_2\text{O}_6$ ), as this has a short time constant of  $20 \mu\text{s}$ . However, x-ray diffraction shows only a minor second phase of  $\text{BaSiO}_3$  which, lacking copper,

seems unlikely to be the source of the short time constant. The Han purple sample is comparably bright with the other materials at  $\sim 10 \mu\text{s}$ , but due to its short time constant the total number of photons is smaller by a factor of about seven. Our lifetime measurements are in good agreement with Fig. 5 of Ref. 4 for  $\text{SrCuSi}_4\text{O}_{10}$  and for Egyptian blue. For Han blue, there are some differences which are understandable since our sample is doped with La and Li, and there is a lack of a simple exponential decay. The time constants of the original and washed Egyptian blue are very similar—equal within experimental uncertainty—even though the HCl washed sample exhibits much stronger fluorescence.

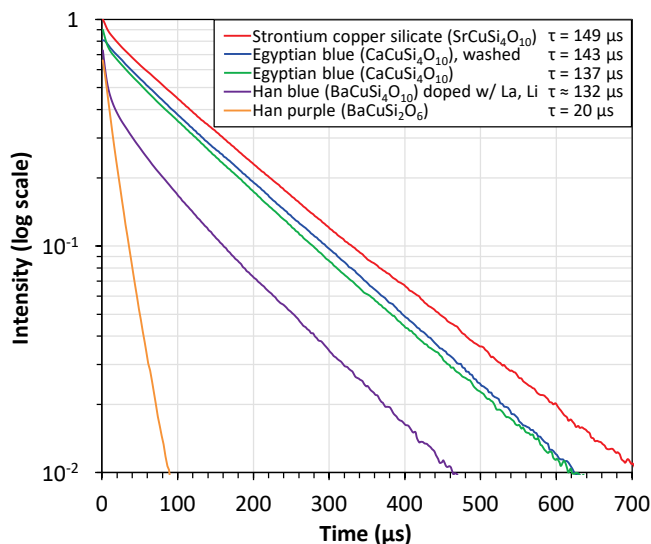


**Figure 21. Fluorescence decay curves. For the top three curves, the interval 25 to 300  $\mu\text{s}$  was used to extract the time constant  $\tau$ . The Han blue (La, Li doped  $\text{BaCuSi}_4\text{O}_{10}$ ) sample shows evidence of more than one decay; the longer decay was estimated based on the 125 to 400  $\mu\text{s}$  period. For Han purple ( $\text{BaCuSi}_2\text{O}_6$ ), the 25 to 100  $\mu\text{s}$  interval was used.**

Comparisons with the literature indicate that samples synthesized by hydrothermal methods generally have larger surface area and shorter decay time than those made by the solid-state method. For example, Ref. 15 gives 16 and 33  $\mu\text{s}$  for the Sr and Ba compounds whereas Figure 21 lists 149 and 132  $\mu\text{s}$ . Also, for Han (Chinese) purple, Ref. 26 gives 6.4  $\mu\text{s}$  whereas we have obtained 20  $\mu\text{s}$  for a commercial sample from Kremer. For Egyptian blue manufactured by Kremer, we have obtained 137  $\mu\text{s}$ , which as already mentioned, agrees well with Borisov et al.<sup>4</sup> Borisov et al. also found 159  $\mu\text{s}$  for unground samples by solid-state synthesis. Additional values reported for Egyptian blue by solid-state synthesis are 107  $\mu\text{s}$ ,<sup>3</sup> 142  $\mu\text{s}$ ,<sup>27</sup> and about 160  $\mu\text{s}$ .<sup>28</sup>

The fluorescence measurements presented in Figure 20 are summarized in Figure 22, which shows the area under each peak, relative to the area of the reference sample of  $\text{SrCuSi}_4\text{O}_{10}$  with pigment loading  $\omega = 100 \text{ g m}^{-2}$ . This reference sample has an effective solar reflectance (ESR) of

0.544, a spectrometer determined solar reflectance (SR) of 0.410, and therefore a fluorescence contribution of 0.134. Given the  $1,090 \text{ W m}^{-2}$  energy content of our reference solar spectrum, the fluorescence energy flux in full sun is  $146 \text{ W m}^{-2}$ . Further, the central photon wavelength is  $914 \text{ nm}$ , which allows us to estimate the photon flux as  $6.73 \times 10^{20} \text{ m}^{-2} \text{ s}^{-1}$ . Now we turn to the issue of determining the number of exciting photons that are absorbed.

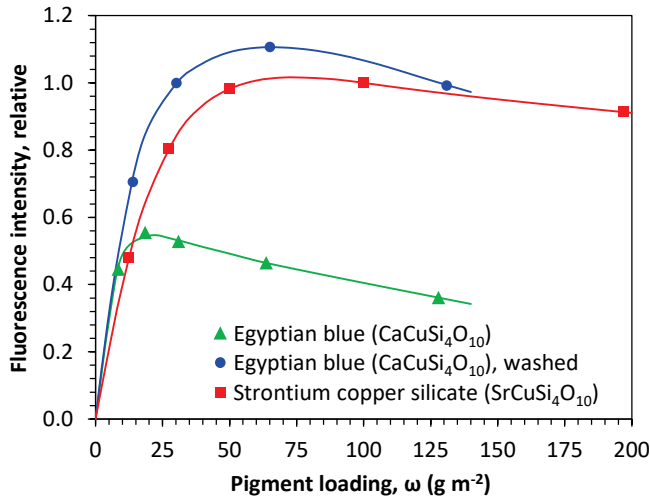


**Figure 22.** Intensity of fluorescence, integrated over wavelength, as a function of pigment loading, based on the data in Figure 20. The sample at  $\omega = 100 \text{ g m}^{-2}$  was used for reference and assigned the value 1.0.

## 9 Spectral reflectance measurements

Figure 23a shows spectral reflectance data for the five samples presented in Figure 20a. The top curve represents a sample with no pigment, i.e., a transparent acrylic coating over a white substrate. Comparing with the curves below, one can see that  $\text{SrCuSi}_4\text{O}_{10}$  absorbs from about 475 to 880 nm, which is the excitation region. There is only weak absorption between 880 and 1100 nm. Reflectance data for Egyptian blue appears in Figure 5b for the untreated pigment and Figure 5c for the Egyptian blue pigment washed with HCl. The untreated Egyptian blue shows much more absorption in the 880 to 1,100 nm region compared to the same washed pigment and the Sr pigment. It also shows less peak-to-valley variation in the visible region. Both characteristics can be attributed to parasitic absorption by CuO.

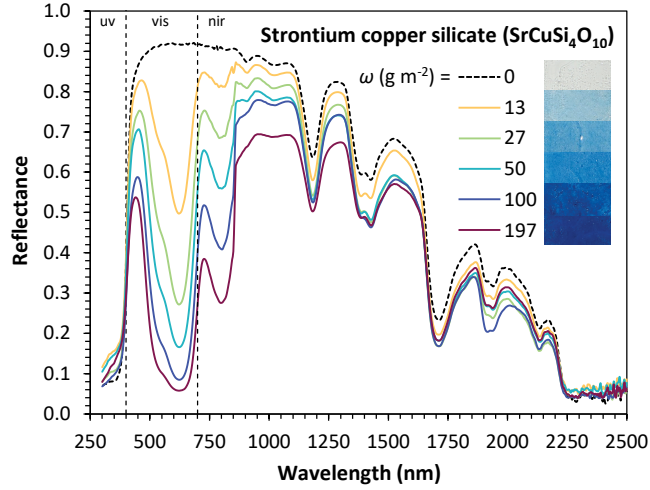


Figure 23a. Measured spectral reflectance of the coatings of Figure 20a and of one transparent coating with no pigment. Inset shows colors.

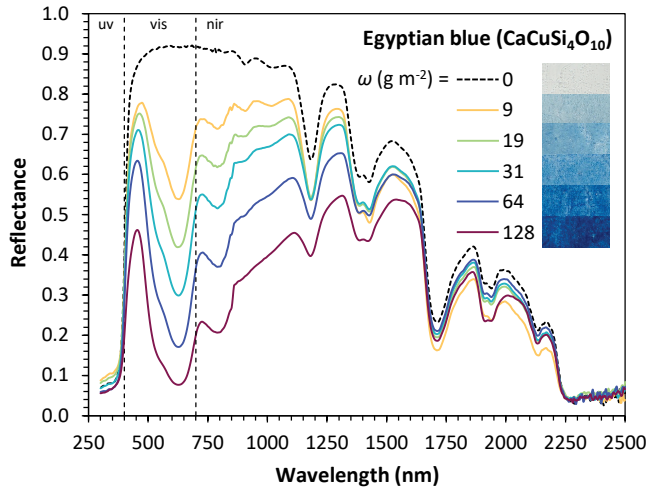
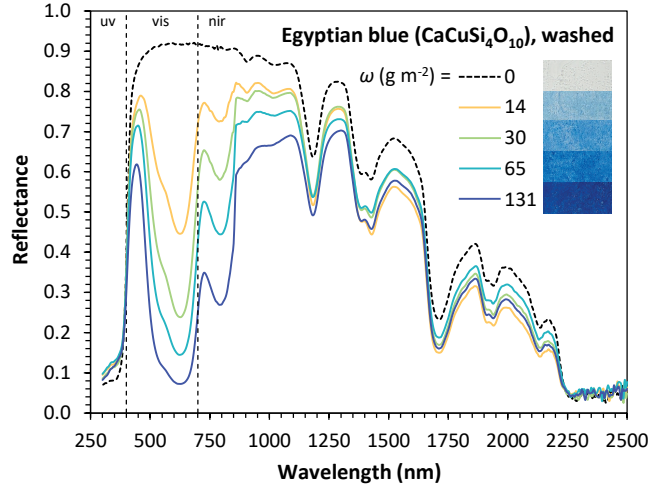
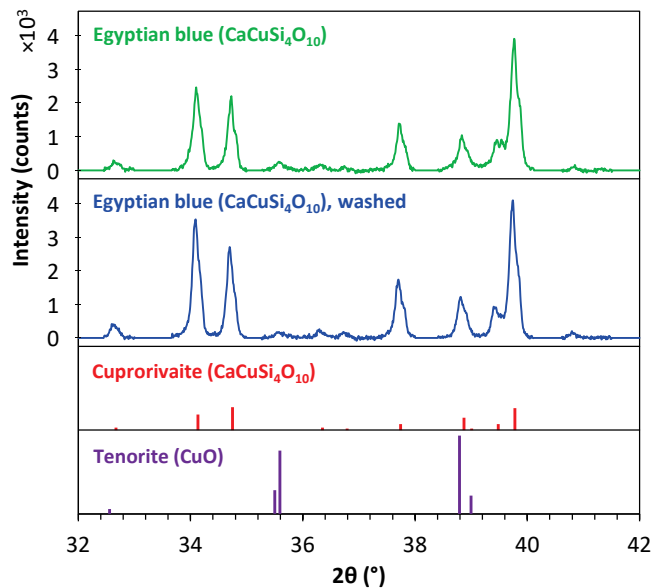


Figure 5b. Spectral reflectance and images of the coatings of Figure 20b (as received Egyptian blue).



**Figure 5c. Spectral reflectance and images of the coatings of Figure 20c (Egyptian blue washed with HCl).**

X-ray diffraction data in Figure 24, for the as-received and washed Egyptian blue powders, show small peaks at  $35.5^\circ$  due to CuO. The peak is smaller in the washed sample but still present. The optical reflectance data of Figs. 5 b, c are consistent: the parasitic absorption in the 880 to 1,100 nm region is reduced but not eliminated by washing. The visible region reflectance indicates that all samples are blue as shown in the insets, with high blue reflectance (400 to 500 nm) and low reflectance in the 500 to 700 nm region. The peak-to-valley distance of the untreated Egyptian blue is enhanced by the reduction of the CuO impurity.



**Figure 24. X-ray diffraction data vs. scattering angle  $2\theta$  for Egyptian blue, washed with HCl, and as received from Kremer. Both samples have some CuO (tenorite, small peak at  $35.5^\circ$ ), and there is less in the washed sample.**

The rate of photon absorption by the pigments is computed from the reflectance curves with and without pigments shown in Figure 23. As detailed earlier, the absorptance of the substrate is reduced to account for photons not striking the substrate due to absorptance by the pigment. The excitation region is taken to be 475 to 880 nm; photons outside this range are assumed not to excite the pigment. Figure 25 summarizes the rate of photon absorption.

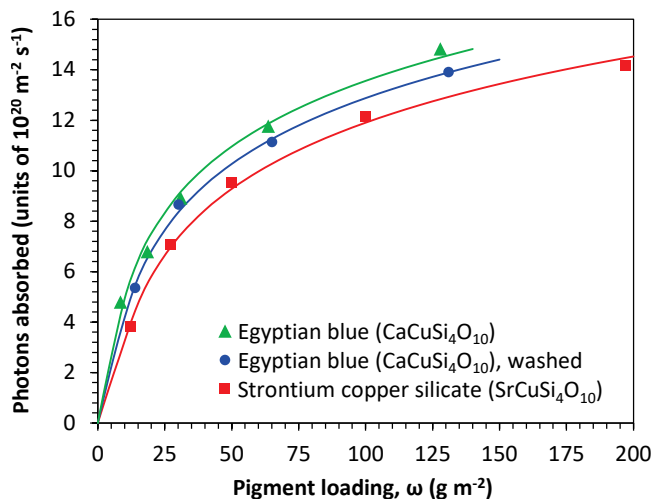


**Figure 25. Rate of photon absorption by the pigments between 475 and 880 nm in full sun computed from the spectral reflectance, the spectral reflectance of a sample with no pigment, and a standard solar spectrum.<sup>17</sup>**

## 9.1 Quantum yield

The quantum yield is now readily computed and is displayed in Figure 26. Most notably, the quantum yield  $\phi$  varies with the pigment loading  $\omega$  (mass per unit area) and, for small  $\omega$ , approaches unity for the  $\text{SrCuSi}_4\text{O}_{10}$  and  $\text{CaCuSi}_4\text{O}_{10}$  compounds. Due to the limited measurement accuracy of the ESR measurement for the  $100 \text{ g m}^{-2}$   $\text{SrCuSi}_4\text{O}_{10}$  calibration sample, the values of  $\phi$  are uncertain by ca.  $\pm 20\%$ . Nevertheless, the trends and overall high values are clear. Figure 22 shows that the fluorescence is maximum near  $70 \text{ g m}^{-2}$  for the better Sr and Ca compounds. Figure 26 then shows that at that maximum the quantum yield is ca.  $0.70 (\pm 0.15)$ . It seems likely, that if the impurity concentration of CuO can be further reduced, even higher performance may be feasible.

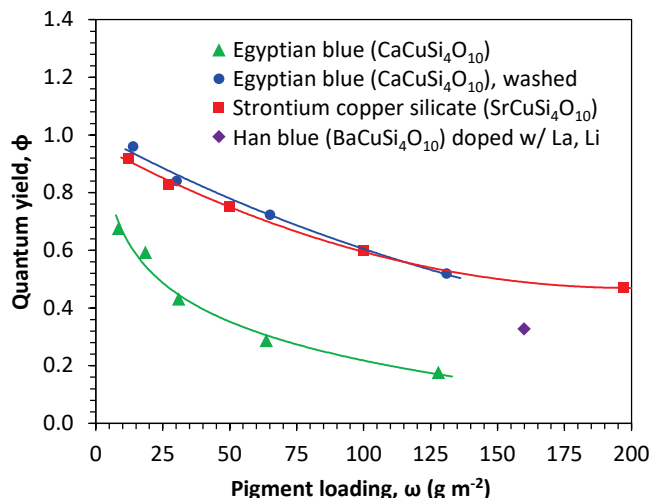


**Figure 26.** The quantum yield of the pigmented coatings as a function of pigment loading (areal density), based on the data in Figure 22 and Figure 25. The single data point for the Han blue pigment is based on a separate ESR measurement, required by the longer wavelength of fluorescence.

The quantum yield of the Han blue (BaCuSi<sub>4</sub>O<sub>10</sub>) compound doped with La and Li is based on a separate ESR measurement, subject to its own 20 % uncertainty, but it seems clear that this specific sample does not perform quite as well as its Sr and Ca counterparts.

In evaluating the quantum yield, we computed the number of excitation photons absorbed by the pigment, as distinct from the substrate. Also, we corrected for the fact that 8% of the fluoresced photons were absorbed by the imperfect white substrate.

## 10 Two energy applications

### 10.1 Cool roofing and facades

The efficient blue fluorescent pigments, calcium and strontium copper tetra-silicates, are suitable for fabricating blue-colored surfaces that stay cooler in the sun than non-fluorescent blues. The amount of fluorescent cooling can be more than 150 W m<sup>-2</sup> in full sun. Attention still must be paid to provide coating formulations that provide high near-infrared reflectance.

For the ruby pigments studied earlier<sup>10</sup> the use of colored co-pigments will reduce fluorescent performance because the excitation range covers the entire visible spectrum (except for the end of the red region in which fluorescence occurs). The currently investigated blue pigments do not absorb blue light. Consequently, a co-pigment can introduce absorption in the short wavelength part of the visible spectrum without impairing fluorescence. For example, a yellow co-pigment can be added to blue provide a green color. Further, an orange pigment can be added to obtain a cool black. Figure 27 shows four images of a coating with SrCuSi<sub>4</sub>O<sub>10</sub> pigment

by itself (blue), mixed with either of two yellow pigments to make green, and coated over orange to make a blue-shade black. Table 1 tabulates the performance of these samples.

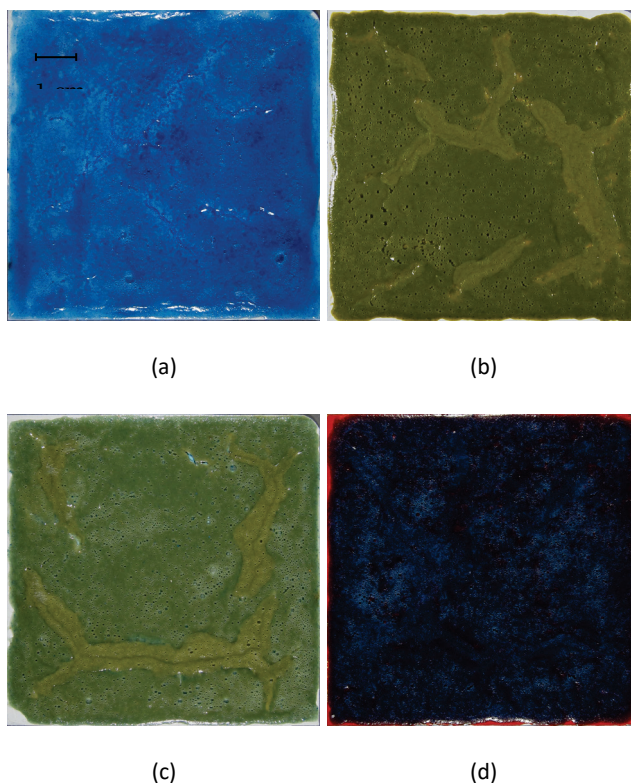


**Figure 27. Coating samples with the  $\text{SrCuSi}_4\text{O}_{10}$  pigment with a bright white undercoat. (a) blue pigment alone (b) blue mixed with azo yellow (Diarylide yellow, PY83 HR70) (c) blue mixed with Shepherd yellow 193 (A mixed oxide of Cr, Sb, Ti). Discoloration on green panels is caused by attempts to patch cracks that occurred during drying. (d) Coating sample, a blue-shade black in color, using the pigment over an orange coating, over white. The orange was Liquitex cadmium light red hue (imitation), one brushed coating. The spectrometer reflectance was 0.14 in the blue at 450 nm, 0.08 in the center of the visible (green) at 550 nm and 0.10 in the red at 650 nm. Thus, this sample is nearly black.**

**Table 5. Optical and thermal performance of the four coatings with SrCuSi<sub>4</sub>O<sub>10</sub> blue pigment shown in Figure 27. The reflectance at 550 nm is included as an indication of visual brightness.**

Co-pigment	Fluorescent pigment loading (g m <sup>-2</sup> )	Visual reflectance (550 nm)	Solar reflectance (SR)	Effective solar reflectance (ESR)	Fluorescence contribution (ESR-SR)
none	100	0.17	0.410	0.544	0.134
Shepherd 193 yellow	90	0.23	0.384	0.507	0.123
Azo yellow	130	0.26	0.350	0.475	0.125
Organic orange underlayer	130	0.08	0.330	0.469	0.139

Table 6 shows information on several additional samples that were characterized by ESR measurements. Of special note is the first sample with fluorescence contribution of 0.175, the largest value observed with the alkaline earth copper silicates. It utilized the washed Egyptian blue, with nearly optimum pigment amount, and was very well dispersed. It absorbed and emitted about 17% more photons than the sample with  $\omega = 65 \text{ g m}^{-2}$  in Figure 26, with the result that the quantum yield  $\phi$  was the same, at 0.72.

**Table 6. Five auxiliary samples for which optical and thermal performance data were obtained.**

Pigment(s)	Fluorescent pigment loading (g m <sup>-2</sup> )	Visual reflectance (550 nm)	Solar reflectance (SR)	Effective solar reflectance (ESR)	Fluorescence contribution (ESR-SR)
Washed Egyptian blue (EB)	68	0.15	0.394	0.569	0.175
Washed EB, with organic orange underlayer	60	0.06	0.263	0.388	0.126
Washed EB, mixed with azo yellow	128	0.16	0.196	0.304	0.108
As received EB (not purified)	128	0.14	0.268	0.360	0.092
Ba(La,Li)CuSi <sub>4</sub> O <sub>10</sub>	160	0.19	0.363	0.438	0.075

If the yellow or orange co-pigments mentioned above can also fluoresce, an additional cooling effect can be obtained. For example, phosphors are used in some white LEDs to absorb blue light and emit yellow. One such compound is YAG:Ce<sup>3+</sup> (Y<sub>3</sub>Al<sub>5</sub>O<sub>12</sub>:Ce<sup>3+</sup>) which absorbs between

420 and 500 nm and emits between 500 and 650 nm.<sup>29</sup> Another possibility is a dye with similar absorption and emission properties. A dye would also minimize scattering. The use of such supplementary phosphors can further excite the alkaline earth copper silicate phosphor and enhance the NIR emission.

## 10.2 Luminescent solar concentrators (LSC)

LSC devices utilize phosphors to absorb sunlight and emit fluorescence that can be trapped by total internal reflection and delivered to photovoltaic cells positioned at the edges of a large plastic or glass sheet. The total area of expensive photovoltaic cells can thereby be minimized. While these devices have great potential, obstacles have delayed implementation. Part of the diffuse fluorescence is nearly normal to the sheet and therefore not trapped. In some designs, a selective dielectric interference filter helps confine the fluorescence. Absorption of the fluorescence can occur before it reaches the sheet edge. The Stokes shift is a double-edged sword: energy is lost due to the redshift of wavelength, but a large Stokes shift also reduces re-absorption losses. Finally, the quantum yield of the phosphor is important. Current reviews<sup>13, 30, 31, 32</sup> indicate that an important class of prospective phosphors is organic dyes of which Ref. 13 gives 20 examples. Another class of phosphors is “quantum dots” such as nanoparticles of CdSe with shells of CdS that can absorb over an extended short-wave spectrum and emit fluorescence in a narrow long-wave band.<sup>33</sup> Other inorganic phosphors have not received close recent attention for LSC applications. Ruby,  $\text{Al}_2\text{O}_3:\text{Cr}^{3+}$ , is one possibility.<sup>11, 12, 34</sup> And now, with adequate quantum yield, the  $\text{MCuSi}_4\text{O}_{10}$  ( $\text{M} = \text{Ca}, \text{Sr}, \text{Ba}$ ) infrared phosphors should be investigated as well.

Li et al.<sup>27</sup> advocated the use of Egyptian blue phosphor for LSC applications. They noted that performance declines only slightly at elevated temperatures, and envisage that a polymer with nanoparticles or a specially formulated glass could host the blue particles in a transparent matrix with matching refractive index. However, a maximum quantum yield of 10.5 % is not acceptable for energy applications.<sup>3</sup> For various other applications such as temperature measurements using fluorescence, high efficiency is welcome, but not essential, provided the signal-to-noise ratio is acceptable. Our observation of quantum yields exceeding 70%, using these durable inorganic phosphors, may open a path for further LSC development.

## Discussion

In view of the much smaller quantum yield based on the sparse measurements reported in the literature<sup>3,15</sup> for the alkaline earth copper tetra-silicates, and in view of the relative novelty of our procedure for measurements of this yield, we briefly review the technique. Instead of employing a single wavelength for excitation, we use natural sunlight. The spectral absorption of the phosphor is deduced from spectral reflectance measurements, as is the overall solar reflectance (excluding fluorescence). The determination of the fluorescent intensity is based on *temperature measurements in sunlight*, in comparison with calibrated non-fluorescent gray

reference samples. The difference between the effective solar reflectance determined from temperature measurements in sunlight and the ordinary spectrometer-determined solar reflectance gives the fraction of the incident solar flux which is re-radiated by fluorescence. (That fraction varies from 0.075 to 0.175 in Table 2, for example.) Then, the number of fluoresced photons can be computed based on the known fluorescence spectrum. The quantum yield is thus an average over the components in sunlight that are absorbed by the phosphor.

The present technique for determining quantum yield using temperature measurements in sunlight has been employed once before.<sup>11</sup> The fluorescent pigment studied was ruby, the  $\alpha$ -phase of  $\text{Al}_2\text{O}_3:\text{Cr}$ . For doping levels up to 3 wt %  $\text{Cr}_2\text{O}_3$ , the quantum yield of a coating with ruby powder was found to be  $0.83 \pm 0.10$ . Some of the best work on this well-known material was done around the time of the demonstration of the first laser, see Maiman et al. (1961).<sup>35</sup> They studied a single crystal with light doping (0.05 wt %  $\text{Cr}_2\text{O}_3$ ) and found that the quantum efficiency varied with excitation wavelength in the range of 0.57 - 0.79. They concluded that the average value was  $0.70 \pm 0.05$ . Details preclude a precise comparison with Maiman et al. - single crystal vs. powder in a coating, anisotropy of ruby, dependence of emission spectrum with doping<sup>11</sup>, etc. - but their results provide evidence that measurements in sunlight can provide quantum yield values not greatly different from more traditional measurements.

A straightforward alternative approach to the determination of quantum yield could rely entirely on laboratory measurements using a lamp with monochromator for excitation. After such measurements, the question would remain: what is the performance in the sun? The present approach merely answers this last question first, and then works backward to deduce what the quantum yield must be.

## 11 Concluding remarks

Future applications of infrared fluorescence are enhanced by the high quantum yields of the alkaline earth copper tetra-silicates. It remains to be seen if the barium compound can match the very high performance of the calcium and strontium compounds.

Non-white coatings with high ESR (effective solar reflectance) are useful for energy conservation applications (e.g., to reduce air conditioning needs). Pigments used should have decay times  $>140 \mu\text{s}$  and contain as little  $\text{CuO}$  as possible. Coating systems should have a highly reflective backplane, optionally include near-infrared reflective pigments, and include a well-dispersed layer of  $\text{MCuSi}_4\text{O}_{10}$  ( $M = \text{Ca}, \text{Sr}, \text{or Ba}$ ) near-infrared phosphor.

In addition to medium and dark blue colors, green and even black materials can be achieved by adding co-pigments. A blue-shade black with ESR exceeding 0.5 appears likely in the near term.

## 12 Acknowledgements

At Berkeley Lab, T. Kirchstetter and X. L. Mao provided advice and equipment. At PPG, initiation of the work was catalyzed by S. Hellring, J. Kulfan, C. Balliet, and I. Schwendeman, and ongoing support was provided by B. Kornish, J. Stalker, and M. Baxter. At Shepherd Color, W. Yuhasz and S. Davis synthesized samples of barium- and strontium-bearing alkali-earth copper silicate blues and other IR-fluorescing pigments used for evaluation.

This work was supported by the Assistant Secretary for Energy Efficiency and Renewable Energy, Building Technologies Office of the U. S. Department of Energy under Contract nos. DE-AC02-05CH11231 and DE-EE0006347. Support was also provided by the California Energy Commission under Agreement EPC-14-010.

## References

- (1) Berke, H., The invention of blue and purple pigments in ancient times, *Chem. Soc. Rev.*, **2007**, 36, 15-30.
- (2) Giester, G. and Rieck, B., Wesselsite, SrCu[Si<sub>4</sub>O<sub>10</sub>], a further new gillespite-group mineral from the Kalahari Manganese Field, South Africa, *Mineral. Mag.*, **1996**, 60, 795-798.
- (3) Accorsi, G.; Verri, G.; Bolognesi, M.; Armaroli, N.; Clementi, C.; Miliani, C.; Romani, A., The exceptional near-infrared luminescence properties of cuprorivaite (Egyptian blue), *Chem. Commun.*, **2009**, 3392-3394
- (4) Borisov, S. M.; Wurth, C.; Resch-Genger, U.; Klimant, I., New life of ancient pigments: applications in high-performance optical sensing materials, *Anal. Chem.* **2013**, 85, 9371-9377.
- (5) Yen, W. M.; Weber, M. J., eds., *Inorganic phosphors: composition, preparation, and optical properties*, CRC Press **2004**, p. 334, prepared by L. S. Rohrer.
- (6) Tilley, R. J. D., *Colour and the optical properties of materials*, John Wiley & Son **2011**, p. 378.
- (7) McDonagh, C.; Burke, C. S.; MaxCraith, B. D.; Optical Chemical Sensors, *Chem Rev.* **2013**, 108, 400-422.
- (8) Werts, M. H. V.; Woudenberg, R. H.; Emmerink, P. G.; van Gassel, R.; Hofstraat, J. W.; Verhoeven, J. W.; A near-infrared luminescent label based on Yb<sup>III</sup> ions and its application in a fluoroimmunoassay, *Angew. Chem. Int. Ed.* **2000**, 39, No. 24, 4542-4544.
- (9) Kuck, S., Laser-related spectroscopy of ion-doped crystals for tunable solid-state lasers, *Appl. Phys. B*, **2001**, 72, 515-562.

- (10) Levinson, R.; Berdahl, P.; Akbari, H.; Miller, W.; Joedicke, I.; Reily, J.; Suzuki, Y.; Vondran, M., Methods of creating solar-reflective nonwhite surfaces and their application to residential roofing materials, *Sol. En. Mat. & Sol. Cells*, **2007**, 91, 304-314.
- (11) Berdahl, P.; Chen, S. S.; Destailats, H.; Kirchstetter, T. W.; Levinson, R. M.; Zalich, M. A.; Fluorescent cooling of objects exposed to sunlight – the ruby example, *Sol. En. Mat. & Sol. Cells*, **2016**, 157, 312-317.
- (12) Friedman, P. S.; Parent, C. R., Luminescent solar concentrator development, Project Report SERI/STR-211-3149 for the Solar Energy Research Institute, **1987**.
- (13) Devije, M. G.; Verbunt, P. P. C., Thirty years of luminescent solar concentrator research: solar energy for the built environment, *Adv. Energy Mater.*, **2012**, 2, 12-35.
- (14) de Mello, J. C.; Wittmann, H. F.; Friend, R. H., An improved experimental determination of external photoluminescence quantum efficiency, *Adv. Mater.*, **1997**, 9 No.3, 230-232.
- (15) Chen, Y.; Shang, M.; Wu, X.; Feng, S., Hydrothermal synthesis, hierarchical structures and properties of blue pigments  $\text{SrCuSi}_4\text{O}_{10}$  and  $\text{BaCuSi}_4\text{O}_{10}$ , *CrystEngComm*, **2014**, 16, 5418-5423.
- (16) Jose, S.; Reddy, L., Lanthanum-strontium copper silicates as intense blue inorganic pigments with high near-infrared reflectance, *Dyes and Pigments* **2013**, 98, 540-546.
- (17) Levinson, R.; Akbari, H.; Berdahl, P., Measuring solar reflectance – part I: defining a metric that accurately predicts solar heat gain, *Solar Energy*, **2010**, 84, 1717-1744.
- (18) Mazzi, F.; Pabst, Reexamination of cuprorivaite, *Amer. Mineral.* **1962**, 47, 409-411.
- (19) Giester, G.; Rieck, B., Effenbergerite,  $\text{BaCu}[\text{Si}_4\text{O}_{10}]$ , a new mineral from the Kalahari Manganese Field, South Africa: description and crystal structure, *Mineralogical Magazine*, **1994**, 58, 663-670.
- (20) Levinson, R.; Berdahl, P.; Akbari, H., Solar spectral optical properties of pigments – Part I: model for deriving scattering and absorption coefficients from transmittance and reflectance measurements, *Solar Energy Materials & Solar Cells*, **2005**, 89, 319-349.
- (21) Levinson, R.; Berdahl, P.; Akbari, H., Solar spectral optical properties of pigments – Part II: survey of common colorants, *Solar Energy Materials & Solar Cells*, **2005**, 89, 351-389.
- (22) Levinson, R.; Chen, S.; Ferrari, C.; Berdahl, P.; Slack, J., Methods and instrumentation to measure the effective solar reflectance of fluorescent cool surfaces, *Energy & Buildings*, **2017**, 752-765. <https://doi.org/10.1016/j.enbuild.2016.11.007>
- (23) M. Zalich, B. Kornish, Fluorescent pigments for high-performance cool roofing and facades, **2016**, Project report, contract no. DE-EE0006347, <http://osti.gov>.

- (24) E.D. Palik, ed., *Handbook of Optical Constants of Solids*, 1998, Academic Press.
- (25) Cheng, Q.; Chai, J.; Zhang, Z., Investigation of double-layer coating with CuO particles of different concentrations on aesthetic and thermal aspects, *Int. J. Thermal Sciences*, 2016, 105, 36-44.
- (26) Chen, Y.; Zhang, Y.; Feng, S., Hydrothermal synthesis and properties of pigments Chinese purple  $\text{BaCuSi}_2\text{O}_6$  and dark blue  $\text{BaCu}_2\text{Si}_2\text{O}_7$ , *Dyes and Pigments*, 2014, 105, 167-173.
- (27) Li, Y. J.; Ye, S.; Wang, C. H.; Wang X. M.; Zhang, Q. Y., Temperature-dependent near-infrared emission of highly concentrated  $\text{Cu}^{2+}$  in  $\text{CaCuSi}_4\text{O}_{10}$  phosphor, *J. Mater. Chem. C*, 2014, 2, 10395-10402.
- (28) Zhuang, Y.; Tanabe, S., Forward and back energy transfer between  $\text{Cu}^{2+}$  and  $\text{Yb}^{3+}$  in  $\text{Ca}_{1-x}\text{CuSi}_4\text{O}_{10}:\text{Yb}_x$  crystals, *J. Appl. Phys.*, 2012, 112, 093521.
- (29) Kim, Y.; Shim, K. B.; Wu, M.; Jung, H. K., Monodispersed spherical YAG: $\text{Ce}^{3+}$  phosphor particles by one-pot synthesis, *J. of Alloys and Compounds*, 2017, 693, 40-47.
- (30) van Sark, W. G. H. M., Luminescent solar concentrators - A low cost alternative, *Renewable Energy*, 2013, 49, 207-210.
- (31) Assadi, M. K.; Hanaei, H.; Mohamed, N. M.; Saidur, S. B.; Bashiri, R.; Moayedfar, M., Enhancing the efficiency of luminescent solar concentrators (LSCs), *Appl. Phys. A*, 2016, 122, 821, 1-12.
- (32) Tummeltshammer, C.; Taylor, A.; Kenyon, A. J.; Papakonstantinou, I., Losses in luminescent solar concentrators unveiled, *Solar Energy Materials & Solar Cells*, 2016, 144, 40-47.
- (33) Bronstein, N. D.; Yao, Y.; Xu, L.; O'Brien, E.; Powers, A. S.; Ferry, V. E.; Alivisatos, A. P.; Nuzzo, R. G., Quantum dot luminescent concentrator cavity exhibiting 30-fold concentration, *ACS Photonics*, 2015, 2, 1576-1583.
- (34) Hovel, H. J.; Hodgson, R. T.; Woodall, J. M., The effect of fluorescent wavelength shifting on solar cell spectral response, *Solar Energy Materials*, 1979, 2, 19-29.
- (35) Maiman, T. H.; Hoskins, R. H.; D'Haenens, I. J.; Asawa, C. K.; Evtuhov, V., Stimulated optical emission in fluorescent solids. II. Spectroscopy and stimulated emission in ruby, *Phys. Rev.*, 1961, 123, 1151-1157.